PTOLEMY Project:
Graphene-Based Particle Detector

Author: Martijn Velders (s1002664)
Supervisors: Prof. dr. N. de Groot & Prof. dr. U. Zeitler
Second corrector: Prof. dr. C.W.J.P. Timmermans
Department: High Energy Physics (HEP)
Institute for Mathematics, Astrophysics and Particle Physics (IMAPP)

March 12, 2023

A thesis submitted in fulfillment of the requirements
for the degree of MSc in Physics and Astronomy

Radboud Universiteit Nijmegen

Abstract

The Big Bang is widely accepted to be the starting point of the existence of the universe and everything in it from galaxies to the lightest particles. A widely accepted methods to study this starting point is via the cosmic microwave background although this is only limited to $3.8 \cdot 10^5\,yrs$ after the Big Bang. New information from $1\,s$ after the Big Bang could be obtained by detecting the cosmic neutrino background. One of the goals of the PTOLEMY project is to detect those neutrinos. With a combination of the relatively new material, graphene, and the rare isotope, tritium, this detection might be possible. In this thesis steps toward a tritium-loaded graphene target prototype are explored. These steps consist of smaller experiments e.g. range determination of β particles through SiO_2 wafers, measuring transfer curves of (hydrogenated/annealed) graphene, and β particle detection with scintillators which ultimately leads to a setup to detect particles passing (hydrogenated) graphene sample. This detection will be a significant achievement in the research of detecting neutrinos from the cosmic neutrino background.

Acknowledgements

Contents

List of Figures

List of Tables

1 Introduction

The observable universe was created with the Big Bang 13.8 billion years ago. This intriguing event can be studied via different methods such as observing the expansion of the universe by red-shifted standard candles (Hubble expansion), the measured abundance of light elements (Big Bang Nucleosynthesis), and detecting Cosmic Microwave Background radiation (CMB). CMB radiation is electromagnetic radiation emitted at a temperature of $3000\,K$, with a frequency of $160\,GHz$, $3.8\cdot10^5\,yrs$ after the Big Bang. Before that time the optical density of the universe was too large for electromagnetic radiation to pass through. Currently, the CMB radiation is measured at a temperature of $2.7\,K$ with small temperature fluctuations. A map of these temperature fluctuations is often seen as the earliest picture of the universe [1, 2].

No electromagnetic radiation from before the CMB radiation can be observed, but merely one second after the Big Bang at a temperature of $3.0\cdot10^{10}\,K$ (30 billion K) another particle was able to travel through space; the neutrino. A neutrino is a lightweight and almost interaction-free particle. The neutrinos emitted during the Big Bang are still present today and are called Cosmic Neutrino Background ($C\nu B$). Despite a flux of $10^{13}\,cm^{-2}s^{-1}$, no $C\nu B$ has been observed due to two main reasons. First, neutrinos only interact via the weak interaction, which makes them hard to see. Second, neutrinos have cooled down to $1.9\,K$ [1] since the Big Bang due to the expansion of the universe. The neutrino kinetic energy is so low, $\sim 10^{-5}eV$, that current detectors are unable to detect them [3]. Although, being able to detect the $C\nu B$ could provide magnificent information about the universe and the Big Bang [2]. With the PTOLEMY [3] project a technique to detect the $C\nu B$ and to study and generate the necessary technology is developed. By measuring electrons from tritium decay (due to the $C\nu B$ capture) with high precision, a small fluctuation in electron energy from the $C\nu B$ could be determined. A step in the right direction for these precise measurements could be taken by using a tritium-loaded graphene target. The possibilities of using tritium for measuring the $C\nu B$ were already suggested by Steven Weinberg in 1962 [4]. The PTOLEMY project is aimed to develop a scalable design for a cosmic neutrino telescope. This would be the first neutrino telescope that can directly observe neutrino density fluctuations from one second after the Big Bang [2].

The heavy isotope of hydrogen (i.e. tritium, T), is a beta emitter with a decay energy of $18.6\,keV$, a lifetime of $12.3\,yrs$, and a relatively high neutrino capture cross-section of $\sim 10^{-45}\,cm^{-2}$ [4] [5]. Tritium decays into helium-3, an electron, and an electron anti-neutrino as follows $^3\text{T} \rightarrow\ ^3\text{He} + \text{e}^- + \bar{\nu}_e$. Here a neutron is converted into a proton, electron, and anti-electron neutrino. Due to the three-body decay, the energy of the electron is described by an energy spectrum. A similar process can be induced by an incoming electron neutrino (originating from the $C\nu B$) $^3\text{T} + \bar{\nu}_e \rightarrow\ ^3\text{He} + \text{e}^-$. In the latter case, the electrons are emitted monochromatically. A clear distinction between the monochromatic energy of the electron and the energy spectrum of the electrons is expected. The monochromatic energy of the electrons gives a clear peak beyond the tritium endpoint of the energy spectrum as shown in figure 1.1. Only relative differences between the neutrino masses are known due to the lack of knowledge about the absolute neutrino masses. This gives freedom in the mass ordering of the neutrino flavours. Normal mass ordering (NO) happens when the lightest neutrino has the largest mixing with the electron flavour. Inverted mass ordering (IO) happens when the heaviest neutrino has the largest mixing with the electron flavour [6, 7].

For the determination of the neutrino mass, molecular tritium ($^3\text{T}-^3\text{T}$) is often used. This limits the precision on neutrino mass to $\sim 100\,meV$. The main reason for this limitation is the instability of the final molecular state which is $^3\text{T}-^3\text{He}$. Vibration modes cause the energy of electrons to diverge. With atomic tritium, this limitation, due to vibration modes, is not present and a higher precision can be accomplished [6]. For tritium-based experiments, it was discovered that tritium is bound to a (2D) graphene lattice with binding energy beneath the eV-scale. This combination gives a stable configuration at room temperature. Knowledge about the background of electrons (not originating from tritium or the $C\nu B$) is crucial for a successful PTOLEMY experiment. Impurities in the target might cause disturbances in the measurements. One can think about ^{14}C decay in graphene. Knowledge about graphene, its electronic and potential particle detection properties, and resistance change due to tritium absorption should therefore be examined [1, 6].

---

[1]Lower temperature than the CMB and is equivalent to $1.6\cdot10^{-4}\,eV$.

[2]Information about the Big Bang can be deduced from the neutrino information one second after the Big Bang.

[3]Claudius Ptolemaeus was a Greek natural philosopher and PTOLEMY is an acronym for PonTecorvo Observatory for Light, Early-universe, Massive-neutrino Yield.

[4]See Appendix A for the cross-section calculation for neutrino capture of tritium.
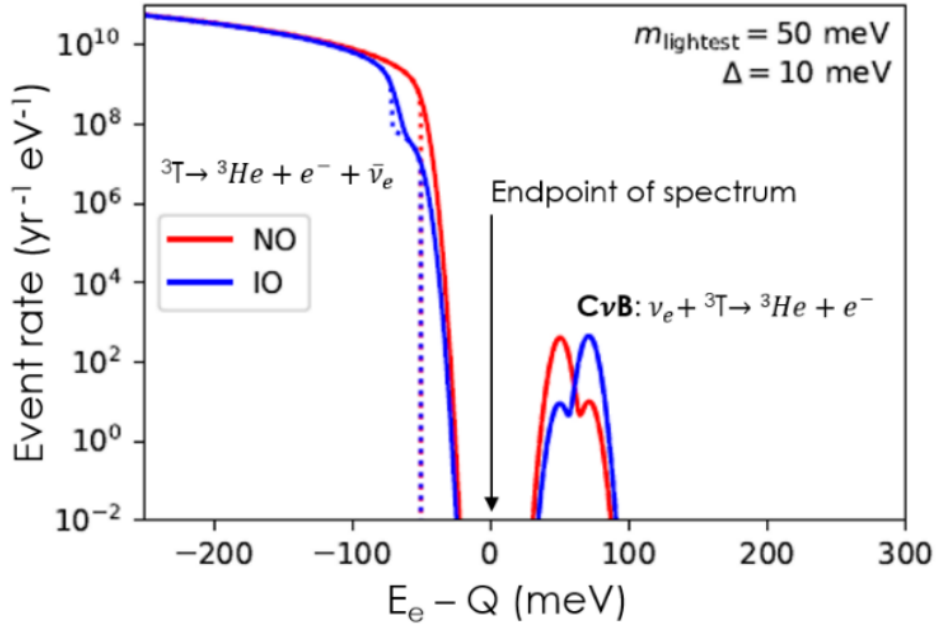
Figure 1.1: The last few $100\,meV$ of the energy spectrum of electrons from the tritium decay endpoint. Above the endpoint energy, the monochromatic energy from the neutrino capture is shown. In red the normal mass ordering and in blue the inverted mass ordering for the neutrinos is simulated. Here it is assumed that the neutrino masses are of the order of $50\,meV$ and the energy resolution of the electrons is around $10\,meV$. Both require extreme precision measurements [6].

The entire PTOLEMY project consists unexplored physics and novel technology, which should be understood to eventually detect $C\nu B$. In this thesis, the possibilities of creating a tritium-loaded graphene target are explored. This is divided into two parts which are combined at the end. The first part consists of understanding and measuring a stable transfer curve of graphene. The second part consists of understanding and measuring electrons from a β source. After this introduction, relevant theories for this thesis will be given. In section 2 some basic and more specific, relevant theories about graphene for this thesis will be discussed. In section 3 information about (mainly β) decays is given. Interaction with decay products with matter is included as well as in section 3.3. Thereafter, in section 4, used materials and apparatuses are discussed. In section 5 the setups for all executed experiments are given. The results of these experiments are given in section 6. The conclusion and discussion can be found in section 7. An outlook is given in section 8. Some additional information is given in the Appendix.

2   Graphene

Graphene is a two-dimensional (2D) material made up of tightly bound carbon atoms arranged in a honeycomb lattice. Ever since the year, 1950 [8, 9] graphene was already studied theoretically. Four decades later graphene appeared as an excellent theoretical toy model for quantum-electrodynamics [10, 11]. This theory became reality in 2004 when Geim and Novoselov created graphene by the use of scotch tape [12–15].

When a 2D material is discussed no more than 10 layers of graphene were allowed. This limit was introduced due to a rapid change in electronic structure when about 10 layers of graphene were exceeded [16]. Single and double-layer graphene has simple electronic spectra because it is a zero-bandgap semiconductor with one type of electron and one type of hole. Once three or more layers were included the spectra become more complicated. Conduction and valence bands started overlapping and charge carriers appeared [16, 17]. Landau and Peierls stated earlier that 2D crystals were thermodynamically unstable and therefore should not exist. They claimed that for every non-zero temperature the thermal fluctuations caused vibrations of atoms which would be around the interatomic distances to break the structure [18]. Experiments confirmed this theory and with a thickness of about ten layers the structure became unstable and would decompose, but Geim and Novoselov changed this theoretical view in 2004 by producing graphene on a substrate [19, 20].

A large advantage of 2D (rippled) graphene is its high crystal quality. Due to the high quality, charge carriers can travel for thousands of interatomic distances without scattering [12–14, 21, 22]. It is possible to make the case that this 2D material still agrees with the theory of Landau and Peierls. The 2D material can be seen as a thinly sliced piece of 3D material. This 3D kind of sample that is left, gains elastic energy but it suppresses thermal vibrations. The total free energy is minimized at a sufficient temperature [23].

2.1   Creation graphene

The first time graphene was created by Geim and Novoselov this was done by using a piece of graphite and scotch tape. By sticking the scotch tape on the piece of graphite, several layers of carbon/graphene stuck on the tape. This tape with several layers of carbon/graphene on it was then stuck on another material and this was repeated several times. After this procedure, the tape is stuck to a SiO_2 film. This is where a single-layer of graphene was placed [11–13, 15]. Despite the simplicity of this technique, finding graphene is difficult. Mainly due to relatively small regions with a single layer of graphene compared to the large regions with still multiple layers of graphene and graphene being almost completely transparent to visible light. Nevertheless, this technique could create high-quality graphene crystals up to $100\,\mu m$ [13, 24]. The size was sufficient for most research purposes. Despite this straightforward method, other groups did not find single-layered graphene with this method. Detection problems were solved by placing the graphene on a Si wafer with a thin film of SiO_2 on top of the wafer as shown in figure 2.1. This adjustment made the graphene visible with an optical microscope [25].

Another method to obtain high-quality graphene is via chemical vapor deposition (CVD). With this method, gaseous reactants are deposited on a Cu-substrate. A reaction chamber at a specific temperature with molecules (often methane) inside made contact with the substrate to produce a thin film. The remaining molecules in the chamber are pumped away afterward. With the correct temperature, the deposition goes in a controlled manner. This is a quite slow process which takes hours for a small area. In combination with extremely low-pressure inside the reaction chamber, it is possible to strongly reduce unwanted reactions. One of the biggest disadvantages of CVD is the toxic gasses that might arise during the reaction [26]. For graphene, the CVD process consists of two steps. First, utilising pyrolysis [5] carbon is formed. Due to the extreme temperatures, it is helpful to use a catalyst to reduce the reaction temperature. This process happened at temperatures of $2500\,°C$ but with a catalyst $1000\,°C$ is sufficient. Catalysts, on one hand, could reduce the temperature but on the other hand, they could contaminate the reaction chamber. Second, when the carbon is formed, graphene structures must be transferred from the Cu-substrate to the SiO_2 substrate and in no other place. All this makes the fabrication of graphene precision work. Eventually, the same situation as with the exfoliation is created as shown in figure 2.1.

---

[5]Pyrolysis is a process wherein a high temperature and inert environment materials are separated.
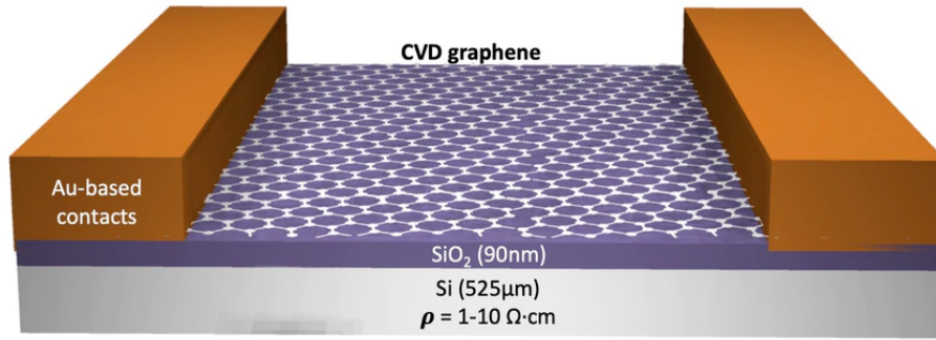
Figure 2.1: Graphene (white honeycomb lattice) deposited via CVD on a Cu-substrate and transferred to a thin film of SiO_2 (purple) with a thickness of $90\,nm$ which was placed on a wafer of Si (grey) with a thickness of $525\,\mu m$. On the sides of the graphene and SiO_2 film, two gold contacts were placed. These contacts were useful in measuring certain (electronic) properties of graphene e.g. current and voltage [27].

2.2 Graphene structure

Graphene consists of carbon. Natural carbon ($^{12}_{6}$C) has six electrons filling the $1s^2$ shell, the remaining four electrons fill the $2s^2 2p^2$ states [6]. This gives the ground state configuration (ground-state multiplet) of atomic carbon (with spin $S = 1$, total orbital momentum $L = 1$, and total angular momentum $J = 0$). The first excited state ($1s^2 2s^1 2p^3$) with $J = 1$ has an energy of about $2\,meV$. This indicates the strength of the spin-orbit coupling in carbon. The lowest energy state with a $1s^2 2s^1 2p^3$ configuration has an energy of about $4.2 eV$. This energy is required to excite an electron from the $2s$ state to the $2p$ state. The exact distribution of electrons over the orbitals is now $1s^2 2s^1 2px^1 2py^1 2pz^1$, which is sp^3 hybridized [28].

Electron wave functions overlap at different sites. This forms molecules out of atoms according to molecular orbits and decreases the total energy. The energy decrease is enough to excite an electron from the $2s$ to the $2p$ state. For the maximum energy gained during the formation of a covalent bond, the overlap in wave function with their neighboring atoms should also be maximal. The bonds are stronger when the overlap in wave functions is larger. With four basis functions corresponding to the spherical harmonics (preferably in orthonormalized linear combinations) the maximum overlap can be calculated. With the normalization and orthogonality conditions, a tetrahedral construction is formed as shown in figure 2.2a where the directions of the sp^3 bonds in the carbon atom are visualized.

It is also possible to form a hybrid covalent bond with three sp electrons distributed through the molecule, where one p electron (say pz) has a different purpose. With the same procedure as mentioned before, it is possible to find the maximum overlap of the wave functions in the xy-plane. Here maxima are separated by a $120\,°$ angle. These bonds are called σ-bonds. The p electron in the p orbital that is perpendicular to the plane, the pz electron, forms a π-bond. This state is called an sp^2 state and forms the layered structure of graphite which is visualized in figure 2.2b [7].

---

[6]The $2s$ orbital is filled and the $2p$ orbital is filled as $2px^1 2py^1$.

[7]Figures 2.2a and 2.2b consist of a combination of orbitals as shown in this subfigure [29].
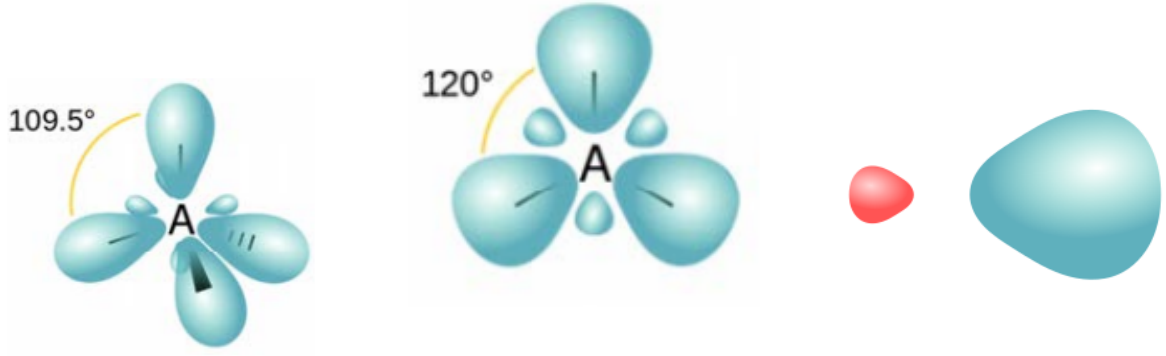
(a) The configuration of an sp^3 orbital. This is the structure present in diamond, with the A in the middle representing the central atom. The typical angle of 109.5 ° between atomic orbitals is indicated as well. A tetrahedral structure can be imagined by connecting the endpoints of the orbitals [30].

(b) The configuration of an sp^2 orbital. This is the structure present in graphene, with the A in the middle representing the central atom. The typical angle of 120 ° between atomic orbitals is indicated as well. A trigonal planar structure can be imagined by connecting the endpoints of the orbitals [30].

(c) Subfigures 2.2a and 2.2b consist of a combination of this orbital [29].

Figure 2.2: A visualization of the sp^3 and sp^2 orbitals. Both consist of combined sp^x like orbitals.

Graphene has a crystal lattice in a honeycomb (hexagonal) shape. This shape is caused by the sp^2 hybridization where an electron from the 2s-orbital is excited to the 2p-orbital. To describe this lattice in more detail the Bravais lattice is introduced. Graphene has a triangular structure with lattice vectors $\vec{a}_1 = \frac{a}{2}(3, \sqrt{3})$ and $\vec{a}_2 = \frac{a}{2}(3, -\sqrt{3})$ as shown in figure 2.3 with $a \approx 1.42$ Å the nearest neighbor distance. A unit cell is another tool to define the space of a lattice. Each unit cell in graphene contains two carbon atoms. The Fourier transform of the lattice, reciprocal lattice, is also triangular with lattice vectors $\vec{b}_1$ and $\vec{b}_2$. For measurements on the lattice, it might be convenient to use the reciprocal lattice rather than the direct lattice. In figure 2.3 it is also shown that points K, K' and M are special high-symmetrical points. Γ indicates the center of the Brillouin zone. The electronic band structure of graphene with symmetrical points is shown in figure 2.4 [31].
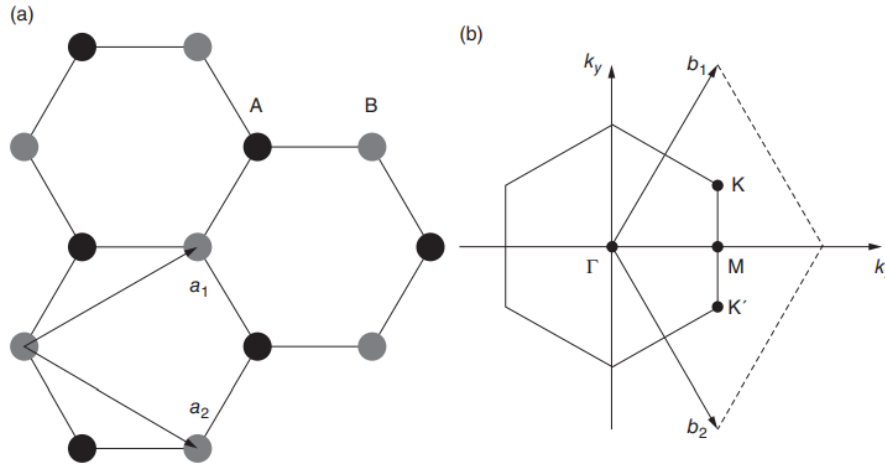
Figure 2.3: In (a) a honeycomb lattice is shown. The black dots represent sublattice A and the grey dots represent sublattice B. Also the lattice vectors $\vec{a}_1$ and $\vec{a}_2$ are drawn for sublattice B. In (b) the reciprocal lattice vectors $\vec{b}_1$ and $\vec{b}_2$ are drawn. Special symmetry points K, K' and M are indicated as well. Γ is the center of the Brillouin zone [28].
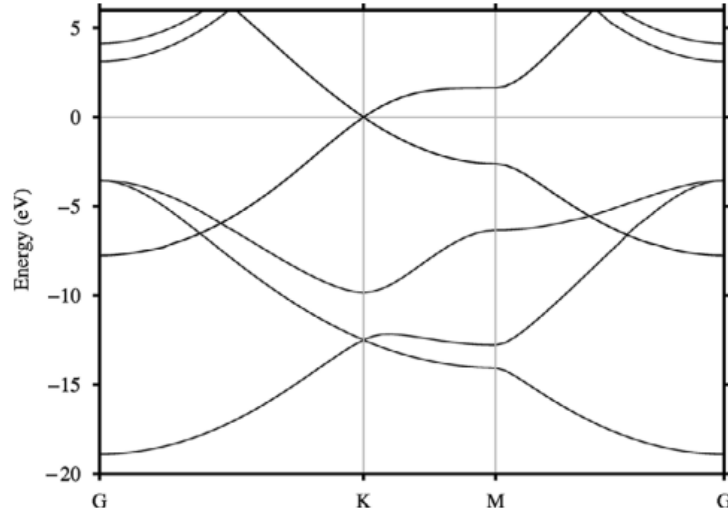
Figure 2.4: The electronic band structure of graphene. On the K symmetry point, a conical structure is visible [28].

The hybridized sp^2 states (σ-states) form occupied and empty bands or band gaps. The pz states (π-state) form a single band that has a conical self-crossing point in K and K'. Most of the unique electronic properties of graphene can be explained by the conical points of the electronic band structure [28].

With the tight-binding model, more insight into the energy spectrum of graphene can be given. We start by looking at the nearest-neighbor approximation, for the π-states. We introduce the hopping parameter t. The hopping parameter is a parameter that indicates the amount of energy necessary for an electron to jump to the next particle. In the nearest-neighbor approximation we assume that hopping between different sublattices does happen but not within a sublattice. The hopping parameter is $t = 0.4\,eV$. The tight-binding Hamiltonian is defined as a 2×2 matrix

$$\hat{\boldsymbol{H}} = \begin{pmatrix} 0 & tS(\vec{k}) \\ tS^*(\vec{k}) & 0 \end{pmatrix}, \tag{2.1}$$

with $\vec{k}$ the wave vector and $S(\vec{k})$ is given by Eq. 2.2

$$S(\vec{k}) = \sum_{\vec{\delta}} e^{i\vec{k}\vec{\delta}}, \tag{2.2}$$

here $\vec{\delta}$ are the nearest-neighbor vectors. By solving the eigenvalue equation an expression for the energy can be obtained: $E(\vec{k}) = \pm t|S(\vec{k})|$. As we would expect at the band crossing points we have $S(\vec{K}) = S(\vec{K'}) = 0$. When the Hamiltonian is expanded around these points we arrive at the expression given by Eq. 2.3

$$\hat{H}_{K,K'}(\vec{q}) \approx \hbar\nu \begin{pmatrix} 0 & q_x \mp iq_y \\ q_x \pm iq_y & 0 \end{pmatrix}. \tag{2.3}$$

Multiple steps were taken to arrive at this result which are not included in this thesis. The phase factor is excluded by a unitary transformation, $\vec{q} = \vec{k} - \vec{K}$ and $\vec{q'} = \vec{k} - \vec{K'}$. Also $\nu = \frac{3a|t|}{2\hbar}$ is defined as the electron velocity at conical points. It is possible to include the next nearest neighbor. This would break the electron-hole symmetry but leaves the behaviour of the Hamiltonian near the conical points unchanged. A visualization of the nearest-neighbor approximation is shown in figure 2.5.

When we look at undoped graphene the energy of the conical points and the Fermi energy coincide. A filled valence band and an empty conduction band with a zero band gap result in a gapless semiconductor. Other materials with this property are already known, but the uniqueness of graphene mainly comes from special electron states and the symmetry between electrons and holes. Typically, graphene is doped so the Fermi energy and the conical point lie close together. For an effective model, it is necessary to expand the Hamiltonian around K and K' as shown before. Additionally, a quantum replacement must be made

10
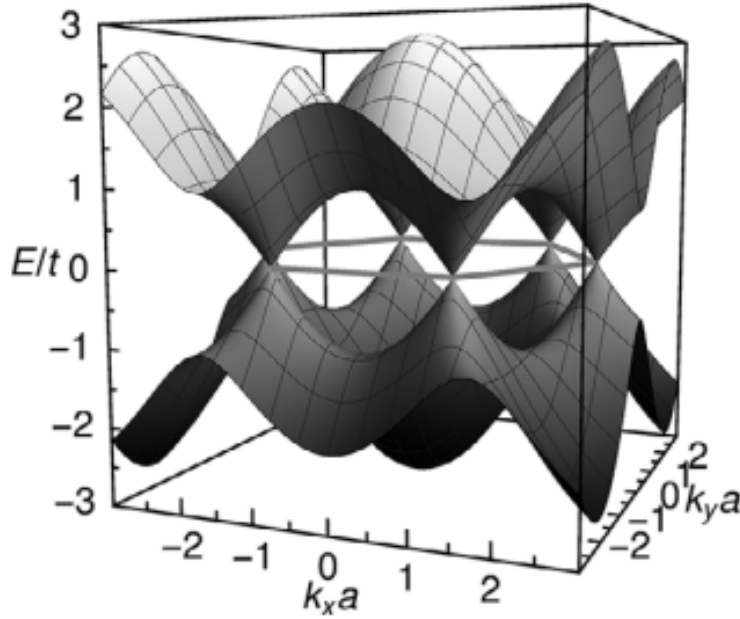
Figure 2.5: The energy spectrum of graphene in the next nearest neighbor approximation. The six conical point/energy bands are the Dirac points [24].

for $q_x \rightarrow -i\frac{\partial}{\partial x}$ and $q_y \rightarrow -i\frac{\partial}{\partial y}$. This replacement corresponds to the effective mass approximation. From Eq. 2.3 we can find

$$\hat{H}_K = -i\hbar\nu\vec{\sigma}\nabla, \tag{2.4}$$

and

$$\hat{H}_{K'} = \hat{H}_K^T, \tag{2.5}$$

with $\vec{\sigma}$ the Pauli matrices in 2D and T indicating the transpose matrix. For the low-energy Hamiltonian, a 4×4 matrix is needed. Here two sublattices and two conical points (K and K') are included. A basis consisting of a wave function with one of the two sublattices and one of the two conical points is chosen. This choice results in the most symmetric form possible of the Hamiltonian as shown in Eq. 2.6

$$\hat{H} = -i\hbar\nu\tau_0 \otimes \vec{\sigma}\nabla, \tag{2.6}$$

τ_0 is the unit matrix for the conical point indices or valley indices. Ideal graphene has decoupled valleys and this does not change with inhomogeneities [28]. Eq. 2.4 is a Dirac-like Hamiltonian for massless fermions in 2D. One exception is the different speed of light which is $\nu = \frac{c}{300} \approx 10^6 \, m/s$. This is also called the Fermi velocity which is the speed of the fastest fermions with a kinetic energy equal to the Fermi energy. In graphene, charge carriers behave like relativistic particles which makes graphene an excellent playground for studying quantum relativistic effects. As expected the Schrödinger equation which usually describes solids e.g. graphene in condensed-matter physics, does not work due to the relativistic particles. The Dirac equation would describe this better. Not the electrons/holes move relativistic but the interaction of these electrons with the lattice gives rise to new quasiparticles which are massless Dirac fermions. To get a better idea about the massless Dirac fermions one can think of electrons without rest mass or neutrinos with an electric charge. At low energy, these particles are correctly described by the Dirac equation with an effective speed of light $v_F = 10^6 ms^{-1}$. Graphene is made up of two sublattices A and B. The energy bands of the sublattices intersect at zero energy near the edges of the Brillouin zone. The components of the Dirac spinor indicate the electron distribution in sublattice A and B. This quantum number is called the pseudospin. The pseudospin here is somewhat analogue to spin in QED. When the pseudospin is 'up' we talk about sublattice A and when the pseudospin is 'down' sublattice B is meant. With other internal degrees [8], the electrons in graphene can thus be described by an 8×8 matrix, but it can be reduced for true Dirac fermions. Electrons (and holes)

---

[8]Isospin and real spin.

are linear combinations of states of sublattices A and B. By a unitary transformation Eq. 2.4 can be diagonalized to obtain eigenfunctions that correspond to the electron and hole states. The eigenvalues that can then be read off are

$$E_{e,h} = \pm\hbar\nu k. \tag{2.7}$$

From the wave functions, it can be seen that the electrons in graphene have a pseudospin direction. This direction is parallel to their motion and is a chiral state as expected for massless Dirac fermions. The same is true for holes except they are antiparallel and have a helical state [28]. Higher-order expansion terms of the tight binding model are not included in this thesis.

2.3   Electronic properties of graphene

Graphene has exceptional electronic quality, so a lot of research is done on this property. The high quality of the crystals in graphene is ideal for the ambipolar electric field effect as shown in figure 2.6. The ambipolar electric field effect induces negative or positive charge carriers in the graphene layer depending on the electric field applied between the graphene and the Si backgate. Figure 2.6 shows the transfer curve of graphene generated by the gate voltage V_G.
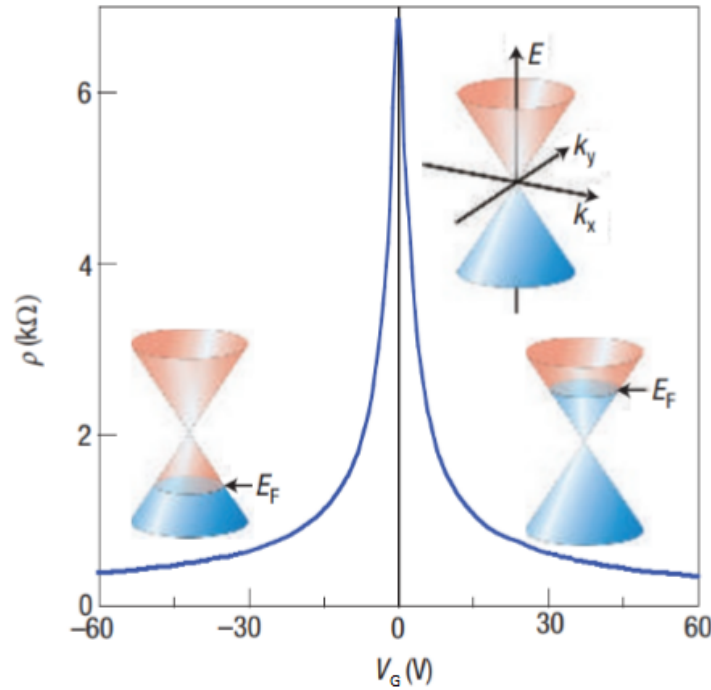
Figure 2.6: The resistivity of graphene, ρ, in $k\Omega$ set out against the gate voltage V_G in Volts (V). The Dirac peak is visible at $V_G = 0\,V$, at this point, the valence band (cone) is filled and the conduction band (cone) is empty (holes). On the left of the Dirac peak, the valence band is not completely filled. On the right of the Dirac peak, the valence band is filled and the conduction band is partially filled [24].

Charge carriers can switch between electrons and holes continuously with high concentrations ($n = 10^{13}\,cm^{-2}$). The mobility, μ, can be above the $15000\,cm^2V^{-1}s^{-1}$ [9]. The temperature has a minimum influence on the mobility. Impurity scattering is the main reason the mobility is not a factor 10 higher [12–14]. Besides, the quantum Hall effect also shows the extreme electronic quality of graphene. This effect is even measurable at room temperature in graphene, which extends the temperature range by a factor of 10 compared to previous quantum Hall effects [32].

The quantum Hall effect was one of the first electronic properties of graphene which were experimentally studied. The quantum Hall behaviour in 'relativistic' graphene could be visualized by a ladder of equidistant steps in Hall conductivity, σ_{xy}, which continues through the neutrality Dirac point. At that point, charge carriers changed from electrons to holes [13, 14]. The quantum Hall effect in graphene was shifted by a factor of $\frac{1}{2}$. Also, double spin degeneracy and double valley degeneracy [33] result in an

---

[9]For reference, copper has electric mobility of $\mu = \sim 6000\,cm^2V^{-1}s^{-1}$.

additional factor of 4 in the ordinary expression for the conductivity of a quantum Hall effect leading to a quantized Hall conductivity.

$$\sigma_{xy} = \pm\frac{4e^2}{h}(N + \frac{1}{2}). \tag{2.8}$$

Here N indicates the index of the Landau levels, e is the elementary charge and h is the Planck constant. With a QED-like quantization of the electronic spectrum of graphene in a magnetic field B is described by Eq. 2.9

$$E_N = \pm\nu\sqrt{2e\hbar BN}, \tag{2.9}$$

where the $\pm$ deals with electrons and holes and ν is the Fermi velocity [34–36]. Eq. 2.9 shows a linear dispersion of the form $E = \nu\vec{k}$ which is in contrast with the classic dispersion relation of $E = \frac{\hbar k^2}{2m}$.

Graphene also appears to be one of the few metallic system without a magnetoresistance [10], even at the Dirac point, e.g. where the resistance is the highest, with a temperature of about 4K no significant magnetoresistance was measured [37]. For high concentrations of electrons or holes and without inter-valley scattering no magnetoresistance should exist. This is because the triangular wrapping of the Fermi surface of graphene breaks the time-reversal symmetry in each valley [38].

---

[10]Materials change their electrical resistance when an external magnetic field is applied.

2.4 Annealing

Exposure of graphene to the air or other particles increases the number of impurities in the graphene. Despite impurities, it is always possible to return to a conductivity close to $\frac{4e^2}{h}$ through annealing. Graphene is strongly hole-doped due to impurities on the surface, which is mainly in the form of water. This shifts the charge neutrality point to the positive side of the gate voltage (V_G) compared to the ideal case shown in figure. 2.6. The device mobility μ indicates the quality of a sheet of graphene. Eq. 2.10 [11] shows an equation for the mobility

$$\mu = \frac{1}{ne\rho},\tag{2.10}$$

where ρ is the resistivity obtained from $\rho = Rl/w$ with R the measured resistance, l the length of the graphene and w the width of the graphene, n the number of charge carriers per cm^2, and e the elementary charge of an electron. The quality can be improved by annealing the graphene for several hours in vacuum conditions at high temperatures of about $120\,°C$. The impurities start to evaporate from the surface of the graphene. Annealing can be done at higher temperatures but is often started at around $120\,°C$ and is increased in steps of several tens of degrees. The higher the temperature, the higher the obtained quality of the graphene, although at too high temperatures the wiring and contacts might be damaged. A sign of improved quality and better homogeneity is the reduced width of the Dirac peak as shown in figure 2.7 [39, 40].
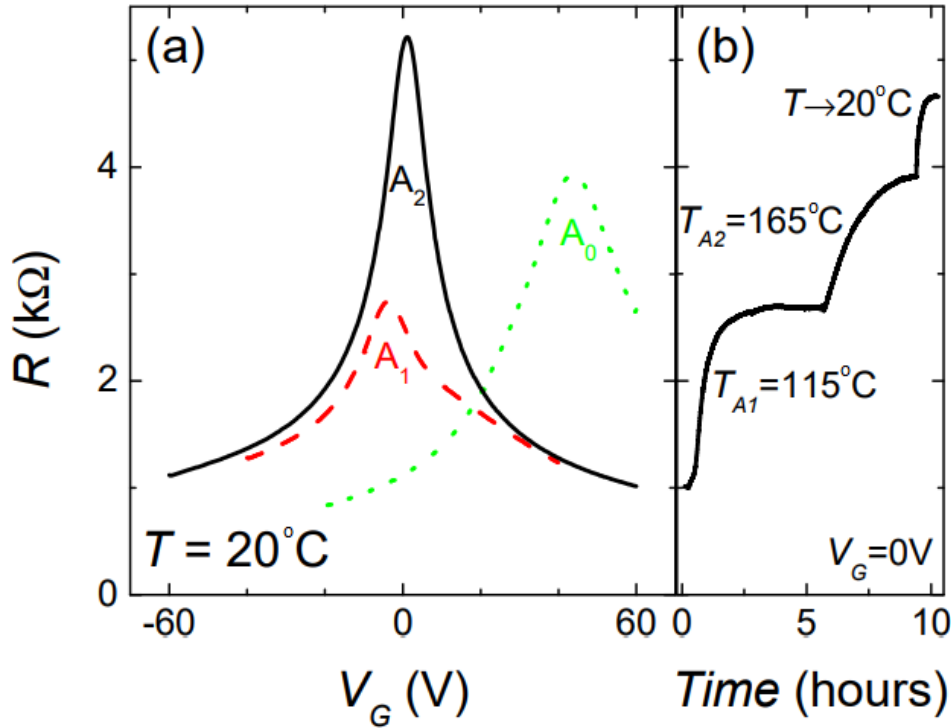
Figure 2.7: Figure **(a)**, the transfer curve for graphene at three stages of the annealing process. First, a gate sweep before annealing was done (green, dotted) graph A_0. Next, a gate sweep after annealing at $115\,°C$ was done (red, dotted) graph A_1. Finally, a gate sweep after annealing at $165\,°C$ was done (black) graph A_2. After annealing the Dirac peak shifted to $V_G = 0\,V$ and at higher annealing temperatures the quality and homogeneity were improved which could be seen from the reduced width of the Dirac peak in (black) graph A_2. Figure **b**, the rise in annealing temperature over time at $V_G = 0\,V$ is shown with room temperature at $T_{A_0} = 20\,°C$ and annealing temperatures $T_{A_1} = 115\,°C$ and $T_{A_2} = 165\,°C$ [40].

---

[11] Deduced from the semi-classical Drude model [39].

2.5 Hydrogenation

Although graphite is nearly chemically inert, graphene can react with hydrogen to create graphane [12]. This reaction causes the zero band gap semiconductor to become an insulator with a band gap. In this process, the hybridization of the carbon atoms changes from sp^2 to sp^3 which removes the π-bands and opens an energy band gap of a maximum of $3.9\,eV$. This changes the transport properties, and electronic and atomic structure and decreases the conductivity. The added hydrogen atoms act as scattering objects influencing the electron flow [41]. For optimal hydrogenation during experiment, the samples were first annealed to remove contaminations. Next, the sample was exposed to a cold, low-pressure hydrogen-argon mixture (10% hydrogen). Between two aluminium electrodes, a cold hydrogen plasma was created to hydrogenate graphene. Via the cold plasma treatment, it was also possible to extend beyond hydrogenation namely, oxidation, nitrogenation, and fluorination. The plasma reached saturation after exposure for $\sim 2h$ at a distance of $\sim 30\,cm$ from the electrodes. Two major advantages of cold plasma hydrogenation are simplicity and tunability. The method is simple because there is little risk of contaminating graphene due to the limited amount of particles present. In other methods, e.g. wet chemical hydrogenation, side reactions and contaminations appeared on the graphene. Also, the tunability of cold plasma is an advantage. The energy, temperature, composition, and electric field are all tunable. The disadvantage of cold plasma hydrogenation can cause damage and defects in the graphene. Another disadvantage is that special, experiment-specific equipment is necessary in creating a cold plasma for hydrogenation [41]. Figure 2.8 it is shown how the resistivity increased and the Dirac peak shifted to a higher gate voltage. At room temperature, the samples were stable for several days. It appeared also possible to anneal the samples again to practically return to their original state with a maximum close to $\frac{4e^2}{h}$. Despite the recovery of mobility, the samples remained p-doped. This might be caused by vacancies induced by plasma damage or residual oxygen during annealing [41, 42].
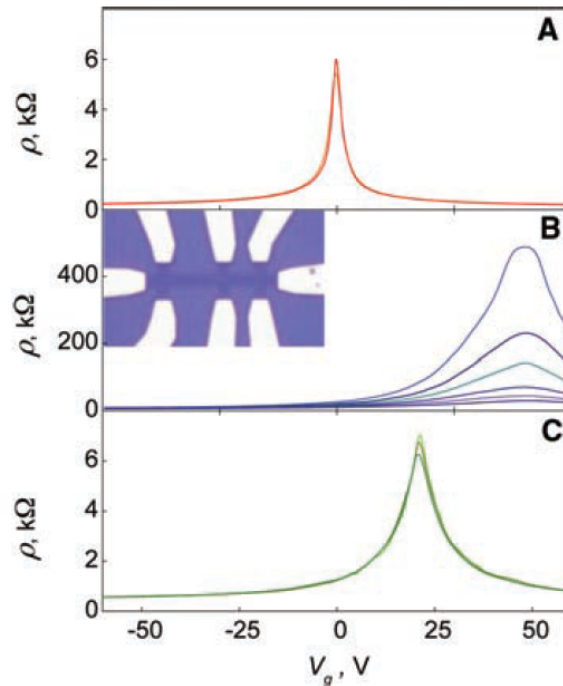
Figure 2.8: The resistivity as a function of the gate voltage of a graphene sample before and after hydrogenation and after annealing all in a zero magnetic field at various temperatures T. **A** shows the graphene sample before hydrogenation. In **A** the three different temperatures ($T = 40, 80, 160\,K$) overlap. In **B** the Dirac curve is shown after hydrogenation. In **B** the temperature increases from the top graph to the bottom graph ($T = 4, 10, 20, 40, 80, 160$). The inset in **B** shows a picture of a piece of graphene with eight connection points for measurement purposes. In **C** the graphene sample after annealing is shown. In **C** the temperature increases from the top graph to the bottom graph ($T = 40, 80, 160$), which nearly overlap [42].

---

[12]Graphane is created by attaching a hydrogen atom to each site of the graphene.

3 Decay

In 1896 Becquerel discovered radiation from uranium-bearing rocks. Curie and Rutherford also investigated radiation and it became clear that there are three types of radiation: alpha (α) radiation, beta (β) radiation, and gamma (γ) radiation. It was discovered that α and β radiation changed the characteristics of the element. α particles were helium nuclei and β particles were electrons. γ radiation appeared to be energetic photons (electromagnetic radiation). The three types of decay will now be shortly elucidated.

α **decay** Mostly heavy nuclei with atomic number (Z) > 82 decay via α decay. α particles are emitted rather than other light nuclei because of the high stability and tightly bound structure of the α particle. The released energy for α decay (Q_α) is given by the difference in mass energy between the parent nucleus, daughter nucleus, and α particle. This is given in Eq. 3.1

$$Q_\alpha = (m_P - m_D - m_\alpha)c^2, \tag{3.1}$$

where m_P indicates the mass of the parent, m_D indicates the mass of the daughter, m_α indicates the mass of the α particle and c is the speed of light. During a decay process, momentum between the daughter and the α particle must be conserved [13], and calculations can be reduced to a one-dimensional situation. The general decay equation for α decay is given by Eq. 3.2

$$^{A}_{Z}X \rightarrow\ ^{A-4}_{Z-2}X^{'} +\ ^{4}_{2}\alpha, \tag{3.2}$$

where A is the mass number of nucleus X, and Z is the atomic number of nucleus X [43].

β **decay** Another decay possibility is via β decay. When a nucleus emits a negatively charged electron, the charge of the nucleus increases by one unit. It is also possible to emit a positively charged electron (positron). In that case, the charge of the nucleus decreases by one unit. α decay happens at a specific energy. The energy spectrum of α decay is zero everywhere except at one energy. For β decay, an energy spectrum is created. The spectra for both α and β decay are shown in figures 3.1 and 3.2 respectively.
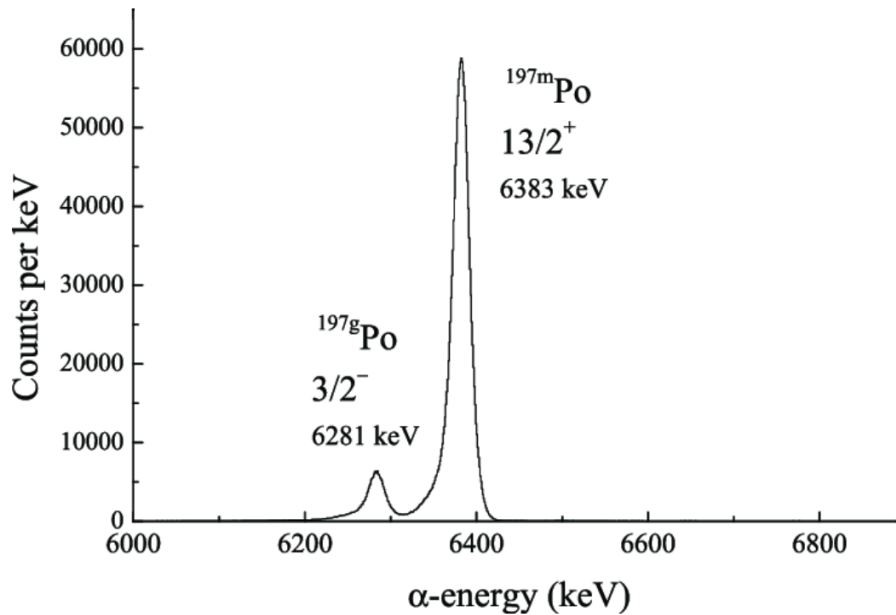
Figure 3.1: A typical α decay energy spectrum (for Po-197). In contrast with the text, not one peak but two peaks are visible, each at one specific energy. This is due to different (discrete) energy states available for the alpha particle. The first peak is for the ground state decay of Po-197 with state $3/2^-$ the second peak is for the excited Po-197 (indicated with an additional m) with state $13/2^+$ [44]

---

[13]Here it is assumed that the parent particle is at rest.
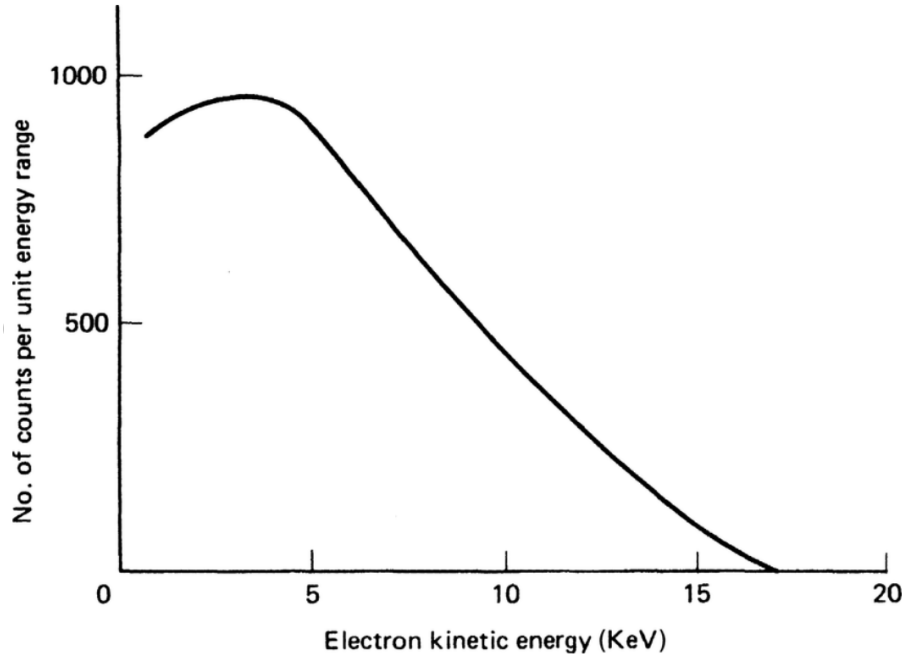
Figure 3.2: A typical β decay energy spectrum (for tritium). A spectrum is created due to the three-body decay for tritium $^3\text{H} \longrightarrow {}^3\text{He}^+ + \text{e}^- + \bar{\nu}_e$. For tritium, the endpoint of the energy spectrum lies around $18\,keV$. The endpoint is expected to go to higher energies then reality shows us. This small difference in expected value and measured value was due to the mass of the neutrino [45, 46].

The maximum energy spectrum of β decay is lower than expected from the energy-mass relation. With the introduction of the nearly undetectable neutrino (ν), β decay appeared to be a three-body decay [14]. Considering β decay with an e^- emitted it is possible to think about a neutron transforming into a proton, electron, and (electron) anti-neutrino ($n \rightarrow p + e^- + \bar{\nu}$). This type of decay is connected with the weak nuclear force. β decay can only happen if the daughter nucleus is lighter than the parent nucleus due to energy conservation [43]. The general decay equation for β decay is given by Eq. 3.3

$$^A_Z X \rightarrow\ ^A_{Z+1}X^{'} +\ ^0_{-1}\beta +\ \bar{\nu}. \tag{3.3}$$

γ **decay**   The last decay possibility is via γ decay, which happens to excited nuclei. When an excited nucleus falls into a lower energy state the nucleus remains the same although it emits a small energy in the form of a γ ray (photon). This type of decay is connected with the electromagnetic force. The general decay equation for γ decay is given by Eq. 3.4

$$^A_Z X^* \rightarrow\ ^A_Z X +\ ^0_0 \gamma, \tag{3.4}$$

where X^* represents the excited nucleus [43].

---

[14]The nucleus, the electron and the neutrino.

3.1 β decay detailed

In this section, β decay is explained in more detail. As explained before, unstable nuclei can emit β particles to optimize the ratio of neutrons and protons. Via the weak nuclear force, a neutron is transformed into a proton, electron, and (electron) anti-neutrino where energy, momentum, and lepton number are conserved. The probability of β decay depends on various factors i.e. energy released in decay, charge and angular momentum of emitted particles, and the initial and final state. By using Fermi's golden rule [47] it is possible to analyze the transition rate between initial and final states [48]. This rate is given by Eq. 3.5

$$\lambda = \frac{2\pi}{\hbar}|M|^2\frac{dn}{dE} \ , \tag{3.5}$$

with E (in the derivative) the available energy in the final state, $\frac{dn}{dE}$ the phase-space factor (density of final states). The phase space describes how the particles are emitted. M is the matrix element of the transition. The matrix element contains details of the nuclear structure and transition. The matrix element has the form of Eq. 3.6

$$M = \int \psi_f^* H \psi_i d\tau, \tag{3.6}$$

H is the Hamiltonian which describes the interaction of the transition between the initial and final state of wave functions ψ_i and ψ_f [43]. This matrix element and the phase space will be discussed in more detail.

   An important characteristic of β decay is the energy spectrum. The three particles after β decay each have a non-zero mass. Although the mass of the neutrino (m_ν) is determined to have an upper limit of a few eV and is often taken to be zero. With the knowledge of the three-particle decay, it becomes directly obvious that an energy spectrum arises. Most of the energy available after the decay is absorbed by the daughter particle, which is massive compared to the leptons. Due to this large mass, it will have a small kinetic energy and is thus often taken to be zero [49]. The leptons do have a non-zero kinetic energy which depends on the phase-space factor and Coulomb interaction between the β particle and daughter nucleus. To give an idea about the energy released, the Coulomb interaction will be neglected. Later, we will include this using a Fermi function [43]. The nuclear energy released (E_0) will be shared between the β particle and neutrino [15] as $E_0 = E_\beta + E_\nu$. By taking into account that the β particle does have a non-zero rest mass of $m_\beta c^2 = 511\,keV$ the kinetic energy for the β particle is $E = E_\beta - m_\beta c^2$. At the endpoint of the β spectrum, the β particle has its maximum energy ($E_{max} = E_t - m_\beta c^2$). The number of available states for the β particles with a specific momentum in a volume can be found by using the density of states (DoS) $\rho(E)$. The DoS gives the number of available states per energy for the volume. A set of positive integers (n_x, n_y, n_z) describe the allowed quantum states (in a box). It is possible to define $n = \sqrt{n_x^2 + n_y^2 + n_z^2}$ which corresponds with a specific energy $E = \frac{h^2 n^2}{8ma^2}$. The number of states between energies E and $E + dE$ is given by Eq. 3.7 which is obtained by multiplying the DoS at a specific energy by dE

$$\rho(E)dE = V\frac{2^{\frac{5}{2}}\pi m^{\frac{3}{2}}}{h^3}\sqrt{E}dE, \tag{3.7}$$

E is the kinetic energy of the particle and V is the volume containing the particles. The DoS can also be linked with the (magnitude of the) momentum via $p = \sqrt{2mE}$. By using the substitutions $\sqrt{E} = \frac{p}{\sqrt{2m}}$ and $dE = \frac{pdp}{m}$ Eq. 3.8 can be obtained

$$\rho(p)dp = V\frac{4\pi p^2 dp}{h^3}. \tag{3.8}$$

This analysis is for standing waves but for traveling waves the same procedure is valid. Although, traveling waves would need periodic boundary conditions. The volume for the allowed states is $4\pi n^2 dn$ which can be obtained by substituting $p = \frac{hn}{a}$ in Eq. 3.8, note that $V = a^3$ [43]. Eq. 3.8 gives the DoS with the momentum included. This gives the number of available states for the electron but it could also be used for the neutrino. When combining these two expressions as in Eq. 3.8 (one for the β particle and one for the neutrino) Eq. 3.9 is obtained

$$dn = \rho(p_\beta)dp_\beta\rho(p_\nu)dp_\nu = \frac{(4\pi)^2 V^2 p_\beta^2 dp_\beta p_\nu^2 dp_\nu}{h^6}. \tag{3.9}$$

---

[15]It is assumed that the daughter nucleus has no kinetic energy.

This expression gives the number of available states for both particles. Looking at the energy of the neutrino with assumed mass, $m_\nu = 0$ the expression $E_\nu = p_\nu c = E_0 - E_\beta$ is obtained. For a fixed electron energy it follows that $dp_\nu = \frac{dE_0}{c}$. Substituting these results in Eq. 3.9 a relation for the phase-space and energy and momentum of the β particle can be obtained as

$$\frac{dn}{dE_0} \propto p_\beta^2 (E_0 - E_\beta)^2 dp_\beta. \tag{3.10}$$

To account for the Coulomb interaction a Fermi function $F(Z, E_\beta)$ is included. With Z the atomic number of the daughter particle. Substituting Eq. 3.10 into Eq. 3.5 an expression for differential decay probability per unit time for β particles with momenta in the range p_β to $p_\beta + dp_\beta$ can be obtained

$$d\lambda(p_\beta) = C|M|^2 F(Z, E_\beta) p_\beta^2 (E_0 - E_\beta)^2 dp_\beta, \tag{3.11}$$

with C as a constant.

Integrating over the matrix element in Eq. 3.6 a factor of $\exp(-i\frac{\boldsymbol{P} \cdot \boldsymbol{r}}{\hbar})$ pops up. $\boldsymbol{P}$ is the vector sum of the electron, and neutrino momenta ($\boldsymbol{P} = \boldsymbol{p_e} + \boldsymbol{p_\nu}$). $\boldsymbol{r}$ is the coordinate of the decaying nucleon. Substituting typical values result in a small number in the exponent which can be replaced with 1 [16] for $r \leq R$ [17]. With this, the matrix element appears to be independent of the momenta of the electron and neutrino. If it is possible to use this approximation the transition is called an 'allowed' transition. To determine the endpoint for these β decay spectra a Fermi-Kurie plot is most convenient as shown in figure 3.3. Linear Fermi-Kurie plots indicate that the leptons do not carry away any orbital angular
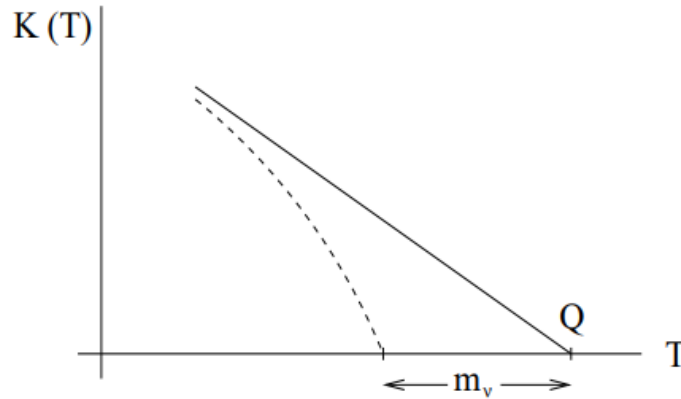
Figure 3.3: The endpoint of the Fermi-Kurie plot for tritium decay. For a non-zero neutrino mass, the endpoint of the spectrum deviates from the straight-line T-dependence. Here T is the kinetic energy of the released β particle. If $m_\nu = 0 \to T_{max} = Q$ and if $m_\nu \neq 0 \to T_{max} = Q - m_\nu$ [50].

momentum. If orbital angular momentum is carried away the Fermi-Kurie plot is not linear [48]. The total decay rate obtained from Eq. 3.11 is

$$\lambda = C|M|^2 \int F(Z, E_0) p_\beta^2 (E_0 - E_\beta) dp_\beta = C|M|^2 f(Z, E_0). \tag{3.12}$$

$f(Z, E_0)$ is a function heavily dependent on the endpoint energy (T_0) [18].

β decay can thus be expressed in terms of $f(Z, E_0)$ and the half-life ($t_{1/2} = \frac{\ln 2}{\lambda}$ as will be shown in section 3.2). Multiplying $f(Z, E_0)$ and $t_{1/2}$ gives the comparative half-life which is proportional to $|1/M|^2$. This separates nuclear physics from the phase-space effects. Due to the large variation in the order of magnitude of the comparative half-life, it is convenient and often uses a logarithmic scale as $\log_{10} f(Z, E_0) t_{1/2}$ with $t_{1/2}$ in seconds [43]. As discussed before, for allowed transitions it was possible to replace the exponential with 1 due to the small value in the exponent. If the transition does not follow selection rule [19] the matrix element is zero. In the case that the exponential is not small, the

---

[16]Note that 1 represents the identity matrix.

[17]Typical values are $\boldsymbol{P} = m_e c$ which gives $\frac{P}{\hbar} = \frac{1}{386} fm^{-1}$. $R = 4 fm$ so $\frac{PR}{\hbar} \approx 0.01$.

[18]Approximately depended on the fourth power.

[19]Not given in this thesis.

previous approximation is not applicable. The exponential can then be expanded as a power series of $\frac{\boldsymbol{P} \cdot \boldsymbol{r}}{\hbar}$. Terms in this expansion depend on polar angles and vector $\boldsymbol{r}$. Thus the orbital angular momenta are greater than zero. This gives rise to the 'forbidden' transitions, which will not be discussed in detail. The 'superallowed' transitions also exist and refer to β decay with a strong overlap in initial and final nuclear states [20]. Forbidden decays (with a different energy spectrum) deviate from this behaviour but are not discussed in detail [43].

3.2 Radioactive decay

Radioactive decay happens if unstable nuclei transform into stable nuclei [21]. The exact time nuclei decay is hard to determine due to the randomness of radioactive decay. The best measure to specify a decay time is the half-life $t_{1/2}$. This is the time half of the nuclei in the sample have decayed [43]. Eq. 3.13 describes the number of radioactive nuclei N present at time t

$$\frac{dN}{dt} = -\lambda N, \tag{3.13}$$

where N is the number of radioactive nuclei in the sample and λ is the decay constant which is the probability per time unit that a nucleus will decay. In the case of more than one decay product, λ is the sum of all the decay probabilities. The decrease in radioactive nuclei is accounted for by the minus sign. Eq. 3.13 has the solution

$$N(t) = N_0 e^{-\lambda t} = N_0 e^{-\frac{t}{\tau}}, \tag{3.14}$$

with N_0 the number of nuclei at $t = 0$ and τ is the mean life or the average lifetime of a nucleus which can be defined as $\tau = \frac{1}{\lambda}$. It can be seen that the half-life, mean life, and decay constant can be related to each other [22]. The activity of a radioactive source is given by

$$A = -\frac{dN}{dt} = \lambda N = N \frac{\ln 2}{t_{1/2}}, \tag{3.15}$$

and has units of becquerel (Bq).

3.3 Range of β particles

When radiation meets matter there is a probability that particles collide with the matter. It is also possible to talk about the mean free path (the distance a particle does not collide with the matter). If a (charged) particle collides with matter it loses energy. How far a particle penetrates matter depends on the type of particle, its energy, and the material it flies into. This distance is called the range of the particle. For electrons, the range can fluctuate by an order of magnitude. This is caused by the energy transfer per collision and the possible emission of Bremsstrahlung. It is possible to experimentally determine the range of a particle. To do this, a beam of particles with specific energy passes the material in question. The ratio of the transmitted to incident particles can be measured and is called the transmission coefficient. Due to the energy spectrum of β particles, it is possible to approximate this in an exponential form which can be shown by Eq. 3.16

$$I = I_0 e^{-\mu x}. \tag{3.16}$$

I is the intensity at a certain distance, I_0 is the intensity at zero distance at the source, x is the distance from the source and μ is the β-absorption coefficient. The coefficient is directly related to the endpoint energy of the β spectrum and the density of the material, ρ. The exponential absorption behaviour of β decay particles only happens to allowed decays, due to its continuous energy spectrum [51].

---

[20] Tritium decay into Helium-3 is one of these decays.

[21] It is possible for unstable nuclei to transform into other unstable nuclei but eventually stable nuclei are formed.

[22] $t_{1/2} = \frac{\ln 2}{\lambda} = \tau \ln 2$

4   Materials

4.1   Graphene sample

A field-effective transistor (FET) is an electrical component in which the current is controlled by nearby electric fields and their associated voltage differential. A FET usually has three terminals: a source, a drain, and a gate. The source and drain where a semiconductor (or in our case graphene) channel runs between the electrodes of the source and drain. The gate is the control mechanism that depends on the applied voltage differential. The higher the gate voltage, the larger the charge transport through the channel [52].

An essential item for the PTOLEMY project was graphene. In this project, a graphene field-effective transistor (GFET) fabricated by Graphenea [23] was ordered. The specific model was the GFET-S10. The graphene was obtained via chemical vapor deposition as explained in 2. This method deposited the graphene on a SiO_2 wafer which was placed on a Si wafer as shown in figure 2.1. Golden contacts were placed for measuring (electronic) properties of graphene. The GFET channels were extremely sensitive (high mobility), due to the one-layered structure of graphene. Other, grapheneless, field-effective transistors (FET) were 3D which limited their mobility drastically because 3D FET surface currents do not necessarily penetrate the channel. The GFET was 2D, thus no penetration deeper into the channel was needed [52]. On one GFET-S10 chip, 36 graphene devices in a grid pattern were provided as shown in figure 4.1. 30 of those devices had a Hall-bar geometry and the remaining 6 had a 2-probe geometry. The Hall-bar devices were used for Hall measurements and 4-probe measurements. Different devices had different graphene channel dimensions to investigate the geometry dependence of devices [53]. Measurements on the transfer curve of the GFET-S10 were done by Graphenea. They obtained a transfer
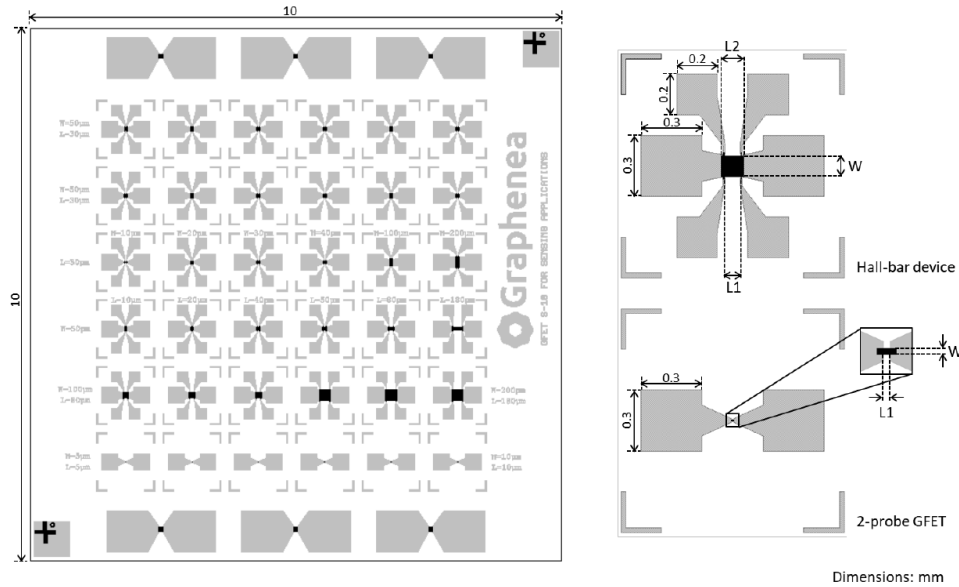
Figure 4.1: The 36 devices on a GFET-S10 chip. Each device has a different graphene channel dimension. The top picture on the right shows a Hall-bar device. The bottom picture on the right shows a 2-probe device [53].

curve comparable with figure 2.6 where a Dirac peak was found but slightly shifted to a higher V_G as shown in figure 4.2.

---

[23]Company could be found via: https://www.graphenea.com
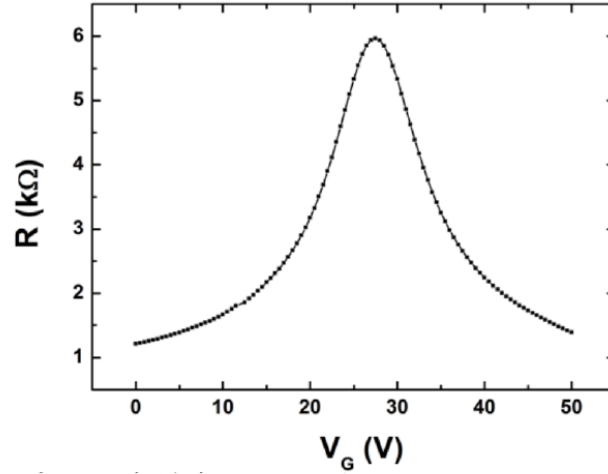
Figure 4.2: The transfer curve from a GFET-S10 device with a width and length of $50\,\mu m$. This measurement was done with a source-drain voltage V_{SD} of $20\,mV$, at room temperature in vacuum conditions. The Dirac peak was found around $V_G = 28\,V$ [54].

Field-effective measurements were often taken with a 4-probe setup. A source-drain voltage between the outer contacts was used and the current was measured between those contacts. Also, the voltage across the graphene over the inner contacts was measured as shown in figure 4.3. With the scheme as
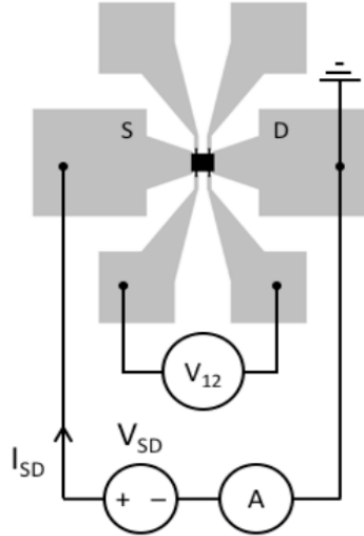
Figure 4.3: The scheme of the 4-probe measurement on a Hall-bar device. S and D represent the source and drain respectively. I_{SD} is the source-drain current, V_{SD} is the source-drain voltage applied, A represents a multimeter for current and V_{12} is a volt meter [54].

given in figure 4.3 and Eq. 4.1 it was possible to create the curve in figure 4.2

$$R = \frac{V_{12}}{I_{SD}}. \tag{4.1}$$

The advantage of this method was that only the resistance of the graphene channel was measured, and no voltage drops at the graphene-metal interfaces were included. The interfaces depended on V_G, but not in the same way as the graphene channel resistance. So, the 4-probe measurement was far more sensitive to applied gate fields or surface charge changes [54].

4.2   Desiccator

As mentioned in section 4.1, the graphene samples should be stored in an enclosed environment with as minimal contact with air or other contaminants such as water molecules as possible. A vacuum desiccator is perfectly suitable for this purpose because it encloses the inside from moisture from the air. A vacuum desiccator has a stopcock which is used to regulate the air inside the desiccator. This measure limits the amount of p-doping which shifts the Dirac peak to a higher positive V_G. This shift makes the graphene devices less useful or even unusable if the doping affects the graphene too much. During the entire project, the graphene will be stored in the desiccator in a vacuum environment and will only be exposed to its surroundings during actual measurements [55].

4.3   Radioactive source

In the PTOLEMY project, radioactive tritium will be used. The availability of tritium is too low and the price is too high to use this as a source in the test phase. A radioactive source with similar properties would be an ideal replacement for the test phase. A candidate with similar characteristics is strontium-90 (Sr-90). Sr-90 has a $t_{1/2}$ of $28.79\,yrs$, and a decay energy of $0.546\,MeV$ distributed over its decay products [24]. Sr-90 decays via β decay just as tritium does. The decay equation is shown in Eq. 4.2

$$^{90}_{38}Sr \rightarrow\,^{90}_{39}Y + e^- + \bar{\nu}_e. \tag{4.2}$$

The Sr-90 decay results in another radioactive particle: yttrium (Y-90) with a $t_{1/2}$ of $64\,h$ and a decay energy of $2.28\,MeV$ distributed over its decay products. This particle also decays via β decay as shown in Eq. 4.3

$$^{90}_{39}Y \rightarrow\,^{90}_{40}Zr + e^- + \bar{\nu}_e. \tag{4.3}$$

Zirconium is a stable nucleus that ends the decay chain [56].

4.4   Multi-pixel photon counter

A multi-pixel photon counter (MPPC) consists of several avalanche photodiodes (APDs) in a special operation modus (Geiger modus). An APD is a semiconductor photodetector working via the photo-electric effect. In this APD a p-doped and an n-doped side in between a depletion layer are present. The p-doped side has a lack in electrons (holes) and the n-doped side has extra electrons, leading to a neutral depletion layer with an electric field [57]. Incoming photons or thermal excitations can disturb the equilibrium in the PN junction. Disturbances with an energy larger than the band gap energy can create an electron-hole pair. An electron from the valance band is excited to the conduction band and leaves a hole behind. The electrical field will separate the holes and electrons to the p-side and n-side respectively. In an electrical circuit, only a current is measurable if the current exceeds the noise. This process only works if the disturbances happen inside the depletion layer. Outside of the depletion layer the electron and hole will recombine. By applying a reverse bias voltage (V_R) the recombination can be prevented. The higher the V_R, the stronger the electrical field. This results in a higher kinetic energy for charge carriers which is lost in a collision. If the average kinetic energy is larger than the band gap energy a collision would initiate a new electron-hole pair which are both accelerated due to the potential difference. This process grows exponentially and can be thought of as an avalanche effect [25]. In this way a small disturbance can result in a large current that exceeds the noise. The increase of the initial to the final signal is called the gain M. A typical relation between the gain and the V_R is shown in figure 4.4. The higher the V_R, the higher the gain [58]. At $V_R \approx 140\,V$ the curve becomes extremely steep [26]. The voltage at which this happens is called the breakdown voltage (V_{br}). If a V_R is chosen above the V_{br} the APD is in Geiger modus. In Geiger modus, only a single electron-hole pair is needed to start the avalanche effect. This avalanche can thus be initiated by a single photon. Due to this sensitivity, the APD would give a signal easily. In an APD a protection mechanism is implemented which resets the APD via a short recovery time where no photons can be detected [59]. For the APD in Geiger modus the gain can be defined as in equation 4.4

---

[24] Tritium has a $t_{1/2}$ of $12.32\,yrs$ and a decay energy of $18\,keV$.

[25] Hence the name: avalanche photodiode.

[26] With a fitted trend line for the middle region a relation between the gain and V_R is approximately $10^{\alpha V}$.
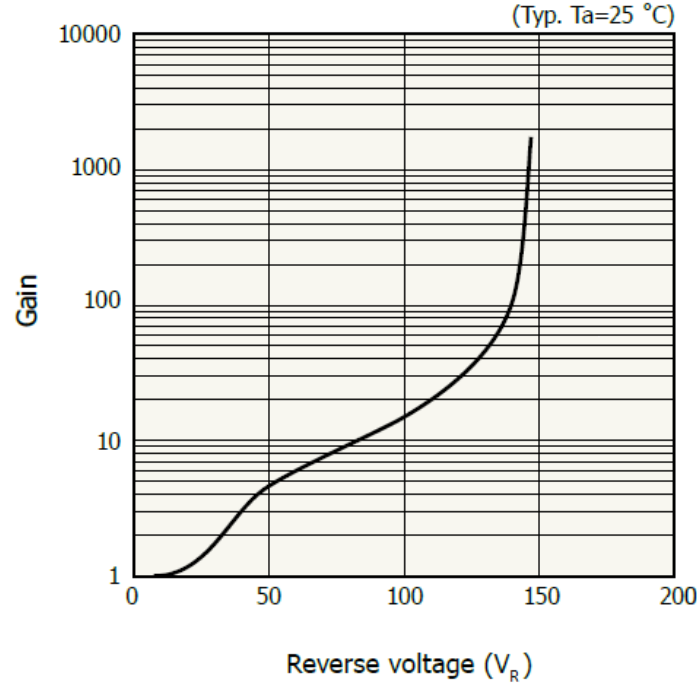
Figure 4.4: The relation between the gain and the V_R in an APD [57].

$$M = \frac{Q}{q} = \frac{C \cdot (V_R - V_{br})}{q}. \tag{4.4}$$

With charge Q dependent on the reserve bias voltage V_R, breakdown voltage V_{br} and the capacitance C of one pixel. q is the charge per electron. The gain is not only dependent on the V_R but also the temperature. At high temperatures, phonons vibrate more which decreases the mean free path of charge carriers. This will slow down the average speed of the charge carriers and fewer ionizing collisions take place. So, with a higher temperature, the gain is smaller. Another temperature-dependent characteristic of the MPPC is the dark count rate (DCR). Due to thermal excitations, electron-hole pairs can be created which would start an avalanche that is indistinguishable from an avalanche started via a photon.

There are two main solutions to this temperature noise. The first one is to cool the system so the temperature is maintained. The second solution is possible if it is known when the photon will arrive. By allowing photons for a small time window in the order of ns the probability for a dark count becomes 0.1%. Noise can also appear from after-pulses. During the avalanche process, some charge carriers can be trapped for a few ns due to impurities of the APD. These delayed charge carriers can initiate new avalanches several ns later, hence the name after-pulses. After-pulses are shown in figure 4.5 If the after-pulse falls in the recovery time of the MPPC their amplitude is shorter than regular pulses. This can be filtered in the data processing. If the after-pulses appear after the recovery time it is indistinguishable from an ordinary signal. With a time-delay filtering algorithm, these pulses could be excluded as well [59]. Another noise source for the MPPC is (optical) crosstalk. During the avalanche process charge carriers have kinetic energy which is not necessarily used for avalanche multiplication. Some of that energy is lost to phonon vibrations, but it is also possible that some of the energy is converted to photons.
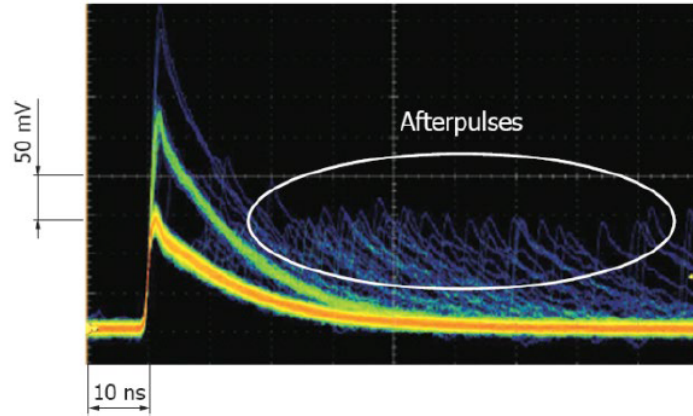
Figure 4.5: After-pulses of an MPPC [57].

These newly created photons can travel to neighboring MPPC pixels and start a new avalanche. It is called prompt crosstalk if an avalanche process is a result of the emitted photon and the output appears simultaneously as the original pulse this is shown in figure 4.6. This noise is only possible to filter if the
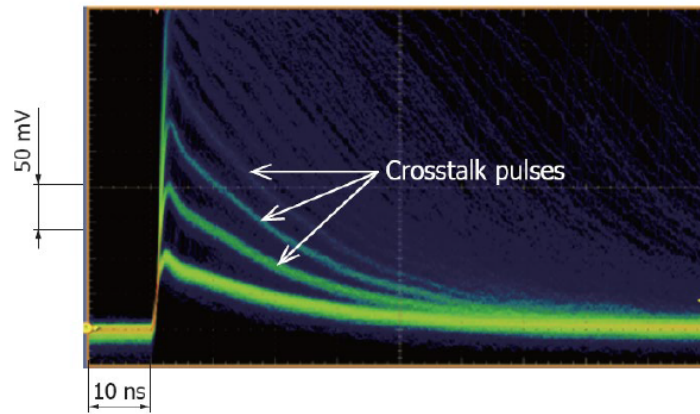
Figure 4.6: Prompt crosstalk of the MPPC [57].

created electron-hole pair (from the emitted photon) has a delay compared to the original pulse. This is called delayed crosstalk [57]. As stated before, the gain is larger for higher V_R, but also the noise increases with higher voltages. For optimal results of the MPPC (and APD), it is crucial to select a temperature and a gain/voltage which causes minimal noise at the Geiger-modus of the APD [27].

---

[27]In Geiger-modus, the APD is extremely sensitive to light and a light-tight setup is necessary.

4.4.1 MPPC evaluation circuit

To measure signals from the MPPC an evaluation circuit was needed. During measurements, the C12332-02 circuit produced by Hamamatsu was used. The circuit consisted of the sensor circuit board and the power supply circuit board as schematically shown in figure 4.7. The MPPC could be connected to the
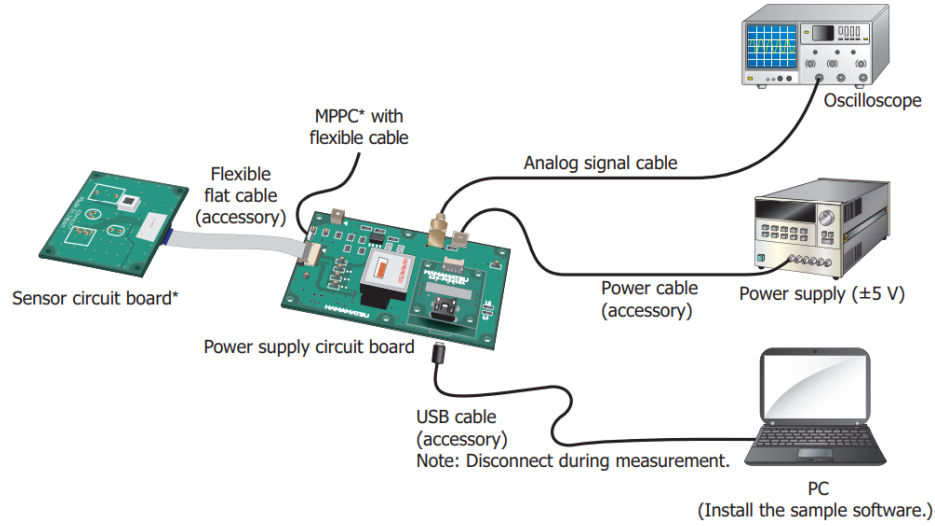
Figure 4.7: The entire setup for the MPPC evaluation circuit with all necessary equipment [60].

sensor circuit board. The power supply circuit board provided the power for the MPPC. An external power supply could be connected to supply the necessary voltage of $\sim 5\,V$. A PC was connected to the power supply circuit board with a USB cable to set the operating voltage of the MPPC [28]. To read the output current of the MPPC an oscilloscope was connected to the power supply circuit board via an analog signal cable.

---

[28]The PC needed the sample software.

4.5 Scintillator

A scintillator is a material that can absorb ionizing radiation such as β radiation and in turn emit photons with a wavelength corresponding to the type of transition. In combination with an MPPC, a scintillator becomes a scintillator detector. Thus the scintillator absorbs the incoming ionizing particle and emits a photon. The photon is detected in the MPPC which can convert this into a measurable electronic signal. Scintillators are extremely effective in detecting β radiation (electrons). The large scattering angle of electrons could result in electrons leaving the scintillator material without depositing all their energy into the material. The higher the atomic number of the scintillator material, the higher the rate of back-scattered electrons. For low-energy electrons [29], materials with a low atomic number are the most effective [51]. During this project, an EJ-208 scintillator from Eljen Technology and a BC408 scintillator are used.

4.5.1 EJ-208 scintillator

The EJ-208 scintillator is a plastic scintillator with a wavelength of maximum emission $\lambda_{max} = 435\,nm$. In figure 4.8 the emission spectrum of the EJ-208 scintillator is shown. This scintillator also has a high light attenuation length of $400\,cm$. The attenuation length is the distance a particle can travel through a material where the intensity of the beam has dropped to 63% [30] [61].
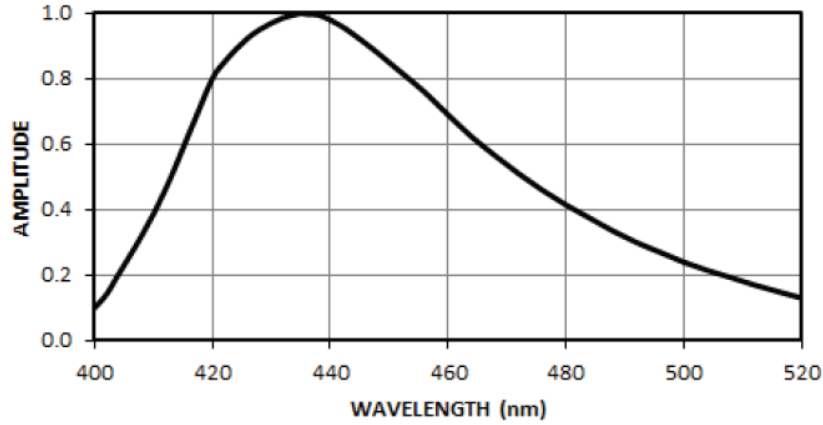
Figure 4.8: The emission spectrum of an EJ-208 scintillator [61].

---

[29]Electrons with energies smaller than $10\,MeV$.
[30]Coming from $\frac{1}{e}$ with e Euler's number.

4.5.2 BC-408 scintillator

The BC-408 scintillator is a plastic scintillator with a wavelength of maximum emission $\lambda_{max} = 425\,nm$. In figure 4.9 the emission spectrum of the BC-408 scintillator is shown. This scintillator also has a high light attenuation length of $380\,cm$. The BC-408 has the advantage of a large area [62].
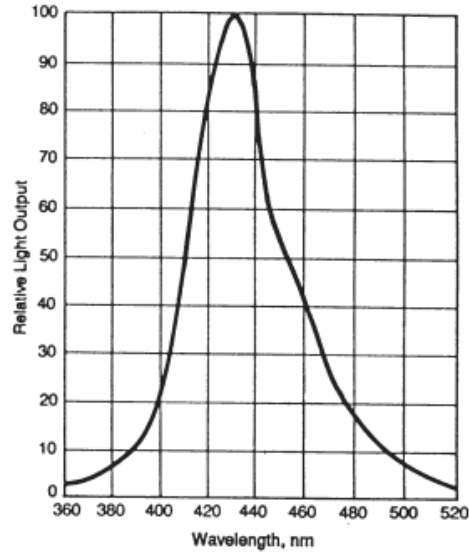
Figure 4.9: The emission spectrum of a BC-408 scintillator [62].

5 Setup

To capture β particles (and later neutrinos) with graphene, smaller, sub-experiments were performed. First, a small-range experiment with a β source and SiO_2 plates was performed. Second, the transfer curve of graphene must be measured with a reliable setup. With this setup, it should also be possible to recognize annealed and hydrogenated samples. Next, a reliable setup for the detection of β particles with a scintillator and photomultiplier should be created. If all these parts work properly as expected, a combination of these experiments can be created. This combination should be able to measure a transfer curve of the graphene if a β particle crosses and the photomultiplier should confirm the detection/change in the transfer curve.

5.1 Range experiment

In section 3.3 it is stated that the range of a β particle in matter has an exponential dependence on the amount of material. To check if β particles go through the graphene on a wafer and can be captured and converted by a scintillator, a simple setup was built. The setup tests the dependence for the range of the Sr-90 β particles and the Y-90 β particles with a decay energy of $0.546\,MeV$ and $2.28\,MeV$ respectively which is pointed at (a) SiO_2 wafer(s). As shown in figure 2.1 the graphene is delivered on a thin SiO_2 film on top of a Si wafer. The experiment was done with SiO_2 wafers due to their higher density compared to Si, $\rho_{SiO_2} = 2.65\,g/cm^3$ and $\rho_{Si} = 2.33\,g/cm^3$. The higher the density, the higher the β-absorption coefficient and thus a smaller intensity at a certain range as shown in Eq. 3.16.

5.1.1 Setup range experiment

The setup used is shown in figure 5.1. The setup consists of a radioactive source that provides the β particles for the experiment with an effective diameter of $\sim 0.3\,cm$. Above the source, a thick, metal disk with a hole of $\sim 0.3\,cm$ was placed. This disk was used to shield as much radiation from the surrounding (due to the divergence of the radiation) and only gave space to particles from the radioactive source. An additional advantage of the metal disk was that small SiO_2 wafers could be placed on top of it. The wafers had dimensions $1.0 \times 1.0\,cm^2$ and a thickness of $0.5 \pm 0.15\,mm$. The Geiger-Muller counter (GM counter) detection part with a detection diameter of $\sim 3.2\,cm$ was placed above this disk to measure radioactive particles. Next to the setup, the screen of the GM counter was placed. This GM counter was placed downwards to limit the background radiation, mainly coming from the sky (above). The entire setup was aligned as well as possible by using a tripod. Later, the experiment was conducted for a second and third time with a slightly different setup which would be more comparable to the setup mentioned in 5.3.2 [31].
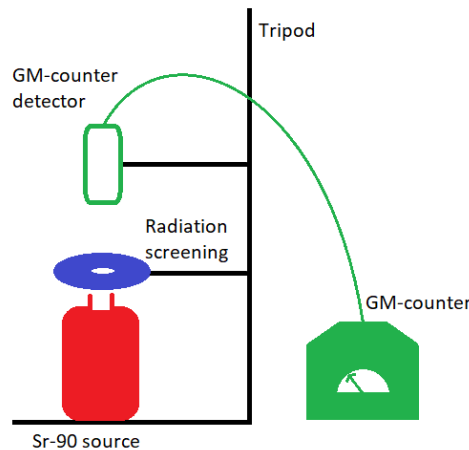
Figure 5.1: A schematic drawing of the setup. In red the radioactive source is shown where the β particles are pointed upwards. The blue ring with a hole is used as radiation screening and the place to put the SiO_2 wafers. In green a GM counter with its detector part above the source. All these parts are aligned as much as possible by using a tripod.

Results and findings about the range experiment can be found in subsection 6.1.

---

[31] At the time of run 1, no clear decision about the final setup for graphene detection was made yet.

5.2 Measuring graphene transfer curve

The transfer curve of graphene indicates the purity and amount of doping of the graphene as explained in section 2. Besides, it gives the possibility to recreate a resistance for a gate voltage. It is important to measure this transfer curve with high accuracy and stability for later detection purposes. In later stages, small perturbations of the resistance of this transfer curve will be measured due to the β particle crossing the graphene. If no stable transfer curve can be measured, the perturbations from the β particle are difficult to observable. In the search for the most reliable detection method, two setups were tested.

5.2.1 Probe setup

First (and unsuccessful), a probe setup was created to measure the transfer curve of graphene. In this setup (figure 5.2) the graphene samples, as shown in figure 4.3 and described in subsection 4.1, were connected via four conducting pins in a probe as shown in figure 5.2a. These pins were designed to make perfect contact with the Hall-bar devices. The pins were connected to Bayonet Neill-Concelman (BNC) wires.
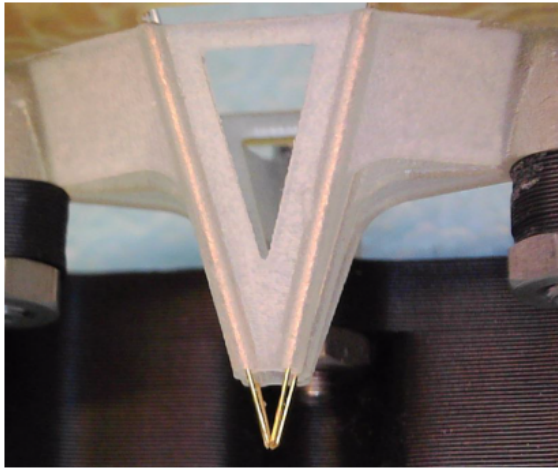
(a) The four contact pins. These pins are placed in a 3D-printed probe. The pins are placed in the exact positions to make contact with the Hall-bar devices.
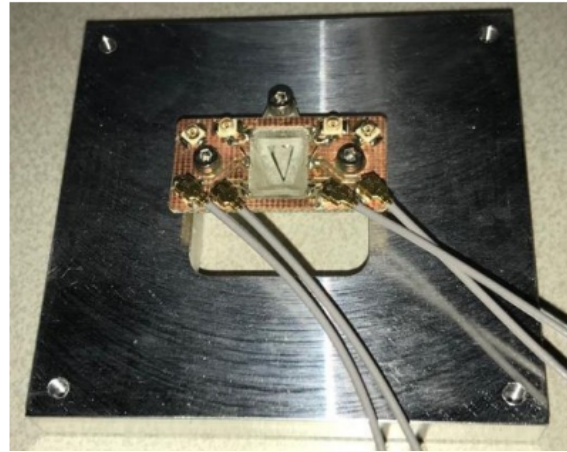
(b) The metal plate with the attached probe from the top, with the BNC cables.
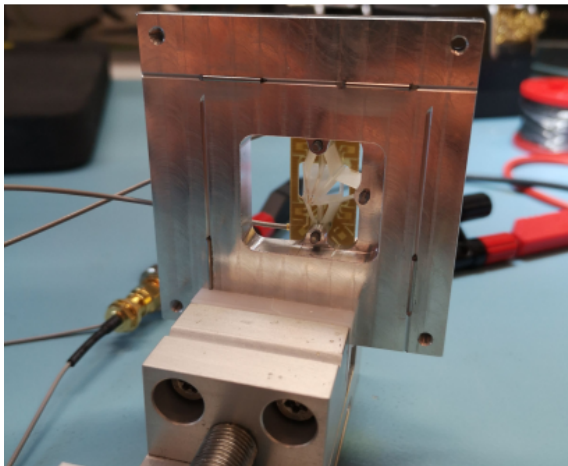
(c) The bottom of the probe plate. In the middle the probe with the four pins is visible. Around these pins (on three sides) there are small wrinkles.
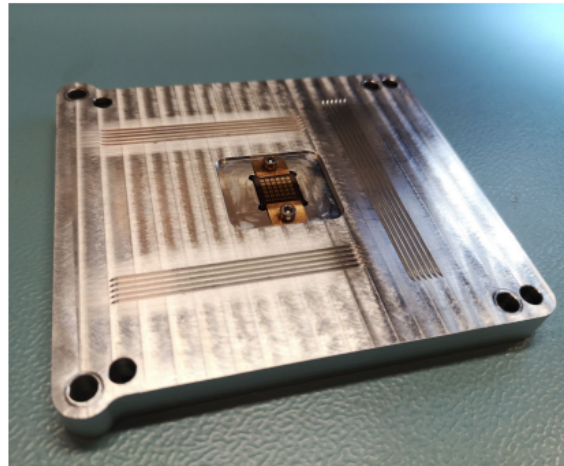
(d) The chip cutout. The copper holder can be seen on two sides of the chip. The grooves for the perfect alignment are also visible.

Figure 5.2: The parts of the probe setup. The setup can be created by screwing the plate from figure 5.2c on top of the plate in figure 5.2d.

The probe was attached to a metal plate as shown in figure 5.2b. The small wrinkles beneath the metal plate could be seen in figure 5.2c. The graphene field-effective transistor-S10 (GFET-S10) chip was placed in another metal plate with a perfect cutout for the chip as shown in figure 5.2d. With small copper holders, the chip was secured in place. On the metal plate grooves were carved so that when the probe plate was laid on top, the probe was perfectly aligned to connect with the connection points of a graphene sample. For a perfect placement despite the grooves, a microscope was used. With the microscope, it was checked if the pins in the probe connected to the Hall-bar connection points, which could create the circuit as shown in figure 4.3.

The source-drain voltage (V_{SD}) was connected to the outer contact and grounded at one side. This voltage transported the charge carriers through the sample. The source-drain current (I_{SD}) could be measured with a multimeter. A gate voltage (V_G) modulated the conductivity of the graphene sample via an electric field. The inner voltage (V_{12}) was measured across the graphene using the inner contacts with a multimeter. The advantage of the 4-probe measurement was explained in subsection 4.1. $V_{SD} = 20\,mV$ was applied and the V_G was increased from $0\,V$ to $50\,V$.

Measurements were done with two GFET-S10 chips. Unfortunately, the chips did not have the same dimension. One chip was slightly larger than the other one and had to be cut into the right dimensions. The first measurements seemed promising but after a few days, no sample worked, just as before.

Checking the contacts and pins with a multimeter gave an inconsistent signal. With the use of a strong microscope, the chips were inspected. This suggested the current setup needed improvements. One of the suggestions was to use a spring before each pin, so the mechanical pressure was limited. After careful consideration, the workload to accomplish this, combined with doubtful connections between the wires and pins the crucial decision to focus on a new setup was made.

Results and conclusions about the probe setup can be found in subsections 6.2.1 and 7.1.1, respectively.

5.2.2   Chip carrier setup

Due to the damaged graphene samples, a new setup to measure the transfer curve was needed. The new setup was called the chip carrier setup. In this setup, a chip carrier was used to place the graphene sample. Newly ordered graphene samples with polymethylmethacrylate (PMMA) on top were delivered. This layer was left on top so the graphene chip could be cleaved to the right size to fit in the chip carrier without contaminating the graphene samples with dust from the cleaving. The chips were cleaved along the black lines in figure 5.3
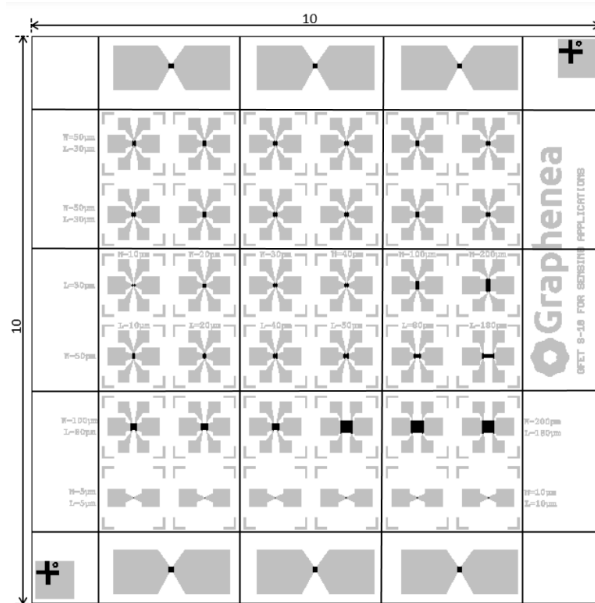
Figure 5.3: The cleaved lines for the GFET-S10 chip in black to obtain new smaller chips. The middle nine pieces are used during experiments [53].

The smaller chips were stored under vacuum conditions in a desiccator and only taken out for measurement purposes. The smaller chips were placed in a chip carrier. The contact was connected with extremely thin aluminium wires to the chip carrier as shown in figure 5.4. For the first measurement, the
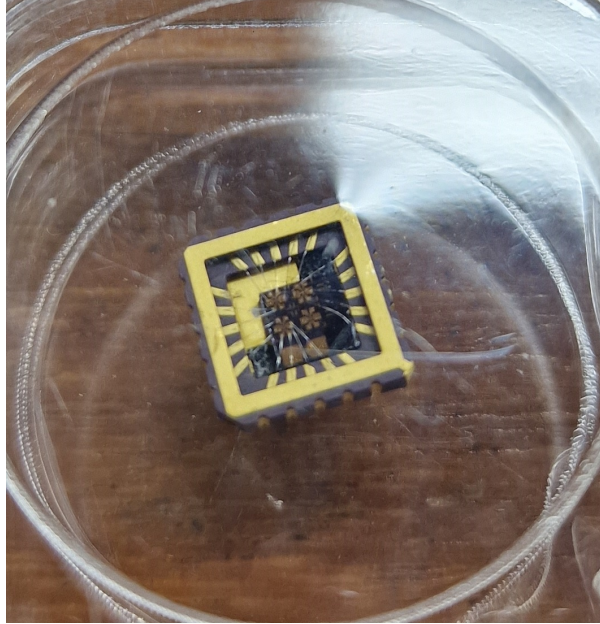
Figure 5.4: The cleaved chips in the chip carrier. From the golden connection points, thin silver-colored wires which are connected to the chip carrier are visible. This picture was taken moments after measurements inside a small plastic storage box (read to be stored in the desiccator again).

chip carrier was put in vacuum condition during the measurement. The resistance was measured with a back-sweeping V_G, with the start and endpoint both at $0\,V$. The second measurement was done in the same conditions but without the PMMA layer on top of the samples. The third measurement was done after annealing the samples to obtain the best quality possible for the graphene samples. Annealing was done at two temperatures i.e. $400\,K$ and $450\,K$.

Results and conclusions about the chip carrier setup can be found in subsections 6.2.2 and 7.1.2, respectively.

5.2.3 Hydrogenation box

To hydrogenate graphene a special setup was designed as shown in figure 5.5. Hydrogenation was done by exposing the graphene to a cold, low-pressure hydrogen-argon mixture. A hydrogen plasma was created between the electrodes. One of the electrodes is shown in figure 5.6. Depending on the amount of plasma created and the frequency of sparks created between the electrodes, the time and distance from the electrodes for the graphene were determined. Different configurations were tested during the hydrogenation and checked by measuring the transfer curve. For the hydrogenation, the setup from figure 5.5 was completed by attaching a gas inlet pipe for the hydrogen-argon mixture and connections for the electrodes with a high-voltage source as shown in figure 5.7. Later, pure hydrogen gas was used as well.
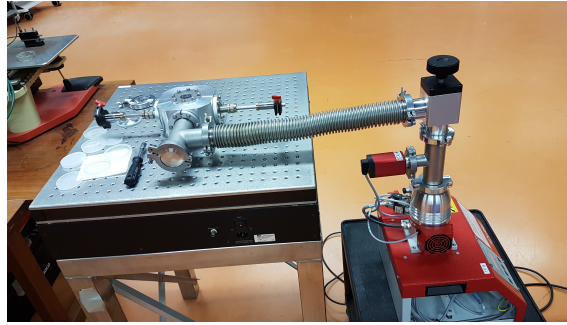
Figure 5.5: The hydrogenation box on top of an optical table. On the right of the picture the vacuum pump with a tube connected to the hydrogenation box. On the side of the hydrogenation box, two electrodes stick out (not connected to a high-voltage source). These sticks can be connected to a high-voltage source to create a spark inside the hydrogenation box.

Figure 5.6: One of the electrodes from the hydrogenation box. This electrode is designed to keep the hydrogenation box airtight but still able to adjust the position of the metal tip. The metal tip is shown on the right of the electrode. The black piece on the left is the connection for the high-voltage source.
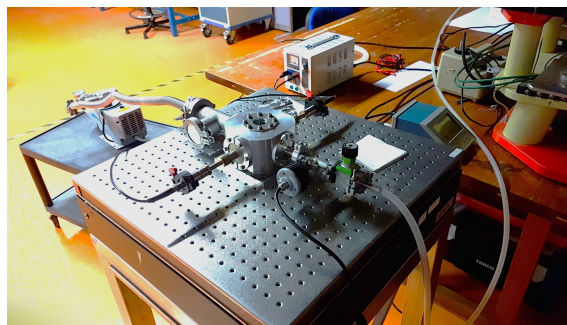
Figure 5.7: The hydrogenation setup. In the back (left in the picture) the vacuum pump just as in figure 5.5. Right above the hydrogenation box, the high-voltage source. This is attached to the electrodes to create a potential difference (and plasma). On the right, the gas inlet pipe. On this side is also a pressure sensor attached so the pressure inside the box was measured and controlled.

Results and conclusions about the hydrogenation box can be found in subsections 6.2.3 and 7.1.3, respectively.

5.3 Detection of β particles with photomultiplier

The β particle detection method with graphene is relatively new. To check if the resistance change in a GFET-S10 device is the result of a passing β particle, a reliable detection method must be used. A proven, reliable detection method is the combination of a photomultiplier and a scintillator. Where the resistance in the graphene is changed and a signal is measured in the photomultiplier. Two setups were tested.

5.3.1 Silicon photomultiplier setup

A silicon photomultiplier as explained in section 4.4.1 was used at first. To test the setup no graphene was used, just the detection of β particles was anticipated. The MPPC was connected to the sensor circuit board C12332-01. The power supply circuit board was provided with $\sim 5\,V$. To set the operating voltage, this board was connected to software installed on a PC. According to the datasheet, the breakdown voltage (V_{BR}) should be set to $3\,V$. It was important to find V_{BR}, so the scintillator and source were nicely aligned with the silicon photomultiplier. V_{BR} could be found by checking the reverse bias voltage which caused the Geiger to discharge. As the β particle was emitted from the source they entered the scintillator. The scintillator emitted photons that enter the silicon photomultiplier. This result was displayed on an oscilloscope which was connected to the power supply circuit board (after a set trigger level). The total setup is shown in figure 5.8.
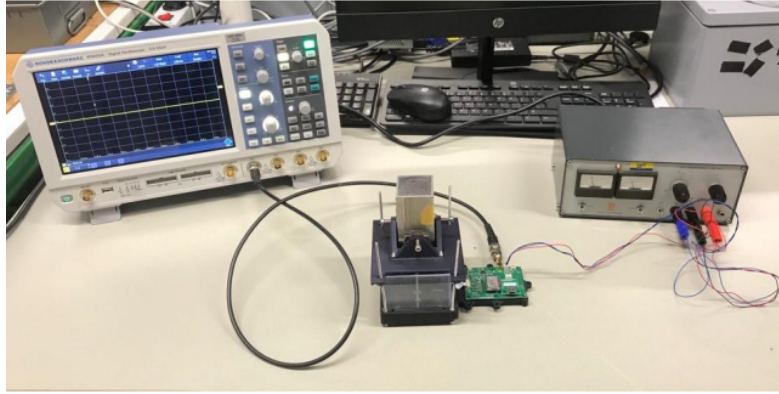
Figure 5.8: The total silicon photomultiplier setup. On the left, the oscilloscope is connected to the (green) power supply circuit board. The power supply circuit board is connected to the sensor circuit board (left from the green plate) under the transparent scintillator. On the right, an external power supply applies $\sim 5\,V$. On top of the scintillator, the radioactive Sr-90 source is located.

The photomultiplier was highly sensitive to photons. To improve the results as much as possible, measurements were executed in a dark room inside a specially designed metal box as shown in figure 5.9. The edges of the lid were later covered by black tape. The box was provided with the necessary connections.

Figure 5.9: The metal box with necessary connections. With this box, the setup is shielded as well as possible from incoming photons. The only photons that should be detected were from the scintillator.

Results and conclusions about the silicon photomultiplier can be found in subsections 6.3.1 and 7.2.1, respectively.

5.3.2 Scintillator setup

The other setup was the scintillator setup. This setup consisted of multiple components. In figure 5.10 this complete setup is shown. A nuclear instrumentation module (NIM) is shown on the left. These modules are often used in particle and nuclear physics. The flexibility in signal properties and change of instruments is a great advantage to organize the electronic properties of the setup. The NIM was connected to an oscilloscope, which was connected to the detectors. The top detector was set as a trigger to minimize the noise. Also gave the oscilloscope the possibility to count the number of detected events (taking the trigger level into account). The two detectors (two metal boxes) next to the oscilloscope detected the beta particles. Each box consisted of two chambers, in the front chamber, a scintillator (BC-408) was located. The scintillator was wrapped in aluminium foil and covered in black tape. Only a single part was not covered. This uncovered part was pointed to the other chamber via a covered tube. This tube ended in the photomultiplier. This entire detector setup was inside the box so a minimal amount of light could enter the detector. Although the metal box screened β particles, the NIM should still make a clear distinction between noise and source. On the right, the external power source for the photomultipliers was located.
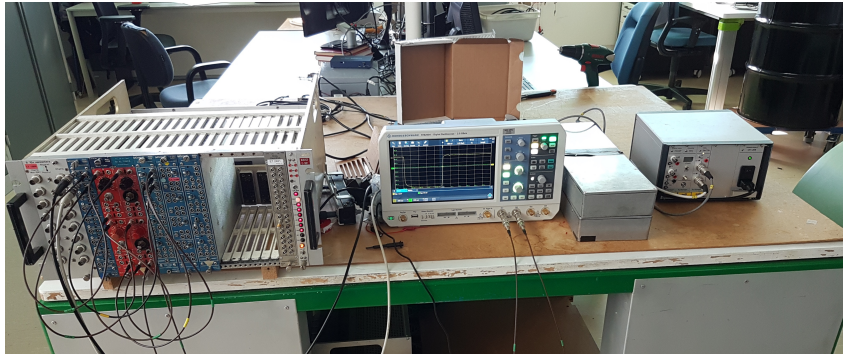
Figure 5.10: The total setup for the detection of β particles. On the left, the NIM. Next to that, the oscilloscope. Next to the oscilloscope, two detectors (metal boxes). Inside each box, there is a scintillator and photomultiplier. These boxes are the actual detectors. On the right, the external power source.

A new perfectly fitting lid for the scintillator was found. This lid had four holes that could be used to overcome the screening problem. The four holes were taped on both sides of the lid to prevent light saturation for the photomultiplier. Three out of the four holes were filled with tin grains to shield those holes as much as possible from the background. This new lid should improve the signal-to-noise (S/N) ratio significantly. This gave the ability to simplify the setup by losing the NIM and the second scintillator. The advantage of the NIM in combination with the second scintillator was expected to filter the background by $\sim 40\%$. The disadvantage was that the setup became much more complicated and it was difficult to tune the right parameters to reproduce measurements, which made these additions of the NIM and second scintillator unnecessary. Despite the simplified setup, the right trigger level on the oscilloscope should be set. The trigger level should be at a level where the S/N was as high as possible. For the best possible alignment of the source, a cardboard was cut out which perfectly placed the source on top of the hole. The cardboard was called the source alignment tool and gave a reliable and consistent placement of the source on top of the hole. With this setup, the scintillator was tested and the transmission coefficients (T) [32] could be determined from the counts measured. Also, the consistency in counts over time could be determined.

Results and conclusions about the silicon photomultiplier can be found in subsections 6.3.2 and 7.2.2, respectively.

---

[32]This was calculated as a fraction between the transmitted particles (counts for a wafer and source) and the total incoming particles (course for the source). $T = \frac{wafer - background}{source - background}$.

5.4   Concept setup for graphene as a particle detector

The scintillator setup was an ideal basis to test graphene as a (β) particle detector. Despite the ideal basis, some improvements on this setup should be made to be able to measure β particles. With the knowledge about the transfer curve of graphene, it should be possible to measure the charge β particles. Around the Dirac point, the two steepest parts of the transfer curve can be found. With the right V_G, it was possible to select a point on this steep part of the curve. A small change in the current created a large change in resistance as shown in figure 4.2. This change might have been the result of a β particle passing or colliding with the graphene. With the scintillators from the scintillator setup, it was possible to measure β particles. By reusing parts from the probe setup a new complete setup for the detection of particles with graphene could be made. With this setup, graphene could measure β particles and the scintillator could check what fraction of β particles were detected. Initially, the new setup started with the same structure as the scintillator setup. The same settings on the oscilloscope and lid with a hole were used. Due to the sensitivity of the graphene sample for doping from the air, a closed cabin was constructed for the sample.

A perfectly reusable item for this purpose was the metal box from the probe setup as shown in figure 5.9. Due to the newly drilled holes [33] in this box it was impossible to create a vacuum. Although it was possible to create a flushing chamber. By flushing the chamber with an inert gas i.e. helium or nitrogen, no moisture of particles in the air could dope the graphene samples. By sealing five of the six newly drilled holes the inert gas stayed inside the box. The single non-sealed hole was used to align the box above the hole in the lid. The flushing was done by removing two of the four BNC sockets. One of these BNC holes was used as an outlet and the other one is used as an inlet of the inert gas. One of these holes was connected with a tube and attached to the bottom (side of the lid with a hole) of the box. Due to the lower density of helium, this would screen fewer particles from the scintillator than nitrogen, and thus was the tube used as an outlet. Parts from the holder from the probe setup as shown in figure 5.11 were used to place the graphene sample and measure its transfer curve. Also, adjustments and modifications were made. The graphene samples were smaller than at the time of the probe setup and the measuring technique has changed since then. This resulted in the removal of the four metal pins that were used during the probe setup. Also, a chip carrier was installed in the bottom of the holder to measure the transfer curve of the smaller graphene samples as shown in figure 5.12.
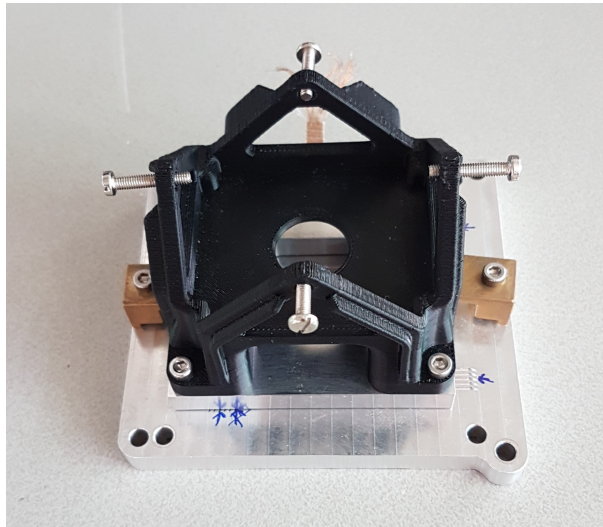
Figure 5.11: The holder from the probe setup. The probe part (with the metal tips as shown in figure 5.2) was removed to prevent screening.

---

[33]The newly drilled holes are on the backside of the metal box. Six small holes were drilled.
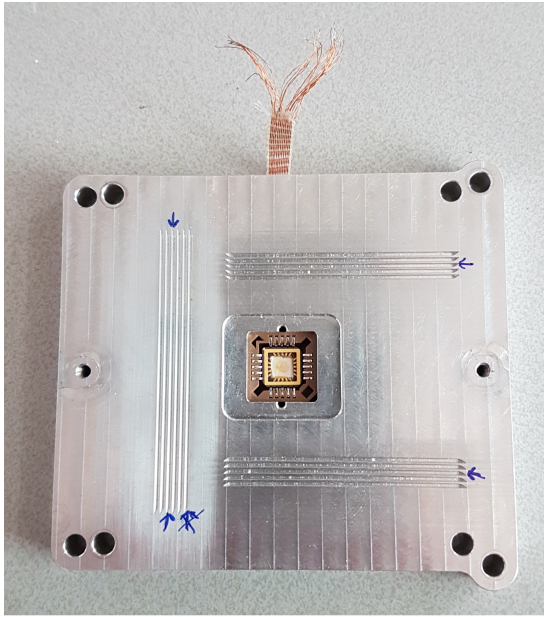
(a) The top of the chip carrier. The graphene sample is placed in the middle of the chip carrier.
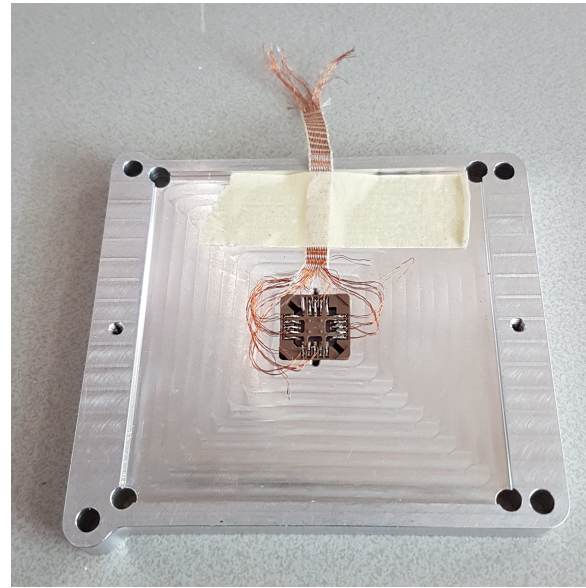
(b) The bottom of the chip carrier. The soldered connections from the chip carrier to the wires are shown as well.

Figure 5.12: A picture of the chip carrier for the graphene sample. In subfigure 5.12a the top of the setup, directly looking into the chip carrier. In subfigure 5.12b the bottom of the chip carrier. Here the solder work and wires are visible.

The radioactive source could be placed in the crown part of the probe setup as shown in figure 5.13
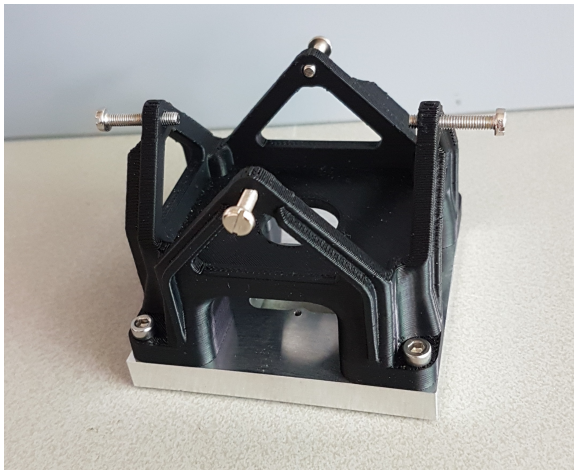
(a) The crown part of the holder from the probe setup.

(b) The crown with the radioactive source in it.

Figure 5.13: In subfigure 5.13a the crown part of the holder from the probe setup. This part will be used to place the source in a stable setup as shown in subfigure 5.13b.

This crucial part of the setup should be tested for optimal results. Thereby, could improvements e.g. alignment and distance (through) air to sample be made easily in this stage of the experiment. One way to check this is by measuring the transmission coefficient. Also screening from the chip carrier should be measured. With a too-low transmission coefficient too much data gets lost which would extend the measurement time to compensate for the screened particles. Besides these tests practicality and usefulness will determined the final design of the box which should be able to detect β particles in graphene.

Results and conclusions about graphene as a particle detector can be found in subsections 6.4.1, 6.4.2, 7.3.1 and 7.3.2, respectively.

6   Results

In this section results for the range experiment (in subsection 6.1), the transfer curve measurements (including annealing and hydrogenation in subsection 6.2) and results about the detection of β particles in different settings (in subsection 6.3). The finding about the range experiment are also included (in subsection 6.1).

6.1   Range experiment

In table 1 the results of the range experiments are given. In this experiment, the range of β particles was measured for several layers of SiO_2 wafers. This was executed in three different runs that were all summed together.

Table 1: The results for the range of Sr-90 β particles and Y-90 β particles with SiO_2 wafers. The read-off error is assumed to be 5% due to the logarithmic scale on the GM counter.

Total thickness SiO_2 wafers (mm)	Number of SiO_2 wafers	Counts per second in GM-counter
0.0	0	$472 \pm 5\%$
0.5 ± 0.15	1	$145 \pm 5\%$
1.0 ± 0.15	2	$95 \pm 5\%$
1.5 ± 0.15	3	$48 \pm 5\%$
2.0 ± 0.15	4	$23 \pm 5\%$
2.5 ± 0.15	5	$7.5 \pm 5\%$
3.0 ± 0.15	6	$5 \pm 5\%$
3.5 ± 0.15	7	0

The plot for the decay of the experiment is shown in figure 6.1.
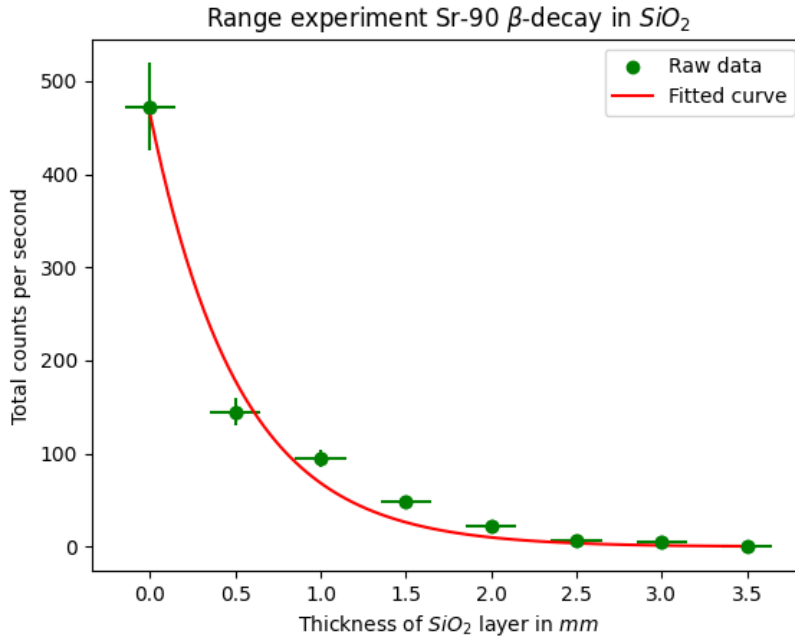
Figure 6.1: The data points from table 1 are summed and plotted with an error of $\pm 0.15\,mm$ for the thickness and an error of $\pm 5\%$ (multiplied by a factor 2 for better visibility) for the GM counter read-off. An exponential fit (ae^{-bx}) was made to the summed data with fitting parameters $a = 464.62 \pm 20.33$ and $b = -1.91 \pm 0.18$ (plots made in Python 3.11).

Besides this experiment, some back-of-the-envelop calculations were executed. These calculations are shown in section B.

β particles from the radioactive source were expected (and hoped) to travel with enough energy to pass at least the graphene, SiO_2 film, and Si wafer. This was tested by using several SiO_2 wafers which had a higher density than the Si wafers. The density was an important factor in the range β particles travels in matter. In figure 6.1 the results are shown. In table 1 the data from all three runs are added together. During run 1 the GM counter seemed to stop and had issues during measurements which may have influenced the count per second. Due to run 2 and 3 the overall data was still useful. Also was the air gap in run 1 between the source and wafers slightly larger than during runs 2 and 3, which may have influenced the data as well. Despite the differences in data, the fit showed an exponential behaviour. A significant fraction of the β particles from the source were able to travel through the wafer material and thus should be able to travel through the graphene devices to the scintillator. There appeared an inconsistent data point at a thickness of $0.5\,mm$ during run 2. Due to this value, the fitted graph differed slightly from the potential fit (compared with the other data points). This value might be caused by a small set-off in the setup where the distance and angle of the GM counter were changed compared to other runs and measurements. Initially, this was not discovered but during the data processing this value stood out and the origin of this deviation was discovered. The fit was still informative and showed the expected exponential decrease but future measurements should be done with more eye on a stable setup. Also, back-of-the-envelope calculations in section B agreed with the theoretical detectability of the β particles.

6.2 Measuring graphene transfer curve

The results of the measurements using two different setups i.e. the probe setup and the chip carrier setup, were given in subsections 6.2.1 and 6.2.2, respectively. With these results the best possible setup for future measurements could be selected.

In subsection 6.2.3 the best of the two setups was used in combination with the hydrogenation box, where graphene samples were exposed to a cold, low-pressure plasma. Two types of plasma were used. First results of the measurements with $Ar - H_2$ plasma and next the results of the measurements with H_2 plasma were executed.

6.2.1 Probe setup

In the probe setup, the resistance of the GFET-S10 chips was determined by measuring V_{12} and I_{SD}, and using Eq. 4.1. $V_{SD} = 20\,mV$ was applied to the graphene device at room temperature. Unfortunately, no current was measured, which would indicate that the resistance would be extremely high. The inconsistent results between the wires and pins during a signal check with a multimeter and the zero source-drain currents suggested problems with the graphene and its connections. A strong microscope showed highly damaged graphene devices as shown in figure 6.2. It appeared that the pins of the probe setup catastrophically scratched the graphene. The 2-probe devices were not used during the measurements and those appeared unharmed under the microscope. Besides the connection between the wiring and contact points was inconsistent after measurements with a multimeter. The same problems were discovered with a later-ordered GFET-S10 chip.
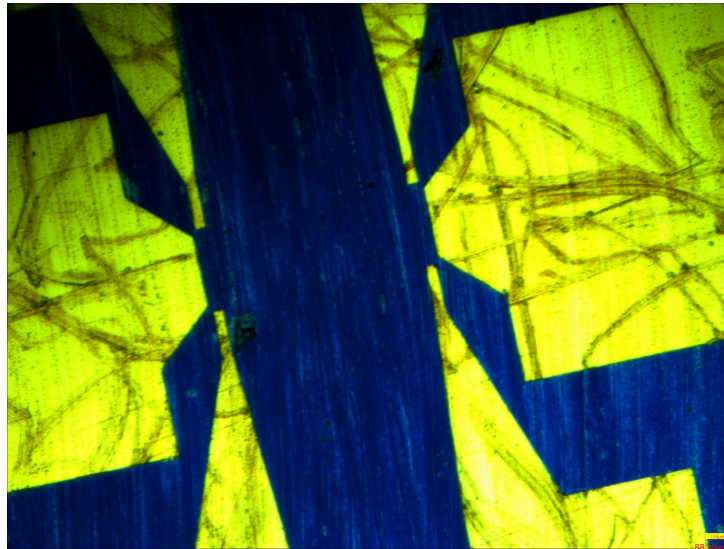
Figure 6.2: Picture from a GFET-S10 device with a 20× magnification. This picture was taken after several measurement attempts with the probe setup.

6.2.2 Chip carrier setup

Three measurements for the transfer curve of graphene samples were executed with the chip carrier setup. First, a measurement with the PMMA layer on top of the graphene sample was executed. During this measurement the V_G was swept between $-60\,V$ and $70\,V$ with a starting and ending point of $0V$ in steps of $\sim 0.1V/s$. In figure 6.3 the resistance as a function of the V_G was plotted. The measurement was executed at room temperature. For increasing V_G the Dirac point was at $V_G = 53.2\,V$ and for decreasing V_G at $V_G = 63.6\,V$. The Dirac point shifted to the right indicates on (p-)doping of the graphene and the difference in increasing and decreasing curve indicates hysteresis behaviour of the sample.
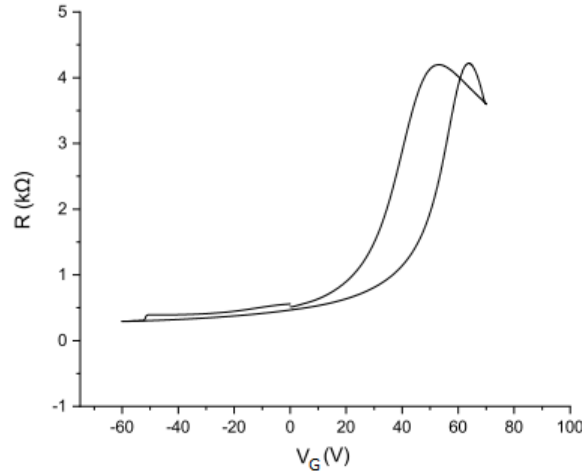
Figure 6.3: The measured transfer curve of a graphene sample with PMMA on top. V_G varied from $-60\,V$ to $70\,V$. The measurement was executed at room temperature. For increasing V_G the Dirac point was at $V_G = 53.2\,V$ and for decreasing V_G at $V_G = 63.6\,V$ (plot made in Origin 2016).

The next measurement was done after carefully removing the PMMA layer. The same graphene sample was measured during the first measurement under the same conditions. During this measurement the V_G was swept between $-20\,V$ and $70\,V$ with a starting and ending point of $0\,V$ in steps of $\sim 0.1V/s$. In figure 6.4 the resistance as a function of the V_G was plotted. The measurement was executed at room temperature. The Dirac point was at a V_G above $70\,V$. No exact Dirac point was found due to a too-low V_G. At $V_G = 70\,V$ a highly fluctuating leakage voltage was measured, which might indicate the graphene was starting to break. The Dirac point shifted even further to the right than in figure 6.3 this sample is expected to be highly (p-)doped. Also the difference in increasing and decreasing curve indicates hysteresis is still present.
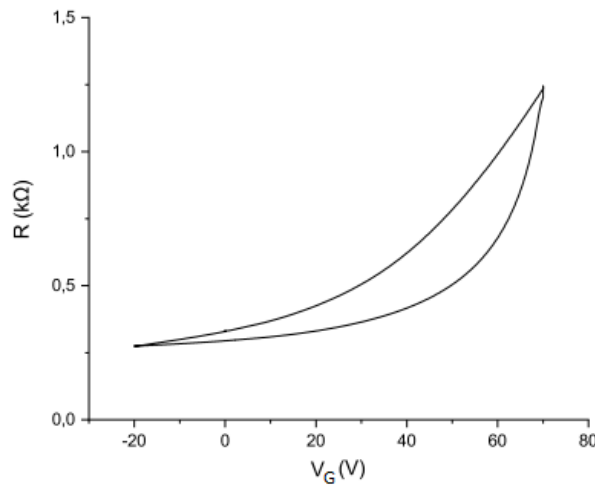
Figure 6.4: The measured transfer curve of a graphene sample with no PMMA on top. V_G varied from $-20\,V$ to $70\,V$. The measurement was executed at room temperature. The Dirac point was above $V_G = 70\,V$ (plot made in Origin 2016).

Next, the same sample was measured after the annealing of the graphene. This was done in two steps ($400\,K$ and $450\,K$). After annealing at $400\,K$ the V_G was swept between $-30V$ and $60V$ with a starting and ending point of $0\,V$ in steps of $\sim 0.1V/s$. In figure 6.5 the resistance as a function of the V_G was plotted. The measurement itself was executed at room temperature. For increasing V_G the Dirac point was at $V_G = 22.2\,V$ and for decreasing V_G at $V_G = 30.0\,V$. The results showed that the graphene was not broken during the previous gate sweep. The Dirac point was still shifted to the right although the (p-)doping was less than in figure 6.3 and 6.4. The hysteresis was still present.
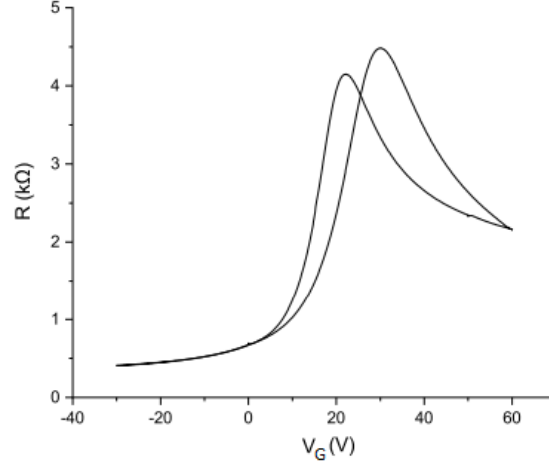
Figure 6.5: The measured transfer curve of a graphene sample annealed at $400\,K$. V_G varied from $-30\,V$ to $60\,V$. The measurement was executed at room temperature. For increasing V_G the Dirac point was at $V_G = 22.2\,V$ and for decreasing V_G at $V_G = 30.0\,V$ (plot made in Origin 2016).

After annealing at $450\,K$, the V_G was swept between $-30\,V$ and $50\,V$ with a starting and ending point of $0\,V$ in steps of $\sim 0.1V/s$. In figure 6.6 the resistance as a function of the V_G was plotted. The measurement itself was executed at room temperature. For increasing V_G the Dirac point was at $V_G = 6.9\,V$ and for decreasing V_G at $V_G = 8.3\,V$. The Dirac point was still shifted to the right compared to the theoretical value but this was the best results obtained and thus the least (p-)doping. The hysteresis was still present, but highly improved compared to previous curves.
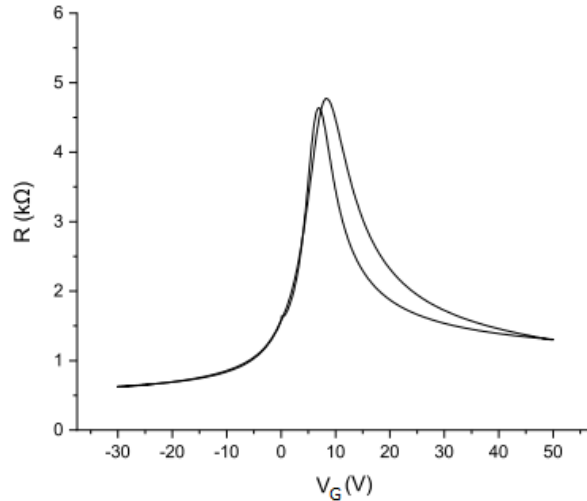
Figure 6.6: The measured transfer curve of a graphene sample annealed at $450\,K$. V_G varied from $-30\,V$ to $50\,V$. The measurement was executed at room temperature. For increasing V_G the Dirac point was at $V_G = 6.9\,V$ and for decreasing V_G at $V_G = 8.3\,V$ (plot made in Origin 2016).

In subsections 6.2.1 and 6.2.2 the results of the probe setup and chip carrier setup were given, respectively. The probe setup gave no results. With the chip carrier setup first the transfer curve of graphene with PMMA on top was measured. Next, the transfer curve without PMMA on top. And after that the graphene sample was annealed at two different temperatures. The chip carrier setup was selected for future measurements due to these results.

6.2.3 Hydrogenation box

With the hydrogenation box a cold, low-pressure plasma was created. Measurements were done similarly as described in subsection 6.2.2 despite being in the hydrogenation box where the vacuum and room temperature were achieved. Note, that forward and backward gate sweeps were executed during all gate sweeps. Although, for clarity purposes, all transfer curves in this subsection were shown with only the part with decreasing V_G, in contrast with figures in subsection 6.2.2. Due to the explosiveness of hydrogen gas in combination with sparks, the setup was first tested with an argon-hydrogen mixture. First, a gate sweep was executed with a sample without PMMA on top. The Dirac point of this transfer curve was found above $50\,V$. Unfortunately, it was not possible to push V_G past the Dirac point due to the leak current. The leak current increased rapidly which indicated that the sample was breaking. The breaking of the graphene was avoided by stopping to push the V_G [34].

Next, the transfer curve for annealing at a temperature of $435\,K$ for $12\,h$ was measured. The annealing took place without a vacuum. This meant that the annealing was executed in air circumstances instead of a vacuum. The transfer curve of this measurement was shown in figure 6.7. The Dirac point was found at $V_G = 39\,V$ which came closer to earlier values with a clear improvement compared to the transfer curve without PMMA and annealing as shown in figure 6.7. This figure differs from figure 6.6. The Dirac point here was shifted further to the right, was lower and the graph was a wider. This meant more (p-)doping, a smaller bandgap and a lower quality of the graphene structure, respectively.
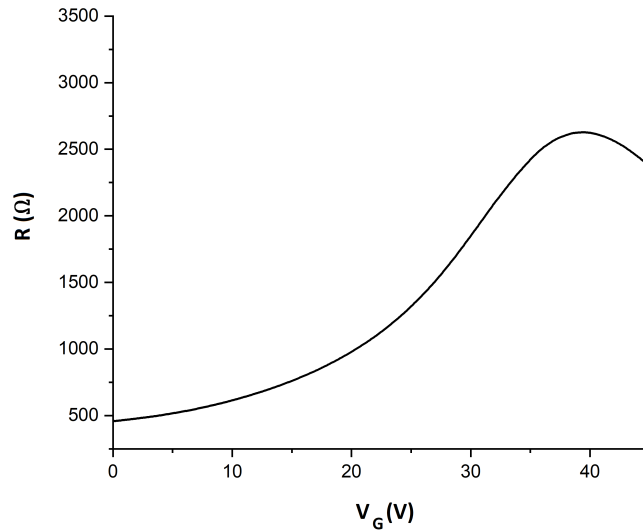
Figure 6.7: The transfer curve of a sample after annealing at $T = 435\,K$. V_G varied from $0\,V$ to $45\,V$, with its Dirac point at $39\,V$ (plot made in Origin 2016).

After annealing, the hydrogenation process with a argon-hydrogen $(Ar - H_2)$ mixture was started. After each hydrogenation process which lasted $30\,s$, a gate sweep was executed. This procedure was executed four times in a row after which six $30\,s$ exposures were executed followed by a small cool-down time and subsequently by a gate sweep. The last plasma exposures were executed for $16\,min$ and $15\,min$, each followed by a gate sweep. In figure 6.8a the gate sweeps were shown and in figure 6.8b the resistance as a function of time for the plasma exposures was shown. All plasma exposures were executed with a pressure of $\sim 1.0\,mbar$. Each hydrogenation (regardless of exposure time) had a similar shape and ended at a higher resistance than started. Note that the first hydrogenation of $30\,s$ was shown in figure 6.8b but no gate sweep after this exposure was shown in figure 6.8a. The Dirac point per curve were: $V_{G,2} = 30\,V$, $V_{G,3}$ was above $40\,V$, $V_{G,4} = 36\,V$, $V_{G,5} = 26\,V$, $V_{G,5} = 29\,V$ and $V_{G,6} = 25\,V$. $V_{G,1}$ is not correctly saved so no sweep for $V_{G,1}$ is in subfigure 6.8a. It was remarkable that most transfer curves in figure 6.8a had a lower Dirac point compared to the annealed sample.

---

[34]During the data analysis, it was remarked that the curve only started at $V_G = 15\,V$. Probably data was lost during the analysis procedure and could not be restored. Fortunately, the part of the transfer curve was not the most interesting. Besides, no hydrogenation or annealing took place which was the main objective of these measurements.
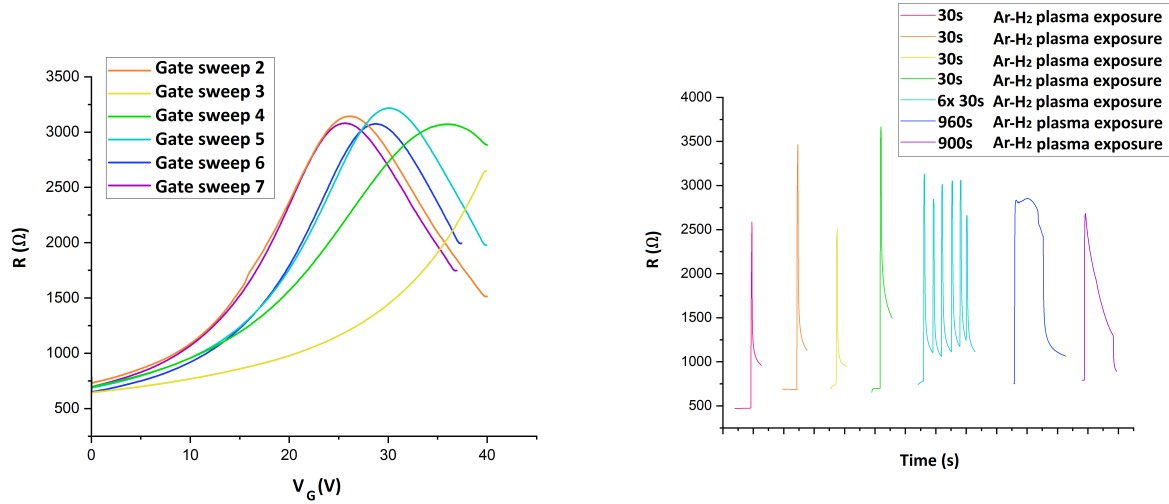
(a) The transfer curves after each exposure to the $Ar - H_2$ mixture are shown. The Dirac point for each curve were: $V_{G,2} = 30\,V$, $V_{G,3}$ was above $40\,V$, $V_{G,4} = 36\,V$, $V_{G,5} = 26\,V$, $V_{G,5} = 29\,V$ and $V_{G,6} = 25\,V$ (plot made in Origin 2016).

(b) The resistance over time, after each hydrogenation phase. All plasma exposures were executed with a pressure of $\sim 1.0\,mbar$ (plot made in Origin 2016).

Figure 6.8: Subfigure 6.8a, the gate sweeps after hydrogenation with the $Ar - H_2$ plasma. Subfigure 6.8b, the resistance curve over time during the plasma exposure.

After a full day of hydrogenating with the $Ar - H_2$ mixture, the sample was annealed in a vacuum at a temperature of $435\,K$ for $12\,h$. The transfer curve was measured after this annealing procedure and this was shown in figure 6.9. The Dirac point was found at $V_G = 24\,V$.
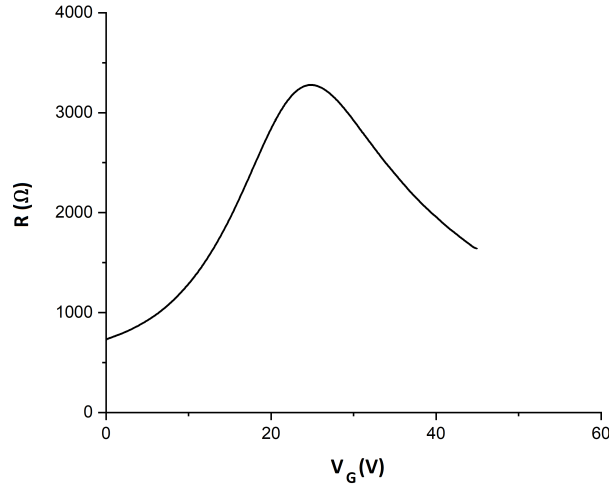
Figure 6.9: The transfer curve of a sample after annealing and after the $Ar - H_2$ plasma exposure at $T = 435\,K$ in a vacuum. V_G varied from $0\,V$ to $45\,V$, with its Dirac point at $24\,V$ (plot made in Origin 2016).

After annealing, the whole procedure of annealing, exposing, and gate sweeping was executed again but the hydrogenation process with only a hydrogen gas was started. For safety, the hydrogenation box was first pumped vacuum to get rid of the air, then flushed with argon to make sure all air was removed from the box and later the hydrogen gas was let in. These plasma exposures were executed for $30\,s$, $30\,s$, $120\,s$, $300\,s$, and $1200\,s$. Each plasma exposure was followed by a small cool-down time and subsequently a gate sweep. In figure 6.10a the gate sweeps were shown and in figure 6.10b the resistance as a function of time for the plasma exposures was shown. All plasma exposures were executed with a pressure of $\sim 1.0\,mbar$. The values for the resistance varied a lot depending on the plasma exposure time. In figure 6.10b only the first three exposures were shown. In figure 6.11, the fourth and fifth plasma

exposures were included for better visibility. Note, the fifth gate sweep is not shown in figure 6.10a. The sweep was not fully completed and the resistance was of the order $\sim 140000\,\Omega$, which started to have characteristics comparable to that of an insulator, which was to be expected with enough doping to open a bandgap. [35]. Regardless of the exposure time the shape of the graphs stayed the same. When the plasma was activated a high peak in resistance was reached. Once the plasma was turned off the resistance dropped. This drop was significant compared to the peak value but a plateau was reached which was higher than the resistance it initially started with.
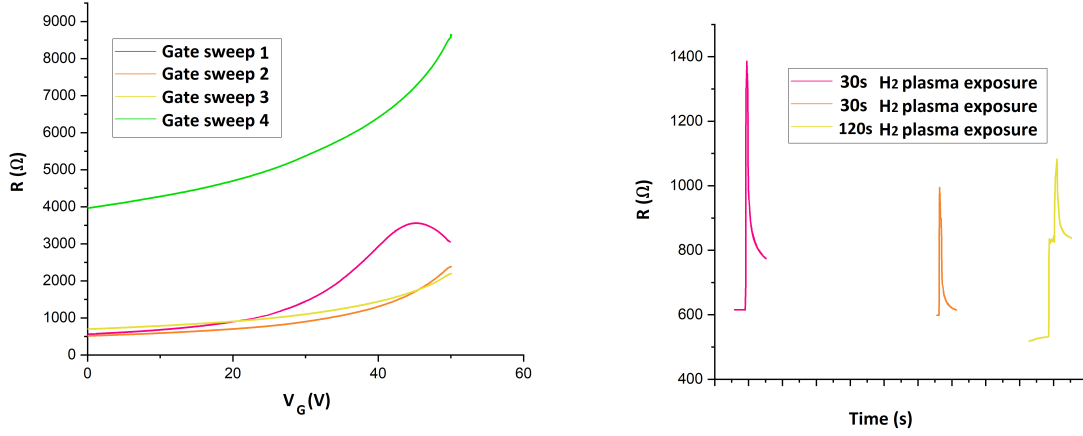
(a) The transfer curves after each exposure to the hydrogen plasma. The Dirac point for each curve was: $V_{G,1} = 45\,V$, $V_{G,2}$ was above $50\,V$, $V_{G,3}$ was above $50\,V$, and $V_{G,4}$ was also above $50\,V$ (plot made in Origin 2016).

(b) The resistance over time, after each hydrogenation phase. All plasma exposures were executed with a pressure of $\sim 1.0\,mbar$ (plot made in Origin 2016).

Figure 6.10: Subfigure 6.10a, the gate sweeps after hydrogenation with the $Ar - H_2$ plasma. Subfigure 6.10b, the resistance curve over time during the plasma exposure.
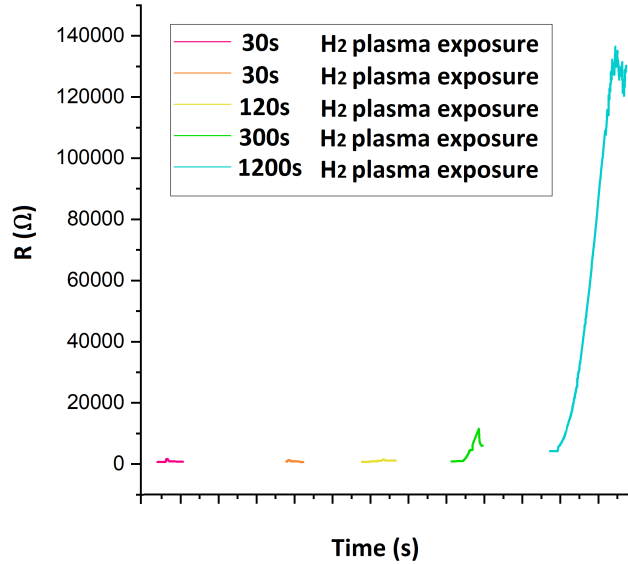
Figure 6.11: The resistance over time, after each hydrogenation phase, is shown, including the fifth exposure. All plasma exposures were executed with a pressure of $\sim 1.0\,mbar$ (plot made in Origin 2016). Note the factor 100 difference between this figure and subfigure 6.10b.

---

[35] Unfortunately, only the first gate sweep passed the Dirac point. The other gate sweeps gave a high leak current which indicated that the sample was breaking. Despite no Dirac point being found for later gate sweeps, the shape of each gate sweep was similar to others.

Next, in figure 6.12 a combination of figures 6.9 and 6.10a were shown. Gate sweep 4 was not shown in this plot. Here a clear comparison between the Dirac point after annealing in a vacuum (6.9) and the gate sweeps after hydrogen plasma exposure (6.10a) was shown. After each gate sweep the Dirac point shifts to a higher gate voltage.
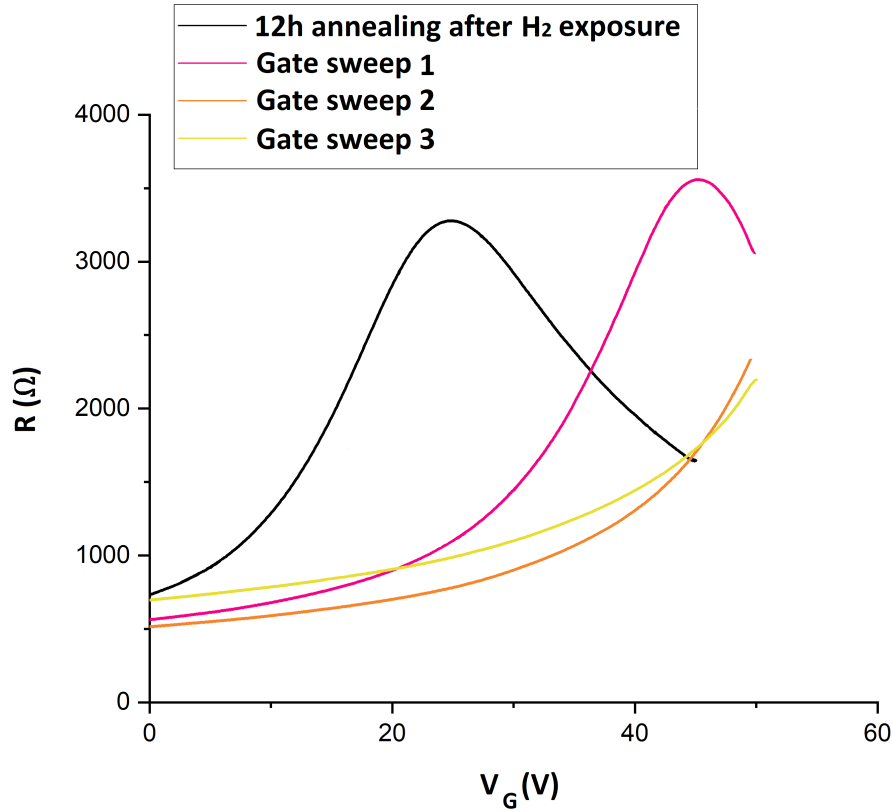
Figure 6.12: Plots for the annealing before the exposure to hydrogen plasma and the gate sweeps after the exposure to hydrogen plasma. Gate sweep 4 was not shown in this plot (plot made in Origin 2016).

In this subsection sample that were hydrogenated with the hydrogenation box we measured. First, a gate sweep of a sample without PMMA on top and without hydrogenating was executed. Next, a gate sweep of an annealed sample was executed. After that the hydrogenation procedure with $Ar - H_2$ was started and alternated with gate sweeps to obtain transfer curves for different exposure times. Later, the sample was annealed, hydrogenated with H_2 and a gate sweep was executed. The hydrogenation and gate sweeps were alternated. Hopeful results were obtained during these experiments which suggested further research into the hydrogenation for an even better understanding and more quantitative results.

Although, there were a few disadvantages of the samples delivered by Graphenea which hindered some potential interesting results. First, the size was not perfectly suitable for available measurement methods which resulted in additional action for samples that were compatible with the measurement methods. This additional cleaving could have been harmful to the samples which would result in a declined quality of the samples. Second, the quality of the samples was questionable. Combined with a gate oxide of only $90\,nm$ samples were easy to break due to a large leak current. A suggestion is to create graphene samples ourselves via exfoliation instead of the CVD used by Graphenea the quality, size, and thickness of the gate oxide could be determined with an eye for our measurement purposes.

6.3 Detection of β particles with photomultiplier

In this subsection, the results of the detection of β particles with a photomultiplier and scintillator are given. Two different setups i.e. were tested in subsections 6.3.1 and 6.3.2, respectively. With these results the best possible setup was selected. Information about the best trigger level and in later experiments signal reduction and transmission coefficients could be determined. This information is valuable for future measurements.

6.3.1 Silicon photomultiplier setup

The V_{BR} as given by the datasheet was checked first. The reverse bias voltage was increased to $V_{BR} = 52.9\,V$. Despite this determination, no β particles were detected by the silicon photomultiplier. At other V_{BR} no β particles were detected either. Problems were found in the scintillator emitted photons that (mainly) a wavelength that did not correspond to the maximum photon detection efficiency of the silicon photomultiplier. Also light might still have entered the box due to all holes in the box. Finally, the connections were not as stable as possible. The silicon photomultiplier setup could have had some potential but a new setup should have been built. The large advantage of this setup could be its compactness where a new setup could bring its potential back to life.

6.3.2 Scintillator setup

In table 2 the results with a trigger level of $-500\,mV$ from the two scintillator setup are shown.

Table 2: The results for the two scintillator setup. Several materials were used to screen the scintillator. The trigger level was set to be $-500\,mV$. The counts achieved over 15 minutes are shown. The error in the counts was assumed to be the square root of the data.

Counts measured in 15 minutes	Background	Source	Source and $SiO2$ wafer	Source and graphite
Run 1	1528 ± 39.1	2449 ± 49.5	2264 ± 47.6	2328 ± 48.2
Run 2	1499 ± 38.7	2283 ± 47.8	2359 ± 48.6	2309 ± 48.1

The signal-to-noise ratio for run 1 was $(S/N)_{run1} = 1.603 \pm 0.052$ and for run 2 it was $(S/N)_{run2} = 1.523 \pm 0.051$. During the measurements of the source, the radioactive source was moved. Another deviation might have been the placement of the graphite under the source. The transmission coefficient for run 1 and run 2 for the SiO_2 wafer and graphite wafer were comparable. A small difference in the transmission coefficient between run 1 and run 2 for the graphite wafer was found. All the transmission coefficients and the total number of counts lie closely together.

When the settings of the NIM and oscilloscope were changed no useful signal was found anymore.

Fortunately, a new lid with pre-made holes gave the possibility to lose the NIM and second scintillator which simplified the setup extremely. The results were improved enormously compared to the two scintillator setup in combination with the NIM. These measurements were done without the source alignment tool, so the source was not in the same position between measurements [36]. For a trigger level of $-500\,mV$ the signal-to-noise ratio [37] was $(S/N)_{run1} = 5.368 \pm 0.165$. In figure 6.13 the data points, errors in the data, and linear fits are shown. The transmission coefficient (T) [38] of SiO_2 was $T_{SiO2} = 0.182 \pm 0.016$ and for graphite $T_{graphite} = 0.201 \pm 0.016$.

---

[36]This could mean that the source might not have been perfectly aligned above the hole, so the lid screened some of the radiation. Future experiments should be carefully aligned with the source alignment tool, so the same placement of the source was guaranteed.

[37]For the signal the source counts after 5 minutes were used and for the noise, the background counts after 5 minutes were used.

[38]The transmission coefficient was calculated as $T = \frac{\text{counts after wafer - counts for the background}}{\text{counts for the source - counts for the background}}$.

And its error was calculated as Error on $T = \sqrt{\left(\frac{\text{error signal - error noise}}{\text{signal - noise}}\right)^2 + \left(\frac{\text{error source - error noise}}{\text{signal - noise}}\right)^2} \cdot T$. The total error was found by adding the situation of the background and source together and take this percentage of the calculated transmission coefficient.
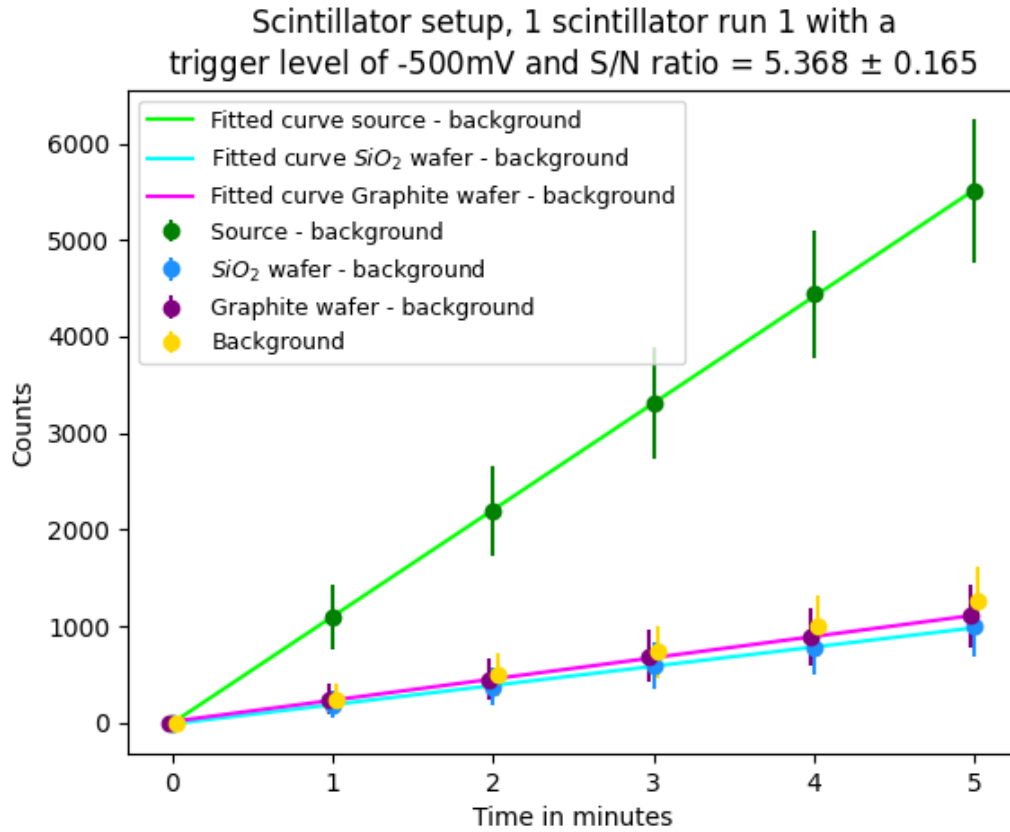
Figure 6.13: Three fitted curves for different situations with the background subtracted, and only the data points for the background for run 1. All the data points have an error of the square root of the data (multiplied by a factor of 10 for better visibility). The fitted curves are fitted to a linear function $(ax + b)$. The fitting parameters for the source - background are $a = 1104.9 \pm 3.9$ and $b = -4.0 \pm 11.8$. The fitting parameters for the SiO_2 wafer - background are $a = 199.0 \pm 3.4$ and $b = -11.9 \pm 10.4$. The fitting parameters for the graphite - background are $a = 220.2 \pm 3.4$ and $b = 12.9 \pm 10.3$ (plots made in Python 3.11).

The results of the second measurement with a trigger level of $-500mV$ are shown in table 3. These measurements were done with the source alignment tool, so the source was in the same position between measurements.

Table 3: The results for the one scintillator setup for run 2 with a lid with a hole. Several materials were used to screen the scintillator. The trigger level was set to be $-500\,mV$. The counts achieved over 5 minutes with data taken each minute are shown. The error in the counts was assumed to be the square root of the data.

Number of passed minutes	Counts for the background	Counts for the source	Counts for the source and $SiO2$ wafer	Counts for the source and graphite
0	0	0	0	0
1	213 ± 14.6	1560 ± 39.5	456 ± 21.4	475 ± 21.8
2	459 ± 21.4	3120 ± 55.9	915 ± 30.2	984 ± 31.4
3	713 ± 26.7	4700 ± 68.6	1343 ± 36.6	1489 ± 38.6
4	948 ± 30.8	6230 ± 78.9	1792 ± 42.3	1975 ± 44.4
5	1197 ± 34.6	7882 ± 88.8	2252 ± 47.5	2462 ± 49.6

The signal-to-noise ratio was $(S/N)_{run2} = 6.585 \pm 0.204$. In figure 6.14 the data points, errors in the data, and linear fits are shown. The transmission coefficient (T) of SiO_2 is $T_{SiO2} = 0.158 \pm 0.013$ and for graphite $T_{graphite} = 0.189 \pm 0.013$.
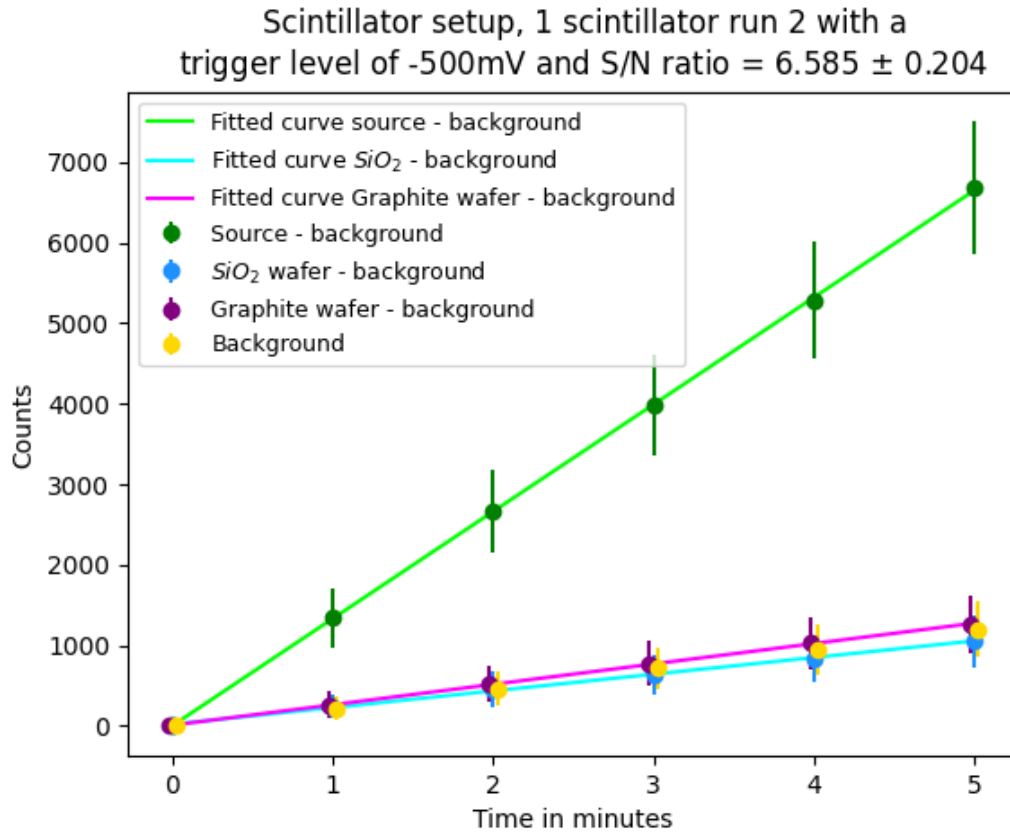
Figure 6.14: Three fitted curves for different situations with the background subtracted, and the data points for the background for run 2 are shown. All the data points have an error of the square root of the data (multiplied by a factor of 10 for better visibility). The fitted curves are fitted to a linear function $(ax + b)$. The fitting parameters for the source - background are $a = 1330.2 \pm 6.5$ and $b = 1.6 \pm 19.6$. The fitting parameters for the SiO_2 wafer - background are $a = 207.2 \pm 4.3$ and $b = 20.0 \pm 12.9$. The fitting parameters for the graphite - background are $a = 253.5 \pm 2.2$ and $b = 8.9 \pm 6.8$. The data points for the background are barely visible due to the overlap with other data points (plots made in Python 3.11).

Typical images of the oscilloscope are shown as screenshots in Appendix C.1.

To determine the best trigger level several different trigger levels were tested and results were obtained. Data for a trigger level at $-500\,mV$ can be found in table 3. The experiments with the least disturbances that were best reproducible were the experiments for the counts for the background and the counts for the source. These were executed again at different trigger levels. The results are shown in tables 4 and 5 for a trigger level of $-300\,mV$ and $-400\,mV$ respectively. A trigger level at $-200\,mV$ was tried as well but no interesting results were obtained.

Table 4: The results for the one scintillator setup with a trigger level at $-300\,mV$. The counts achieved over 5 minutes with data taken each minute are shown. The error in the counts was assumed to be the square root of the data.

Number of passed minutes	Counts for the background	Counts for the source
0	0	0
1	462 ± 21.5	4070 ± 63.8
2	950 ± 30.8	7150 ± 84.6
3	1404 ± 37.5	10040 ± 100.2
4	1897 ± 43.6	13460 ± 116.0
5	2352 ± 48.5	16740 ± 129.4

The signal-to-noise ratio was $(S/N)_{trigger300} = 7.117 \pm 0.157$.

Table 5: The results for the one scintillator setup with a trigger level at $-400\,mV$. The counts achieved over 5 minutes with data taken each minute are shown. The error in the counts was assumed to be the square root of the data.

Number of passed minutes	Counts for the background	Counts for the source
0	0	0
1	330 ± 18.2	3710 ± 60.9
2	656 ± 25.6	7600 ± 87.2
3	987 ± 31.4	11500 ± 107.2
4	1306 ± 36.1	15000 ± 122.5
5	1632 ± 40.4	18433 ± 135.8

The signal-to-noise ratio was $(S/N)_{trigger400} = 11.295 \pm 0.292$.

In this section the best trigger level was found at $-400mV$, which was found by determining the signal-to-noise ratio. This trigger level will be used in future measurements regarding the signal reduction and transmission coefficients.

6.4 Concept setup for graphene as a particle detector

In this subsection results for the graphene sample as a particle detector are shown. In subsection 6.4.1 results about the signal reduction for the setup are given. These results can contribute to a new design for a future detector. In subsection 6.4.2 results about the transmission coefficient are given. These results can also contribute to a new design for a future detector. Where the signal reduction in subsection 6.4.1 mainly focuses on the actual design e.g. distances between sample and source and screening by the chip carrier, the transmission coefficient in subsection 6.4.2 mainly focuses on different substrates and its transmission coefficient.

6.4.1 Signal reduction

Measurements with the box and holder were done to determine how much the signal was reduced by implementing the box and holder. In table 6 the results for a range of measurements are shown.

Table 6: The results from the signal reduction measurements. Multiple situations were tested so the limiting factor for the signal reduction could be found and the reduction factor could be calculated. The counts were measured with a trigger level of $-400\,mV$. The numbers behind the title of each column are used as an abbreviation to indicate what value (after 5 minutes) for which column was used in calculations. The error in the counts was assumed to be the square root of the data.

Number of minutes passed	Counts for the background with box (1)	Counts for the source without box (2)	Counts for the source in box and holder (3)	Counts for the source in holder without box (4)	Counts for the source in crown without box (5)
0	0	0	0	0	0
1	317 ± 17.8	3710 ± 60.9	366 ± 19.1	380 ± 19.5	1505 ± 38.8
2	640 ± 25.3	7600 ± 87.2	710 ± 26.6	781 ± 27.9	2974 ± 54.5
3	949 ± 30.8	11500 ± 107.2	1101 ± 33.2	1172 ± 34.2	4488 ± 67.0
4	1276 ± 35.7	15000 ± 122.5	1512 ± 38.9	1585 ± 39.8	6048 ± 77.8
5	1580 ± 39.7	18433 ± 135.8	1889 ± 43.5	1982 ± 44.5	7605 ± 87.2

The signal-to-noise ratio was $(S/N) = 1.196 \pm 0.041$. Here the ratio between (1), background with box, and (3), source in box in holder, was taken. So, the holder was included in the value for the signal as well. The measured counts for the background were comparable with other count measurements for the background.

The counts for (3), source with box in holder, and (4), source in holder without box, were compared by determining their ratio. With this ratio, the signal reduction due to the box could be determined. This ratio after subtracting the background gave the following value. $f_{box} = \frac{(4)-(1)}{(3)-(1)} = \frac{1982-1580}{1889-1580} = 1.301 \pm 0.444$.

The same was done for (4), source in holder without box, and (5), source in crown without box, which were compared by determining their ratio. With this ratio, the signal reduction due to the chip carrier could be determined. This ratio after subtracting the background gave the following value $f_{chipcarrier} = \frac{(5)-(1)}{(4)-(1)} = \frac{7605-1580}{1982-1580} = 14.988 \pm 3.155$.

The counts for (2), source without box, and (5), source in crown without box, were compared by determining their ratio. With this ratio the signal reduction due to the long distance (through the air) could be determined. This ratio after subtracting the background gave the following value $f_{air} = \frac{(2)-(1)}{(5)-(1)} = \frac{18433-1580}{7605-1580} = 2.797 \pm 0.066$.

Finally, the counts for (2), source without box, and (4), source in crown without box, were compared by determining their ratio. With this ratio the signal reduction due to the chip carrier and longer distance (through the air) could be determined. This ratio after subtracting the background gave the following value $f_{air+chipcarrier} = \frac{(2)-(1)}{(4)-(1)} = \frac{18433-1580}{1982-1580} = 41.923 \pm 8.792$. All these fractions are again shown in table 7.

Table 7: Factors of possible improvements setup for graphene as a particle detector. Multiple improvements could be applied. The total improvement factor in that case is the product of the individual factors (as shown in the lowest row).

Improvement factor	Value
f_{box}	1.30 ± 1.1
$f_{chipcarrier}$	15.00 ± 3.9
f_{air}	2.80 ± 1.7
$f_{air+chipcarrier} = f_{air} + f_{chipcarrier}$	41.92 ± 6.5

6.4.2   Transmission coefficient

Measurements for the transmission coefficient and the influence of graphite were done to determine the expected transmission of the β particles through the SiO_2 wafer (and graphite). In table 8 the results for the transmission measurements are shown.

Table 8: The results from the transmission measurements. The background and source itself were (again) measured to ensure measurements were done with correct values. In the last two columns, the counts with the source on top of wafers are shown. First, a clean wafer made of SiO_2 was tested, and later the same type of SiO_2 wafer with graphite on top. The counts were measured with a trigger level of $-400\,mV$. The numbers behind the title of each column are used as an abbreviation to indicate what value (after 5 minutes) for which column is used in calculations. The value 1570 was an estimated value due to a missed read-off from the oscillator. The error in the counts was assumed to be the square root of the data.

Number of minutes passed	Counts for the background	Counts for the source in crown	Counts for the source in crown and SiO_2 wafer	Counts for the source in crown and SiO_2 wafer with graphite
0	0	0	0	0
1	278 ± 16.7	1042 ± 32.3	489 ± 22.1	481 ± 21.9
2	608 ± 24.7	2066 ± 45.5	1038 ± 32.2	1018 ± 31.9
3	877 ± 29.6	3091 ± 55.6	1570 ± 39.6	1569 ± 39.6
4	1189 ± 34.5	4070 ± 63.8	2038 ± 45.1	2104 ± 45.9
5	1511 ± 38.9	5102 ± 71.4	2661 ± 51.6	2635 ± 51.3

The transmission coefficient for the SiO_2 wafer was $T_{SiO_2} = 0.320 \pm 0.027$. The transmission coefficient for the SiO_2 wafer with graphite on it was $T_{graphite} = 0.313 \pm 0.027$.

Conclusions about the signal reduction can be found in subsection 7.3.1 and conclusions about the transmission coefficient can be found in subsection 7.3.2. With these results a design was created which can be found in section 8. In section 8 all results discovered in these subsections were taken into account for the best possible design for detecting β particles.

7   Conclusion and discussion

In this section conclusions and possible future improvements of results are given. Most of these conclusions contributed to the final product of this thesis which was the design and creation of a box were graphene measurements could be done under the best circumstances according to these results. In subsection 6.2 the conclusions of the two methods i.e. probe setup and chip carrier setup are given. Also an extensive conclusion and finding for the hydrogenation are given in this subsection. The following subsection, subsection 7.2, gives conclusions about the silicon photomultiplier setup and the scintillator setup. This leads to the last subsection, subsection 7.3, where conclusions about the signal reduction and transmission coefficients are given.

7.1   Measuring graphene transfer curve

In this subsection the results about the probe setup and chip carrier setup are evaluated. This determines the setup which will be used in future measurements. With the best setup, samples were hydrogenated. The results of the hydrogenation are evaluated in subsection 7.1.3.

7.1.1   Probe setup

The probe setup did not give results. It was concluded that the probe setup was not the best option for measuring a stable transfer curve of a GFET-S10 chip. An alternative setup was proposed namely the chip carrier setup.

7.1.2   Chip carrier setup

The results of the chip carrier setup seemed promising for measuring a stable transfer curve. With PMMA on top of the graphene sample results seemed comparable with the datasheet from Graphenea. Previously doping from the air caused contaminations on the sample. The PMMA prevented molecules from the air to attach on the graphene surface and thus protected the graphene from doping. A possible explanation for the hysteresis effect could be given by trapped and released charge carriers at the interface of the graphene and silicon oxide layer. Due to a minimal amount of freely moving electrons in graphene, the effective electron concentration is low because most electrons are bound. The then p-doped graphene shifted the Dirac peak more to the positive V_G when V_G was lowered back to zero. After annealing the quality of the graphene seemed to be enhanced compared to previous results. The annealing removed impurities from the graphene surface. These impurities caused p-doping and shifted the Dirac peak to a positive V_G. The theoretical transfer curve for graphene should have had its Dirac peak around $V_G = 0\,V$. Graphenea measured the Dirac peak around $V_G = 28\,V$, which was significantly higher than the measurements done for this thesis. So the annealing procedure approached better (theoretical) results. At higher annealing temperatures the quality of the graphene improved. This was seen in the transfer curve, the width of the Dirac peak became smaller and the Dirac peak was shifted close to the theoretical $V_G = 0V$ and was lower than the V_G measured by Graphenea. The hysteresis also appeared to be less present than in previous measurements. The impurities enhanced the hysteretic behaviour before but the annealing process improved the quality of graphene so the hysteretic behaviour was reduced. At higher temperatures and longer annealing times, the sample could improve further, although at too high temperatures the contacts of the graphene devices or graphene itself might be damaged.

7.1.3   Hydrogenation box

The findings from subsection 7.1.2 about hysteresis remained valid in this subsection. The amount of hysteresis was comparable to before, where the forward sweep had a lower Dirac point compared to the backward sweep. This phenomenon decreased after removing the PMMA layer and annealing the samples (just as before).

First, the PMMA from a new sample was removed and a gate sweep gave a value of the Dirac point of above $50\,V$. This was not a big problem because the main objective was to hydrogenate samples and not discover the limits of the samples as this was already checked before.

After 12 hours of annealing at $435\,K$ the Dirac point was worse compared to previous results. One reason for this quality decrease was the age of the samples. Despite the carefully stored samples, con-

tamination took place over time. Combined with annealing in the air, the quality declined. A possible solution would have been annealing at higher temperatures and most importantly anneal in a vacuum.

After several $Ar - H_2$ exposures no pattern in the influence of the Dirac point or resistance due to pressure fluctuations were discovered. Future improvements could be made by using an electronic pressure control mechanism. After the hydrogenation procedure, the Dirac point changed values. It was expected that hydrogenating the sample would increase the doping in the sample and this pushed the Dirac point to a higher V_G. The plasma of $Ar - H_2$ mixture contained hydrogen ions and argon ions. The hydrogen ions were expected to hydrogenate/dope the graphene while the argon ions recombined into argon gas and were sucked away by the vacuum pump. Due to the low pressure, the inlet of the $Ar - H_2$ mixture might have caused the argon ions to clean the sample by scattering contamination off the graphene. This might have explained the lower Dirac point.

The peak value in resistance during hydrogenation was explained by the forced argon ions on the sample. As long as the plasma was on, charged ions were pushed against the graphene which resulted in higher resistance. Once the plasma was turned off, this pushing force fell away and the resistance was no longer forced to a high value. Only the actual hydrogenation remained on the graphene. To confirm the influence of argon and verify that the sample was doped by hydrogen a new measurement was executed with only hydrogen gas.

The value which agreed most with theory was after annealing for 12 hours in a vacuum with a value for the Dirac point of $V_G = 24\,V$. This shows the importance of annealing in vacuum.

From the hydrogenation with a hydrogen plasma, it could be deduced that the Dirac point shifted to a higher V_G, and thus the sample became more doped. The longer the exposure time the more doped the sample. With longer exposure times a band gap started to open and the graphene started to behave as an insulator.

Cleaning effects present with the $Ar - H_2$ plasma were absent with only the hydrogen plasma. Argon thus appeared to have scattered contamination of the graphene during previous measurements and acted as a cleaning method. It was concluded that a plasma consisting of hydrogen was the best option for hydrogenating the graphene sample. When the transfer curves were compared to the samples that were exposed to the $Ar - H_2$ plasma an expected pattern where doping increased the V_G for the Dirac point was found.

After the results obtained future researchers continued with the hydrogenation experiment. In figure 7.1 the transfer curve of a graphene sample is shown. In this experiment the sample started in an annealed state and was exposed to the hydrogen plasma for a minute each exposure round. The width of the transfer curve seemed to increase after more exposures. The Dirac point was kept around $0V$ but the resistance of the Dirac point increased to a maximum of $\sim 3.5k\Omega$.
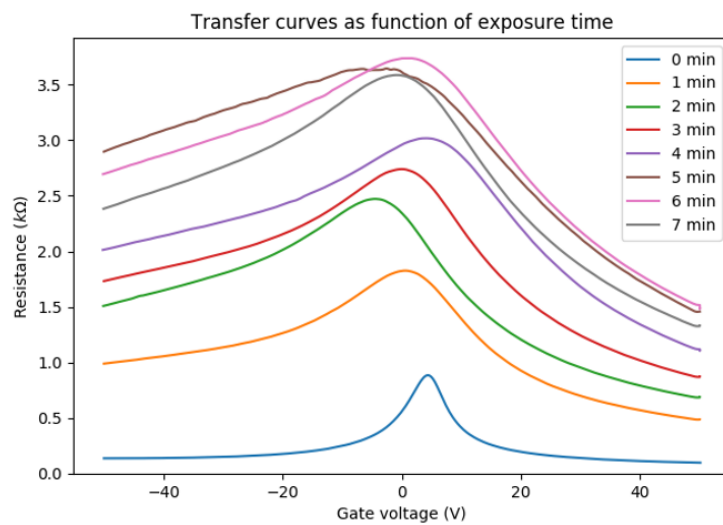
Figure 7.1: Transfer curves of hydrogenation in a future measurement. This measurement was started with an annealed sample and after that exposed for 1 minute each exposure round. In the label the cumulative exposure time is given.

7.2   Detection of β particles with photomultiplier

In this subsection the results about the silicon photomultiplier setup and the scintillator setup are evaluated. On the basis of these conclusions the next subsection, where the signal reduction and transmission coefficients were determined, was executed.

7.2.1   Silicon photomultiplier setup

The initial setup with a scintillator and silicon photomultiplier gave no results. The problems with the silicon photomultiplier were avoided by using a different kind of scintillator and photomultiplier in a different setup.

7.2.2   Scintillator setup

The signal-to-noise ratio in run 1 and run 2 gave poor results. This poor ratio was attributed to the aluminium lid on top of the scintillator. This was important to prevent light saturation of the scintillator.

In the results the positive effect of the source alignment tool is visible. This suggest that future measurements should have the best possible and stable alignment for reproducible results.

Small differences in transmission coefficients between run 1 and 2 were found. This might have been caused because of poor-quality wafers. The SiO_2 wafer were old (probably contaminated) wafers from the HFML. The graphite wafers consisted of a SiO_2 wafer with graphite on top. The thickness of the graphite layers was unknown and varied from location to location within each wafer. It might have been possible that a relatively thin layer of graphite screened the beam in run 1 and a relatively thick layer screened the beam in run 2. The linear fits meant that the detection of particles was constant over time. This regular counts over time were to be expected since no changes were executed during the measurements and the background and source sent out particles regularly. These results gave confidence that it was possible to recreate measurements that were comparable to previous measurements. The best trigger level on the oscilloscope was found at $-400\,mV$ with a signal-to-noise ratio of $(S/N)_{trigger400} = 11.295 \pm 0.292$.

## 7.3   Concept setup for graphene as a particle detector

In this subsection conclusion about the signal reduction and transmission coefficients are given. These results are directly used in the new design for a box where β particles in combination with graphene can be detected.

7.3.1   Signal reduction

The signal-to-noise ratio $(S/N) = 1.20 \pm 1.1$ for the background and box compared to the source and box, which was about a factor of 10 lower than with previous measurements. This deviation was described by the addition of the box and holder, which deteriorated the signal-to-noise ratio. Additional measurements were done to discover other limiting factors due to this low signal-to-noise ratio. First, it was remarked that the background was approximately the same as without a box. The background during this measurement was taken for either measurement with or without a box on top of the scintillator. To discover the factors accountable for this signal-reduction the influence of the box was determined first. With a ratio of $f_{box} = 1.30 \pm 1.1$, it could be concluded that the box reduced the signal by a small neglectable factor. Most of the background noise was already filtered by conducting experiments within a building. Also was the distance the β particles traveled a signal-reducing factor. The further the β particles traveled the more this reduces the signal as would be expected from Eq. 3.16. Another factor that was investigated was the $f_{chipcarrier}$. The chip carrier setup was the best way of measuring the transfer curve of graphene. Although a lot of screening occurred as the signal was reduced by a factor of $f_{chipcarrier} = 15.00 \pm 3.9$. This was a combination of a part of metal from the actual chip carrier and a part of plastic for the chip carrier holder. By drilling a hole into the chip carrier and the chip carrier holder as shown in figure 7.2 no material screened the radiation anymore and improved the signal which was now only limited to the travel distance through the air (and the tape and aluminium foil to prevent light saturation and SiO_2 from the wafer).
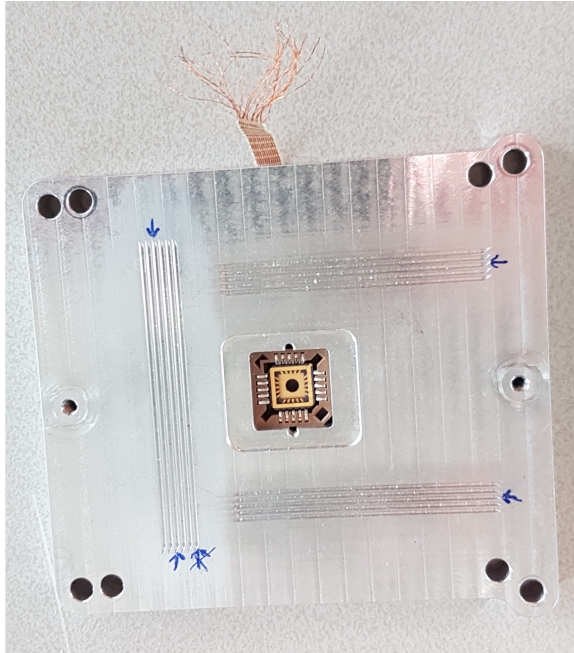
(a) The top of the chip carrier with a hole. The graphene sample is placed in the middle of the chip carrier right over the hole.
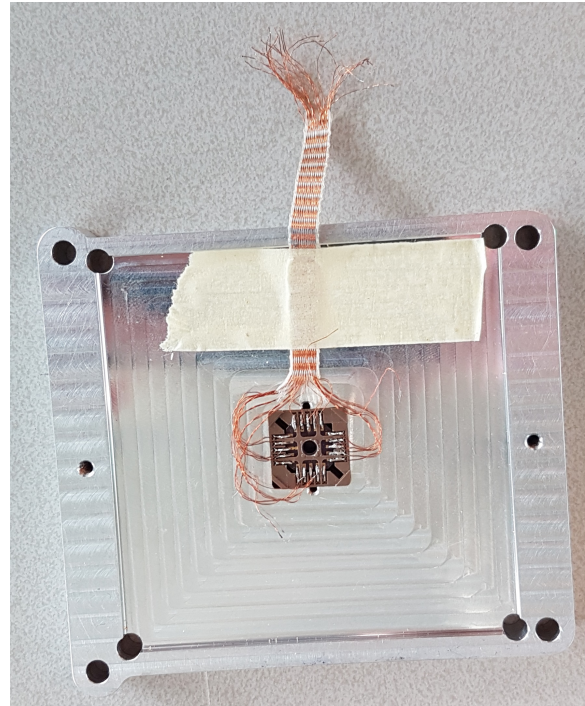
(b) The bottom of the chip carrier with a hole. The soldered connections from the chip carrier with a hole to wires are shown as well.

Figure 7.2: A picture of the chip carrier for the graphene sample with a hole. Subfigure 7.2a, the top of the setup, directly looking into the chip carrier. Subfigure 7.2b, the bottom of the chip carrier. Here the solder work and wires are visible.

The factor for the signal reduction for the traveled distance (through the air) was determined as well. The signal was reduced by the ratio $f_{air} = 2.80$. By performing measurements in a vacuum this factor should (nearly) vanish. The use of an inert gas would not improve the signal for an unchanged travel distance. The inert gas only protected the graphene sample from contamination from the air which would dope the graphene. To limit this reducing factor the distance between the source, sample and scintillator should be as small as possible. The crown that was used was higher than necessary. Because the pins from the probe were removed, the travel distance could be reduced. A simple solution that would result in less travel distance for the β particles was to lower the crown. A newly 3D printed crown could easily be accomplished and the alignment challenges solved. Although perfect alignment remains difficult, the newly printed crown made it possible to reproduce the same alignment conditions over and over again. The product of the signal reduction factors $f_{chipcarrier}$ and f_{air} gave the factor by which the current signal could be increased. All signal reduction factors are shown in table 7. A total factor of $f_{air+chipcarrier} = f_{chipcarrier} + f_{air} = 41.92 \pm 6.5$ was to be gained. This factor was not reached in practice because of two main reasons. By lowering the crown the travel distance was reduced but this distance could never become zero (measured from the lid) because space for the graphene sample was necessary. By removing the bottom of the chip carrier and chip carrier holder the signal was improved but this was replaced by a wafer of SiO_2 with graphene on top. The screening from the SiO_2 wafer was nonetheless smaller than from the chip carrier and chip carrier holder together, but there was still a material present to screen the β particles. The factor in practice was not measured due to the fabrication time of the new, improved setup.

7.3.2   Transmission coefficient

The results for the transmission coefficient for a SiO_2 wafer and a SiO_2 wafer with graphite on top were, $T_{SiO_2} = 0.32 \pm 0.04$ and $T_{graphite} = 0.31 \pm 0.03$, respectively. These numbers were quite similar and well within the error margin of each other. The absolute difference between the counts was 26 counts. This difference might be caused by a small timing error at the start or end of each measurement. Due to this minimum difference, it was concluded that graphite barely influenced the transmission coefficient of β particles. It was not known how thick the graphite layer was exactly but a minimum of several 100 atomic layers was assured. The thickness of graphene is just one atomic layer and thus should exceed the transmission coefficient for graphite, $T_{graphite}$. From the transmission coefficient, T_{SiO_2}, (and comparing this to the transmission coefficient $T_{graphite}$) it was concluded that most of the β particles were stopped by the SiO_2 wafer and not the graphite. This also confirms the previous statement that graphene barely influenced the transmission coefficient for β particles. With this expected high transmission coefficient of graphene, the design for a cosmic neutrino telescope could consist of multiple layers of graphene. Assuming tritium on graphene had a minimal influence on the transmission coefficient of the graphene layers, a large surface area of graphene could be created in a relatively small space. By stacking these tritinated graphene layers carefully on top of each other, more $C\nu B$ particles would be captured than using a single layer of tritinated graphene. This stacking would not reduce the signal significantly.

8 Outlook

In subsection 5.4 a concept version for a box with graphene as a particle detector. Combined with the conclusions found in this thesis, as described in section 7, a new design for a box with graphene as a particle detector was built. Expertise from the technical staff was taken into account as well.

A few changes compared to the concept version of subsection 5.4 were made. The initial idea of reusing the previous box was, after discussions with the technician, not favorable due to all the holes and connections points that were useless for the purposes of this box. A new similar box was ordered where only necessary holes and connection were mounted.

The scintillator setup appeared a reliable way to detect particles as extensively explored in subsection 6.3.2. With the knowledge from subsection 6.4, distance and screening appeared to influence the particle detectability significantly. While the scintillator setup allowed for the distance between the graphene sample and the scintillator to be reduced, particles still required to travel a distance in the order of *cm*. Additional to the distance issue, the size of the scintillator setup was too large to be put inside a box. Another challenge was the alignment of the entire setup which needed to be as stable as possible for the best possible results. All these disadvantages were taken into consideration and resulted in the reintroduction of the silicon photomultiplier. In subsection 6.3.1 this appeared a bad method to detect particles. Although it was thought to be a bad method, the size advantage, and the complete alignment challenge would be easy to solve with this new setup. This could overcome the disadvantages of subsection 6.3.1. Also, the distance could be minimal with this silicon photomultiplier inside the box. Screening and signal reduction due to air was minimized. These advantages outweigh the disadvantages from subsection 6.3.1.

It was even possible to fit in a circuit board with stable wiring, which was doubtful during the measurements with the silicon photomultiplier setup. This circuit board combined with a newly printed crown improved the alignment of the setup further. The circuit board had the same option to change the chip carrier with graphene as the probe setup. With this method, the graphene samples were well protected and could still be stored inside the desiccator.

With the addition of a bubbler, the possibility of flushing with an inert gas remained possible. With a valve the flushing could be stopped and started. This box is not vacuum-tight but small modifications could make this possible as well.

Another large advantage of this setup was the modulated structure. Each part was easily interchangeable into new parts. If for example, the scintillator emitted photons with a different wavelength than the silicon photomultiplier was able to detect, this part could be interchanged for a new part. Other scintillators or photomultipliers could be placed inside the box without the need for a completely new box.

The inside of the new box was shown in figure 8.1.

Figure 8.1: In this figure, the inside of the box for graphene as a particle detector is shown. On top of the inside of the box, the radioactive source is placed. Beneath that the graphene sample in a chip carrier is located. On the front connections stick out for the connection with the Fischer 24 connector. In the yellow part of the box, the scintillator is located beneath that the silicon photomultiplier. On the right, the lid with cables (connected to the Fischer 24 connector) is shown. These cables could be connected to the contact connected to the chip carrier.

More details about the inside of the yellow part from figure 8.1 and the chip carrier could be found in figure 8.2.
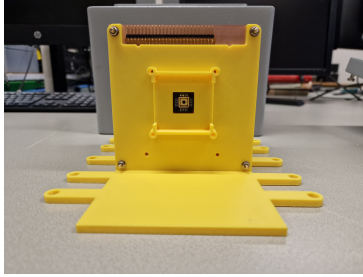
(a) A top view of the chip carrier. The chip carrier could be replaced with a chip carrier with graphene in it as shown in figure 5.4
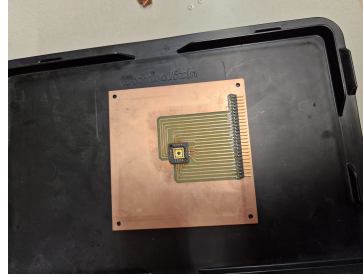
(b) The stable connections via a circuit board. With at the bottom of this picture, the tips for connections with the Fischer 24 connector.
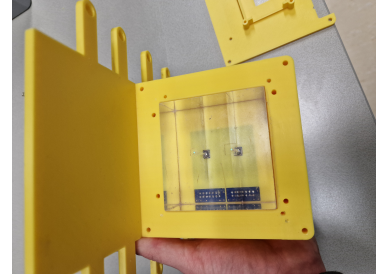
(c) A look through the scintillator. At the bottom, through the scintillator the silicon photomultiplier is visible.

Figure 8.2: Detailed insight into the graphene measurement box.

The outside of the graphene measurement box was shown in figure 8.3.

Figure 8.3: The Fischer 24 connector in the middle of the box. On the left top and right bottom, the inlet and outlet for the helium gas, respectively. The inlet has a valve that could stop the inflow of helium gas. The outlet is connected to the bubbler. With this implementation, it is impossible for gas to enter the box via the outlet. The bubbler is filled with glycerol due to the advantages of its high viscosity.

9   References

[1] Apponi, A. *et al.* Heisenberg's uncertainty principle in the PTOLEMY project: a theory update. *arXiv preprint arXiv:2203.11228* (2022).

[2] Baracchini, E. *et al.* PTOLEMY: A proposal for thermal relic detection of massive neutrinos and directional detection of MeV dark matter. *arXiv preprint arXiv:1808.01892* (2018).

[3] Apponi, A. *et al.* Implementation and optimization of the PTOLEMY transverse drift electromagnetic filter. *Journal of Instrumentation* **17**, P05021 (2022).

[4] Weinberg, S. Universal neutrino degeneracy. *Physical Review* **128**, 1457 (1962).

[5] Sokolenko, A. Detecting relic neutrinos (2020). URL https://indico.cern.ch/event/912388/attachments/2034862/3406569/CnuB.pdf.

[6] Betti, M. *et al.* Neutrino physics with the PTOLEMY project: active neutrino properties and the light sterile case. *Journal of Cosmology and Astroparticle Physics* **2019**, 047 (2019).

[7] The KATRIN collaboration. Direct neutrino-mass measurement with sub-electronvolt sensitivity. *Nature Physics* **18**, 160–166 (2022).

[8] Wallace, P. R. The band theory of graphite. *Physical review* **71**, 622 (1947).

[9] Slonczewski, J. & Weiss, P. Band structure of graphite. *Physical Review* **109**, 272 (1958).

[10] Semenoff, G. W. Condensed-matter simulation of a three-dimensional anomaly. *Physical Review Letters* **53**, 2449 (1984).

[11] Haldane, F. D. M. Model for a quantum Hall effect without Landau levels: Condensed-matter realization of the parity anomaly. *Physical review letters* **61**, 2015 (1988).

[12] Novoselov, K. S. *et al.* Electric field effect in atomically thin carbon films. *science* **306**, 666–669 (2004).

[13] Novoselov, K. S. *et al.* Two-dimensional atomic crystals. *Proceedings of the National Academy of Sciences* **102**, 10451–10453 (2005).

[14] Novoselov, K. S. *et al.* Two-dimensional gas of massless Dirac fermions in graphene. *nature* **438**, 197–200 (2005).

[15] Sun, J. Graphene Science and Technology (2018). URL https://www.edx.org/course/graphene-science-and-technology.

[16] Partoens, B. & Peeters, F. From graphene to graphite: Electronic structure around the K point. *Physical Review B* **74**, 075404 (2006).

[17] Morozov, S. *et al.* Two-dimensional electron and hole gases at the surface of graphite. *Physical Review B* **72**, 201401 (2005).

[18] Landau L.D., L. E. *Course of theoretical physics Vol. 5. Statistical physics, part 1* (Pergamon, 1980), 3ed. edn.

[19] Venables, J. & Spiller, G. Nucleation and growth of thin films. In *Surface Mobilities on Solid Materials*, 341–404 (Springer, 1983).

[20] Evans, J., Thiel, P. & Bartelt, M. C. Morphological evolution during epitaxial thin film growth: Formation of 2D islands and 3D mounds. *Surface science reports* **61**, 1–128 (2006).

[21] Stankovich, S. *et al.* Graphene-based composite materials. *nature* **442**, 282–286 (2006).

[22] Meyer, J. C. *et al.* The structure of suspended graphene sheets. *Nature* **446**, 60–63 (2007).

[23] Nelson, D., Piran, T. & Weinberg, S. *Statistical mechanics of membranes and surfaces* (World Scientific, 2004).

[24] Geim, A. K. & Novoselov, K. S. The rise of graphene. In *Nanoscience and technology: a collection of reviews from nature journals*, 11–19 (World Scientific, 2010).

[25] Blake, P. *et al.* Making graphene visible. *Applied physics letters* **91**, 063124 (2007).

[26] Fuente, J. d. L. CVD graphene - creating graphene via chemical vapour deposition (2010). URL <https://www.graphenea.com/pages/cvd-graphene#.YnpK9ehBy5c>.

[27] Dedicated graphene foundry (2010). URL <https://www.graphenea.com/>.

[28] Katsnelson, M. I. *The physics of graphene* (Cambridge University Press, 2020), second edn.

[29] Wikipedia. Shapes of hybrid orbitals (2020). URL <https://en.wikipedia.org/wiki/File:Shapes_of_hybrid_orbitals.svg>.

[30] Glad, X. Synthèse et étude de la formation de pyramides et cônes de graphite par gravure en plasma radiofréquence argon/hydrogène (2014). URL <http://docnum.univ-lorraine.fr/public/DDOC_T_2014_0127_GLAD.pdf>.

[31] Newson, R. W. *Dynamics of Carriers and Photoinjected Currents in Carbon Nanotubes and Graphene* (University of Toronto, 2010).

[32] Novoselov, K. S. *et al.* Room-temperature quantum Hall effect in graphene. *Science* **315**, 1379–1379 (2007).

[33] Luk'yanchuk, I. A. & Bratkovsky, A. M. Lattice-induced double-valley degeneracy lifting in graphene by a magnetic field. *Physical review letters* **100**, 176404 (2008).

[34] Zheng, Y. & Ando, T. Hall conductivity of a two-dimensional graphite system. *Physical Review B* **65**, 245420 (2002).

[35] Gusynin, V. & Sharapov, S. Unconventional integer quantum Hall effect in graphene. *Physical review letters* **95**, 146801 (2005).

[36] Peres, N., Guinea, F. & Neto, A. C. Electronic properties of disordered two-dimensional carbon. *Physical Review B* **73**, 125411 (2006).

[37] Morozov, S. V. *et al.* Strong suppression of weak localization in graphene. *Physical review letters* **97**, 016801 (2006).

[38] McCann, E. *et al.* Weak-localization magnetoresistance and valley symmetry in graphene. *Physical review letters* **97**, 146805 (2006).

[39] Giesbers, A. J. M. *Physics in graphene & quantum rings: from mesoscopic device fabrication to measurement in high magnetic fields* ([Sl: sn], 2010).

[40] van Elferen, H. *Magneto-transport properties of (multilayer) graphene: the lowest Landau level in high magnetic fields* ([Sl: sn], 2013).

[41] Whitener Jr, K. E. Hydrogenated graphene: A user's guide. *Journal of Vacuum Science & Technology A: Vacuum, Surfaces, and Films* **36**, 05G401 (2018).

[42] Elias, D. C. *et al.* Control of graphene's properties by reversible hydrogenation: evidence for graphane. *Science* **323**, 610–613 (2009).

[43] Lilley, J. Nuclear physics principles and application, 2001. *West Sussex, England, UK: John Wiley & Sons Ltd* (2001).

[44] Seliverstov, M. *et al.* Electromagnetic moments of odd-A Po 193–203, 211 isotopes. *Physical Review C* **89**, 034323 (2014).

[45] Seikh, M. F. H. Importance of 1-3 Mixing Angle in Three-Flavor Neutrino Oscillations Paradigm (2019).

[46] Ubieto Díaz, M. *Off-line commissioning of a non-destructive FT-ICR detection system for monitoring the ion concentration in the KATRIN beamline.* Ph.D. thesis, Ruprecht-Karls-Universität Heidelberg, Germany (2011).

[47] Dirac, P. A. M. The quantum theory of the emission and absorption of radiation. *Proceedings of the Royal Society of London. Series A, Containing Papers of a Mathematical and Physical Character* **114**, 243–265 (1927).

[48] Martin, B. R. *Nuclear and particle physics an introduction* (John Willey & Sons, 2006).

[49] Aker, M. *et al.* Direct neutrino-mass measurement with sub-electronvolt sensitivity. *Nature Physics* **18** (2022).

[50] Bernabeu, J., Burguet-Castell, J., Espinoza, C. & Lindroos, M. Perspectives in Neutrino Physics: Monochromatic Neutrino Beams. *arXiv preprint hep-ph/0512299* (2005).

[51] Leo, W. R. *Techniques for nuclear and particle physics experiments: a how-to approach; 2nd ed.* (Springer, Berlin, 1994). URL https://cds.cern.ch/record/302344.

[52] Bolza, M. Graphene transistors - GFET - graphene field effect transistors (2012). URL https://www.graphenea.com/pages/what-are-graphene-field-effect-transistors-gfets.

[53] Graphenea. Technical Datasheet Graphene Field-Effect Transistor Chip: S10 (2020).

[54] Graphenea. Measurement Protocols and Handling Instructions Graphene Field-Effect Transistor Chip: GFET-S10 (2020).

[55] Booth, H. S. & McIntyre, L. When Is a Desiccator? *Industrial & Engineering Chemistry Analytical Edition* **8**, 148–149 (1936).

[56] Agency, I. A. E. Live Chart of Nuclides (2020). URL https://www-nds.iaea.org/relnsd/vcharthtml/VChartHTML.html.

[57] Ghassemi, A., Sato, K. & Kobayashi, K. Literature / MPPC - hub.hamamatsu.com (2022). URL https://hub.hamamatsu.com/content/dam/hamamatsu-photonics/sites/documents/99_SALES_LIBRARY/ssd/mppc_kapd9005e.pdf.

[58] Shockley, W. The theory of p-n junctions in semiconductors and p-n junction transistors. *The Bell System Technical Journal* **28**, 435–489 (1949).

[59] Hamamatsu. Home Hamamatsu photonics (2022). URL https://www.hamamatsu.com/content/dam/hamamatsu-photonics/sites/documents/99_SALES_LIBRARY/ssd/mppc_kapd0006e.pdf.

[60] K.K., H. P. C12332-02 Simple evaluation driver circuit for non-cooled MPPC (2021).

[61] Technology, E. GENERAL PURPOSE PLASTIC SCINTILLATOR EJ-200, EJ-204, EJ-208, EJ-212 (2021).

[62] Saint-Gobain, C. BC-400,BC-404,BC-408,BC-412,BC-416 Premium Plastic Scintillators (2021).

[63] Schiavilla, R. *et al.* Weak capture of protons by protons. *Physical Review C* **58**, 1263–1277 (1998). URL https://doi.org/10.1103%2Fphysrevc.58.1263.

[64] NRC. 0751 - H122 - basic health physics - 32 - shielding radiation. (2011). URL https://www.nrc.gov/docs/ML1122/ML11229A721.pdf.

[65] Harvard university. α, β, γ penetration and shielding (2016). URL https://sciencedemonstrations.fas.harvard.edu/presentations/%CE%B1-%CE%B2-%CE%B3-penetration-and-shielding.

Appendix

A   Cross-section neutrinos

The average cross-section was given by Eq. A.1

$$\langle \sigma v_\nu \rangle = \frac{G_F^2 E_e p_e}{2\pi} F(Z, E_e) \frac{m_{^3He}}{m_{^3T}} (|F|^2 + g_A^2 |GT|^2), \tag{A.1}$$

with F the Fermi form factor and GT the Gamow-Teller form factor and g_A the axial coupling. With values of $|F|^2 = 0.9987$, $|GT|^2 = 2.788$ and $g_A = 1.2695$ were used. $m_{^3He}$ and $m_{^3T}$ were the masses of the ^3He and ^3T respectively. $F(Z, E_e)$ was the Fermi function which described the coulomb attraction effect between the proton and the outgoing electron. This enhanced the cross-section by a factor of $F(Z, E_e) \approx 1.2$ which was found via Eq. A.2

$$F(Z, E_e) = \frac{2\pi\mu}{1 - \exp(-2\pi\mu)}, \tag{A.2}$$

where $\mu = Z\alpha E_e / p_e$ with $p_e = \sqrt{2Qm_e}$. It was taken that $Z = 2$ and $Q = 18.6\, keV$ to arrive at $F(Z, E_e) \approx 1.2$. This resulted in the average cross-section of $\langle \sigma v_\nu \rangle \approx 1.1 G_F^2 E_e p_e \approx 1.5 G_F^2 m_e^{3/2} Q^{1/2} \approx 3.7 \cdot 10^{-45}\, cm^{-2}$ [5, 63].

B   Back-of-the-envelope calculations: range β particles radioactive source

Here some back of the envelope calculations for the range of β particles in SiO_2 were given. When evaluating Eq. B.1 it was possible to find $\sigma = 0.176 \, g/cm^2$. Here the average energy of $E_{avg} = 0.54586 \, MeV$ for the Sr-90 source was taken [64]. For the Y-90 particles, this equation was not valid.

$$\sigma = 0.407 E_{max}^{1.38}, \tag{B.1}$$

here E_{max} was the max energy for the decay if the maximum energy was smaller than $0.8 \, MeV$. For the radioactive source, the maximum energy was larger than $0.8 \, MeV$ due to the presence of the radioactive decay product Y-90 but this calculation gave the first impression of the distance the particles could travel through SiO_2. To calculate the actual distance Eq. B.2 was used, as shown below

$$d_x = \frac{\sigma}{\rho}. \tag{B.2}$$

In this equation, ρ was the density of the material which was $\rho_{SiO_2} = 2.65 \, g/cm^3$ for SiO_2 and σ was the range of the particle. d_x gave the actual distance with $d_x = 6.661 \cdot 10^{-4} \, m = 0.6661 \, mm$. The maximum energy for the β particles from the radioactive source was larger than the E_{max} for the Sr-90 β particles. In Eq. B.3 an equation for β particles with maximum energies larger than $0.6 \, MeV$ was given, this equation was called Feather's rule [64].

$$\sigma = 0.542 E_{max} - 0.133, \tag{B.3}$$

here E_{max} was the maximum energy for this decay. It was important to keep in mind that the decay product of Sr-90 also was a radioactive β source, Y-90. The maximum energy of this decay (and thus of the entire source) was $E_{max} = 2.28 \, MeV$. When the distance was calculated the distance $d_x = 0.416 \, cm = 4.16 \, mm$ was obtained. This would also agree with the ability of the β particles from the radioactive source to pass the wafer below the graphene.

To determine the range of β particles quickly a rule of thumb was proposed by Harvard Natural Sciences Lecture Demonstrations. For β particles with average energy $E > 0.8 \, MeV$ three situations were distinguished depending on the density ρ for the material. First, for each $1 \, MeV$ of energy of the β particles, the range was $0.5 \, mm$ in the high-density matter. Second, for each $1 \, MeV$ of energy of the β particles, the range was $1.0 \, mm$ in medium-density matter. Third, for each $1 \, MeV$ of energy of the β particles, the range was $2.0 \, mm$ in low-density matter [39] [65].

The density of SiO_2 was $\rho_{SiO_2} = 2.65 \, g/cm^3$ which was classified as a medium-density matter. The β particles in this experiment had an average energy of $E_{avg} = 0.54586 \, MeV$ and a maximum energy of $E_{max} = 2.28 \, MeV$. According to this rule of thumb, the β particles from the Sr-90 source should be able to penetrate between $0.55 \, mm - 2.28 \, mm$, which would be enough for the detection of particles despite the shielding of the SiO_2.

---

[39]Sometimes it was difficult to determine the average energy from the maximum energy (or vice versa). In this case, it was useful to use the rule of thumb: $E_{avg} \approx \frac{1}{2} E_{max}$, where E_{avg} was the average energy and E_{max} was the maximum energy [65].
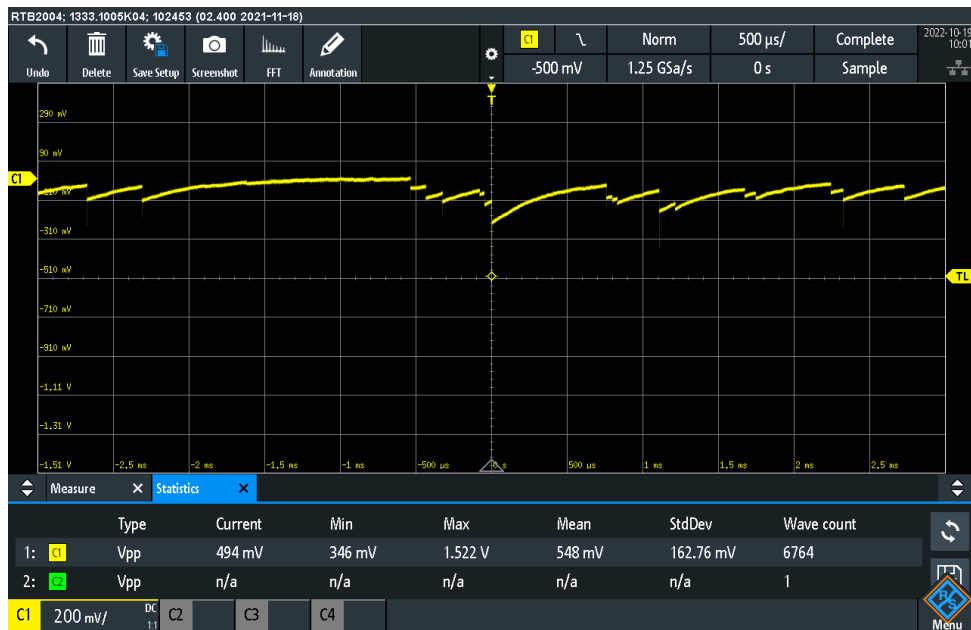
C   Results Scintillator setup

C.1   Screenshots of oscilloscope

In this subsection, screenshots of the screen of the oscilloscope were shown. The shape of the signals could be observed in these pictures.
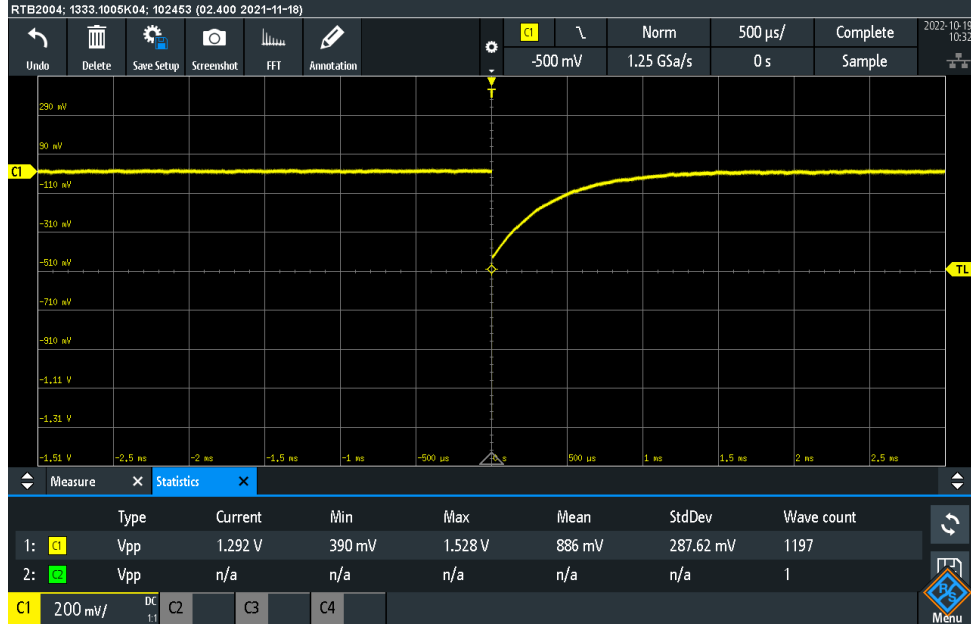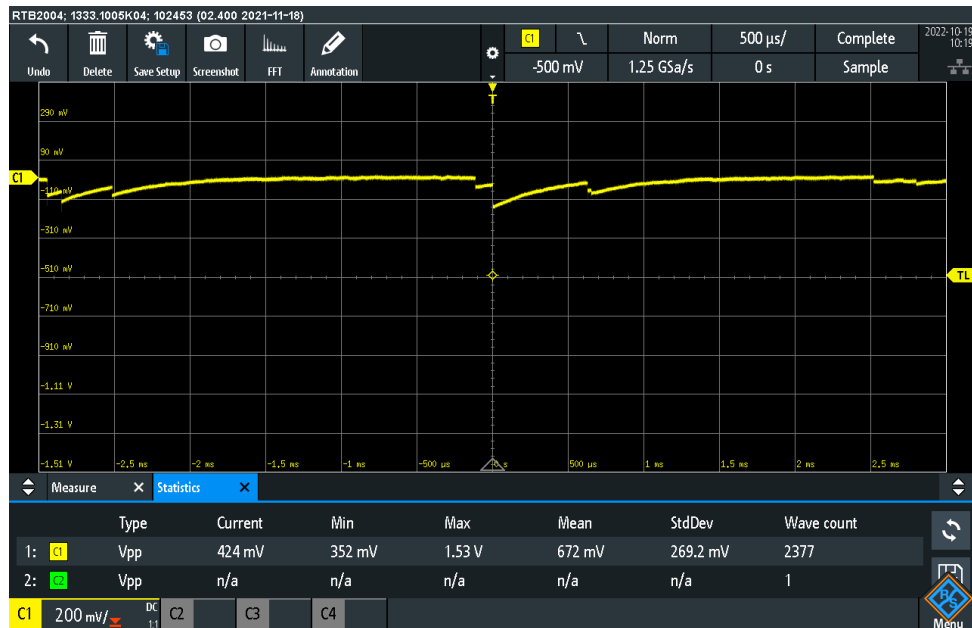

Figure C.1: The signal on the oscilloscope for the background, with the trigger level ($-500mV$) and time scale.

Figure C.2: The signal on the oscilloscope for the source, with the trigger level ($-500\,mV$) and time scale.
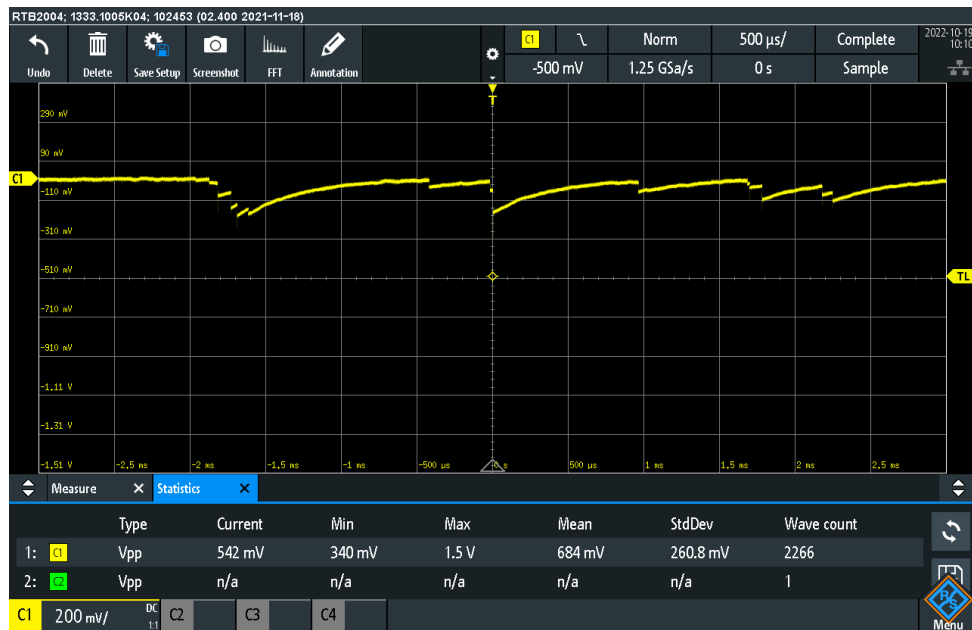
Figure C.3: The signal on the oscilloscope for the source and SiO_2 wafer, with the trigger level $(-500\,mV)$ and time scale.

Figure C.4: The signal on the oscilloscope for the source and graphite, with the trigger level $(-500\,mV)$ and time scale.